

<https://helda.helsinki.fi>

Recent research and advances of material-based saturable absorber in mode-locked fiber laser

Lau, K. Y.

2021-05

Lau , K Y & Hou , D 2021 , ' Recent research and advances of material-based saturable absorber in mode-locked fiber laser ' , Optics & Laser Technology , vol. 137 , 106826 . <https://doi.org/10.1016/j.optlas>

<http://hdl.handle.net/10138/352647>

<https://doi.org/10.1016/j.optlastec.2020.106826>

cc_by_nc_nd

acceptedVersion

Downloaded from Helda, University of Helsinki institutional repository.

This is an electronic reprint of the original article.

This reprint may differ from the original in pagination and typographic detail.

Please cite the original version.

Recent research and advances of material-based saturable absorber in mode-locked fiber laser

K. Y. Lau^{1,*} and D. Hou^{2,3}

¹ Department of Electronics and Nanoengineering, Tietotie 3, Aalto university, 02150 Espoo, Finland.

² Department of Culture, University of Helsinki, Unioninkatu 38, University of Helsinki, 00014 Helsinki, Finland.

³ International Office, Renmin University of China, No. 59 Zhongguancun Street, Haidian District Beijing, 100872, P.R. China

Corresponding author*: Lau.kuenyao@aalto.fi

Abstract

The incorporation of the material-based saturable absorber (SA) to generate mode-locked fiber laser (MLFL) has been extensively explored and demonstrated. However, the material-based SAs have some challenges in terms of optical damage threshold, design complexity, robustness, and stability due to several factors. Presently, several works have been demonstrated to address material-based SA fabrication issues. Therefore, this paper aims to comprehensively review the pros and cons of material-based SA in terms of material synthesis techniques, material characteristics, material-polymer composite, SA structure, and deposition techniques, along with current issues and challenges, and conclude with concrete recommendations. All the highlighted insights of this review will contribute to the increased efforts toward the development of the material-based SAs for the MLFL.

Keywords

Fiber laser, mode-locking, saturable absorber

1.0 Introduction

Mode-locking is a laser mechanism which induces phase-locked longitudinal modes to generate ultrashort pulses of intense coherent light and repetition rate in conjunction to the laser cavity round-trip time [1]. Among the laser configuration, fiber laser possesses distinctive advantages in contrast to conventional solid-state laser with higher beam quality, lightweight, compactness, cost-effective, better heat dissipation, environmentally robust, and alignment-free mechanism [1][2][3]. Mode-locked fiber laser (MLFL) has been extensively studied not only in scientific research but also significantly deployed in practical applications, such as optical signal processing [4], optical coherence tomography [5], high-speed optical frequency comb [6], synchronization for optical and microwave sources [7], waveguide writing in glass [8], radar remote sensing [9] and time-resolved spectroscopy [10].

The MLFL is generated through either active or passive approaches. The active mode-locking operation is conducted with an external modulator, which modulates the resonator losses in exact synchronism with the laser cavity round-trips. The modulator is typically bulky and has limited temporal response in ultrashort pulse generation [11]. This spurs the investigation of passive element, saturable absorber (SA) which transmits light at high excitation intensities with reduced optical loss when the initial states of absorbing transition is empty and the final states are fully occupied. The SA shows distinctive advantages to active mode-locker in terms of compactness, simplicity, flexibility, and shorter achievable pulse duration [3][12].

In this review, emphasis is given to real SA rather than artificial SA. Examples of artificial SA are nonlinear polarization rotation (NPR), nonlinear amplifying loop-mirror (NALM), and nonlinear optical loop-mirror (NOLM). Artificial SAs are bulky and vulnerable to environmental condition such as fiber movement, temperature and vibration, which causes low reproductive MLFL [13][14]. In addition, artificial SAs show random birefringence and polarization which is difficult to design stable laser cavities [15]. On the other hand, the real SA addresses the limitation of artificial SA by providing a more mechanically and environmentally stable device in 1D, 2D and 3D material structures. An example of 1D material is carbon nanotube (CNT), whereas 2D materials are atomically thin with monolayer or a few layer materials, whilst 3D materials are generally bulk crystal [13]. Among these materials, 2D material is more frequently employed to fabricate the SA due to several advantages such as low insertion loss of material in atomic thickness which is feasible for optoelectronic devices, electronic properties dependent on structural details such as doping, defect, thickness, as well as stacking easiness to form multilayer structure of heterojunctions [16]. An example of 2D material is graphene, which has been optimized in terms of its modulation depth by stacking the graphene layer or employing the effect of cross absorption modulation [17][18]. Lately, optimization of four 2D materials has been analysed in terms of the self-amplitude modulation (SAM) coefficient [19]. Based on the studies, 2D materials with higher SAM coefficient generates shorter pulse width when the laser is operating in the low gain condition. More investigations and reviews into optimization of 2D material as the saturable absorber includes the bandgap tuning for mid-infrared red wavelength operation [3], improving the fabrication methods and adopting an integrated approach for high peak power generation [20], and bandgap engineering to achieve higher modulation depth [21].

Since the first demonstration of SA incorporating CNT in 2004 [22], graphene in 2009 [23], transition metal dichalcogenide (TMD) in 2014 [24], and black phosphorus (BP) in 2015 [25], numerous technical and review articles have been presented from year 2015 to 2020. The most recent review was done on BP-SA [3], as well as recent development of 2D materials in photonics, optoelectronics devices and fiber laser [26][27][28][29][30]. Apart from the aforementioned materials, numerous SA candidates such as detonation nanodiamond (DND), deoxyribonucleic acid (DNA),

metal-organic framework (MOF), gold nanorods (GNRs), and quantum dot (QD) materials such as phosphorene, bismuthene, antimonene, and tellurene have been lately discovered. Nevertheless, the pros and cons of these materials have not been thoroughly reviewed since the first demonstration as the SAs. In this review, a comprehensive study is on the synthesis techniques and material properties of these SA candidates, as well as the interaction with polymers and SA configuration on optical fiber platform to have a better insight on the recent advances of the material-based SA in the MLFL.

2.0 Material synthesis techniques

The three most commonly utilized material synthesis techniques are composed of mechanical exfoliation (ME), liquid-phase exfoliation (LPE), and chemical vapour deposition (CVD). A comparison was made among these techniques and summarized with the advantages and limitations. Apart from these techniques, the discussion was also made to other proposed techniques of synthesizing the SA materials.

2.1 ME

ME was firstly employed to synthesis a small amount of graphene from graphite with scotch tape [31][32]. ME is a top-down technique in nanotechnology by creating either a longitudinal or transverse stress on the surface of a layered structured materials [33]. Examples of ME method include the synthesis of graphene from higher ordered pyrolytic graphene [34], single or natural graphite [34][35] with scotch tape [25][36][37], ultrasonication [38], electrical field [39], and transfer printing [40]. The most typical example of the process of ME is using adhesive tape method is-as illustrated in Fig. 1. During ME, thin flakes are moderately exfoliated from a large size of bulk material using scotch tape [25][36][37]. Firstly, a bulk graphite was prepared on a substrate. Next, the bulk graphite is peeled off with an adhesive tape, leaving thinner multiple-layered graphene on the substrate. Then, thinner flakes or reduced number of layers are obtained by continuously pressed the multiple-layered graphene to be adhered to the scotch tape. In the ideal case, a monolayer with thickness of ~0.34 nm would be eventually acquired as the final product. Therefore, However, the ME-synthesized flakes are normally-practically appeared with varying thickness, ranging from nanometers to several tens of millimeters for single layer graphene [33][41]. After the ME, the layered-materials can be deposited on quartz substrate and cleaned with oxygen plasma prior to exfoliation [42] or attaching the tape to the acetone substrate to detach the tape [33]. Therefore, ME shows advantages due to its simplicity and reliability since no chemical procedures and expensive devices are needed throughout the entire synthesis process [25]. In addition, ME is beneficial in getting high quality product than LPE, at the expense of lower production efficiency and labour exhaustive for mass production [37][43][44][45]. In addition, the reliability of acquiring similar structure of 2D material with ME process is quite insignificant [33]. Apart from graphene, Another example of the ME techniques was proposed to synthesize a ~300 nm thick phosphorene from bulk BP

crystal [46][47]. ~~In this scheme, however, the ME possesses an issue of high power illumination which induces thermal effect and optical damage that speeds up the oxidation of the BP material, such as BP [48].~~

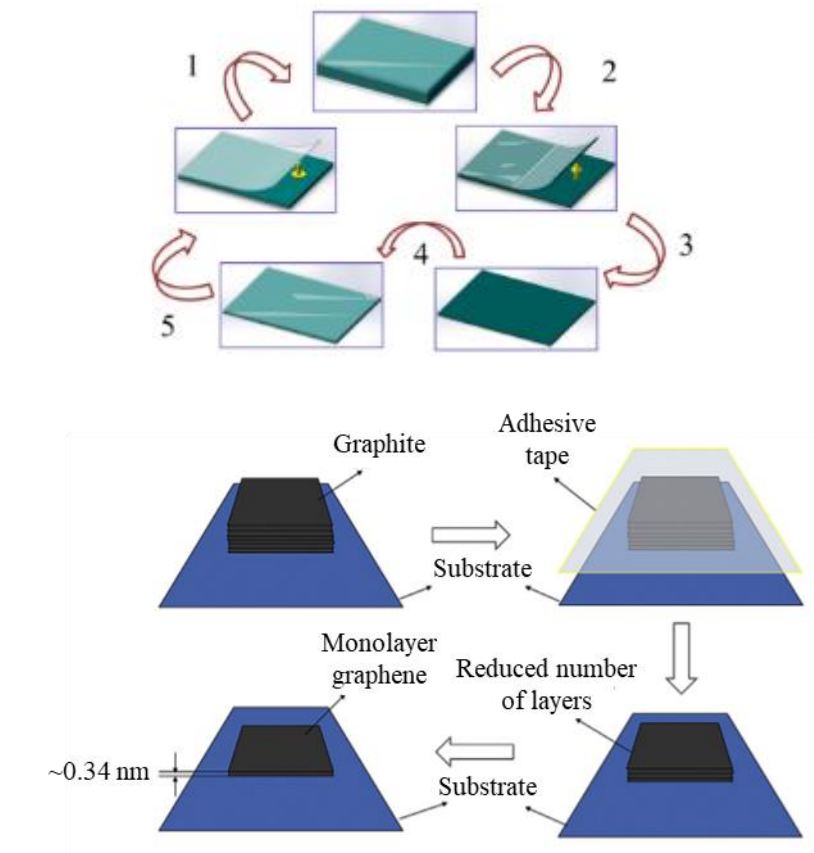


Fig. 1: Process of the ME method ~~for the synthesis of monolayer graphene [40][25].~~

2.2 LPE

LPE is a facile approach to fabricate thin 1D or 2D nanomaterial from the bulk crystal in mass production with high stability in ambient conditions [48][49]. This technique is suitable to synthesize flexible composite materials due to the scalability in fabricating wafer-scale thin film [50]. An example of LPE process is depicted in Fig. 2. During LPE, small-sized powder is exfoliated into nanosheet by immersing into dissolving solvents such as N-methyl-2-Pyrrolidone (NMP), and undergoes ultrasound probe sonication to overcome the interlayer Van der Waals' force for further exfoliation, followed by centrifugation of the nanosheets to remove the residual large sediments, deposits or large-sized crystal in the suspension. In some cases, a vacuum filtration might be applied after the LPE method to further clean the synthesized thin film [51]. During the sonication process, a non-contact sonicator might help to reduce the contamination of the sample [48].

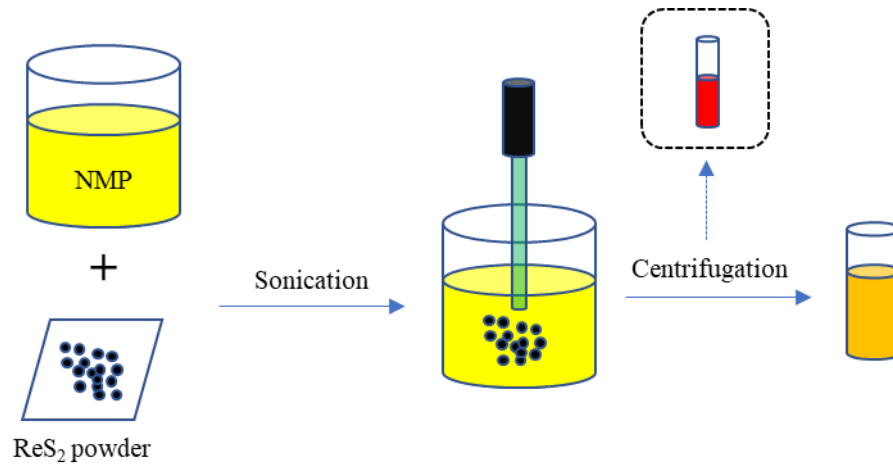
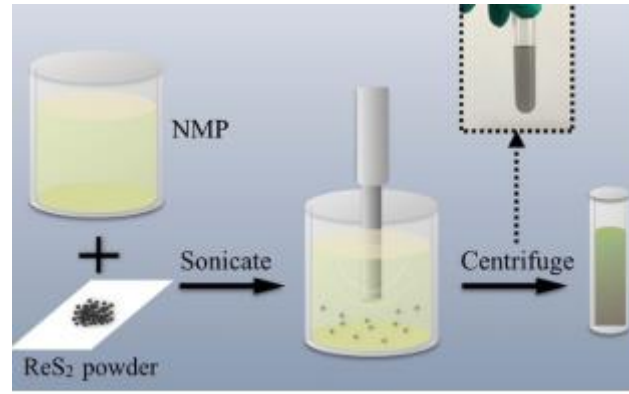


Fig. 2: Process of the LPE method [51].

Both ME and LPE are cost-effective techniques [44][52]. Additionally, LPE produces 2D nanosheet in a larger amount than ME in an ambient condition [53] and does not require toxic elements and polymer to transfer the film in contrast to CVD method [54]. LPE has shown a remarkable advantage by allowing the material, such as graphene to form composite with polymeric material in both liquid and solid form easily [55]. However, LPE shows the limitation in controlling the lateral size and thickness of the synthesized nanosheets [56]. Table 1 summarizes the LPE process parameters for recent reported SAs.

Table 1: Parameters of SA materials synthesized through LPE method.

Ref.	Raw materials	Products	Immersion solvent	Sonication for exfoliation in	Sonication power and frequency	Sonication time	Centrifuge speed	Centrifuge time
[57]	bismuth powder	Bismuthene	IPA	Spiral glass bottle in ice bath condition using probe sonication	-	10 hours	5000 rpm	20 minutes
[51]	ReS ₂ powder	ReS ₂ film	NMP	Water bath using supersonic machine	550 W	1 hour	4000 rpm	10 minutes
[58]	SnS ₂ nanosheet	SnS ₂ dispersion	Alcohol	Ultrasonic cleaner	-	12 hours	2000 rpm	30 minutes
[48]	HfS ₂ bulk crystal	HfS ₂ nanosheet	IPA	Ice bath ambient with non-contact sonicator	360 W	10 hours	5000 rpm	30 minutes
[59]	Purified <u>single-walled carbon nanotube (SWCNT)</u>	SWCNT dispersion	DI water + SDBS	Ultrasonic processor	200 W, 20 kHz	1 hour	25000 rpm	1 hour
[60]	SWCNT (~ 1.3 nm mean diameter)	SWCNT dispersion	DI water + Na-CMC	Tip sonicator	50 W, 20 kHz	1 hour	30000 rpm	-
[61]	Bulk antimony	Antimonene	NMP	Bath sonication	100% power, 40 kHz	4 hours	-	-
[49]	Grinded bulk BP	Phosphorene	NMP	Ice bath sonicator	200 W	3 hours	1) 7000 rpm 2) 12000 rpm	1) Remove undefoliated bulk BP. 2) 20 minutes
[62]	Magnesium powder	N-G nanoparticles	DI water	heterothermal stainless steel autoclave tube (500 °C)	-	20 hours	-	-
[63]	SWCNT powder	SWCNT nanosheet	NMP	Sonication bath	-	1 hour	4000 rpm	3 hours
[64]	Bulk BP crystal	OBP nanoflakes	Aqueous solution	Tip sonication in ice bath	-	3 hours	3000 rpm	20 minutes
[65]	TiS ₂ bulk crystal	Few layer TiS ₂	NMP	Ice bath Sonicator	400 W, 40	5 hours	14000 rpm	25 minutes

				(below 25 °C)	kHz			
[66]	Graphite + bulk BP	GR-BP nanosheet	NMP	Ultrasonic bath	300 W	9 hours	9000 rpm	10 minutes
[55]	Graphite flakes	Graphene dispersion	NMP	Ultrasonic bath	100 W	9 hours	10000 rpm	1 hour
[44]	MoSe ₂ /WSe ₂ bulk crystal	MoSe ₂ /WSe ₂ nanosheet	sodium deoxycholate bile salt surfactant + DI water	Ultrasonic bath	180 W	8 hours	1000 rpm	10 minutes
[67]	Bulk MoSe ₂	Few layer MoSe ₂	Lysine solution	Ultrasonication	-	20 hours	1000 rpm	30 minutes
[68]	WS ₂ flakes	WS ₂ nanosheet	Ethanol + water	Ultrasonic cleaner	-	120 minutes	3000 rpm	30 minutes
[69]	Bulk MoS ₂	MoS ₂ nanosheet	DI water + SC	Point probe (Flathead sonic tip)	285 W	60 minutes	1500 rpm	90 minutes
[70]	Bulk ReS ₂	ReS ₂ nanosheet	NMP	Cell crusher	180 W	2 days	3000 rpm	30 minutes
[71]	Bulk bismuth (grinded into bismuth powder)	Bismuthene	Ethanol	Ice bath probe sonicator	-	15 hours	7000 rpm	20 minutes
[72]	Bulk BP crystal	Few layer BP flakes	NMP	Bath sonicator (15 °C)	-	12 hours	1500 rpm	30 minutes
[73]	ReS ₂ powder	ReS ₂ nanosheet	Alcohol + water	High power ultrasonic cleaner	-	12 hours	2000 rpm	20 minutes
[74]	Bulk BP	BP nanosheet	NMP	Ultrasound probe sonicator	900 W	6 hours	3000 rpm	30 minutes
[75]	Bulk BP	BP nanosheet	NMP	Ice-bath	150 W	4 hours	7000 rpm	20 minutes
[76]	Bulk BP	BP nanoflakes	NMP	Bath ultrasonication (30 °C)	40 kHz, 100% power	4 hours	3000 rpm	10 minutes
[15]	SWCNT agglomerate powder	SWCNT	DMF	-	-	2 hours	-	5 minutes
[50]	WS ₂ powder	Mono- and few-layer WS ₂	SC	Horn probe sonic tip	750 W (38% output power)	1 hour	300 rpm	90 minutes
[77]	Bulk BP powder	Few-layer BP	NMP	Bath sonicator	300 W, 40 kHz	10 hours	1500 rpm	10 minutes

[78]	SnS ₂ nanosheet	SnS ₂ dispersion	Alcohol	Ultrasonic cleaner	-	12 hours	2000 rpm	30 minutes
[79]	InSe powder	InSe nanosheet	Alcohol	Ultrasonic cleaner	-	6 hours	-	20 minutes
[80]	WS ₂ flakes	WS ₂ nanosheet	Ethanol and water	Ultrasonic cleaner	-	10 hours	5000 rpm	1 hour
[81]	Antimonene powder	Antimonene nanoflakes	ethanol	Ultrasonic cleaner	300 W, 40 kHz, room temperature	2.5 hours	1500 rpm	48 hours
[82]	Bulk tellurium crustal	Tellurene nanosheet	ethanol	Sonicator	40 kHz	8 hours	1500 rpm	30 minutes
[83]	Tellurium powder	Tellurene nanosheet	ethanol	Ultrasonic cleaner	-	8 hours	2000 rpm	30 minutes
[84]	PdS ₂ powder	PdS ₂ supernatant	Isopropyl alcohol	Bath Ultrasonication	400 W, 40 kHz	20 hours	3000 rpm	5 minutes

Note: IPA – Isopropyl alcohol, ReS₂ – rhenium disulfide, SnS₂ – tin disulfide, HfS₂ – hafnium disulfide, SWCNT – single-walled carbon nanotube, SDBS - sodium dodecylbenzene sulfonate, Na-CMC – sodium-carboxymethylcellulose, N-G – Nitrogen-doped graphene, OBP – oxidized black phosphorus, TiS₂ – titanium disulfide, GR-BP – graphite-black phosphorus, MoSe₂ – molybdenum diselenide, WSe₂- tungsten diselenide, WS₂ – tungsten disulfide, MoS₂ – molybdenum disulfide, SC – sodium cholate, InSe – indium diselenide, PdS₂ – Palladium disulfide

2.3 CVD

In contrast to ME and LPE with uncontrollable lateral size and thickness of the synthesized product with few to few tens of μm [85], CVD induces less damage and produces a larger amount of uniform 2D nanosheets [53][86]. CVD produces films with more uniform thickness than randomized deposition by spin coating method thus improving the interaction efficiency [53]. Typically, CVD is employed to synthesize monolayer material [87]. The CVD method precisely grows the material layer on a substrate. For instance, CVD has been previously utilized to grow graphene on Cu substrate [88][89][90][91], WSe_2 [85], PtSe_2 [92] or ReS_2 [93] on sapphire substrate, or MoS_2 [94] and WS_2 on Si or SiO_2 substrate [53], WSe_2 and MoTe_2 on Al_2O_3 substrate [87]. The CVD is a common method to fabricate monolayer graphene with higher product quality than ME and LPE. The CVD-grown graphene can be deposited easily on a 100 nm thick gold film using thermal evaporation to achieve stable mechanical support during the transfer process [95]. In addition, mechanical support is also provided by spin coating a polymethyl-methacrylate (PMMA) layer on the graphene layer [91][96]. After all, the detachment of monolayer graphene from the Cu substrate can be performed with electrochemical delamination method [91]. Apart from monolayer graphene, examples of SA materials synthesized by CVD include:

1. Double-walled carbon nanotube (DWCNT) was synthesized by methane (CH_4) over $\text{Mg}_{1-x}\text{Co}_x\text{O}$ solid solution containing Mo oxide [97]. The oxidation of CNT was performed at 570 °C for 30 minutes after the growth process. Then, the metal oxides are rinsed with hydrochloric acid (HCl) to remove the residual materials. After that, purified DWCNT was ultra-sonicated in DI water and SDBS for 240 minutes in 10 °C. Finally, the large bundles are removed by centrifugation.
2. An aerosol CVD method was employed to grow CNT on the surface of iron particles suspended in the gas phase inside a heat flow reactor and collected on a micro-porous filter [98]. This method is advantageous without the utilization of polymer for the purification steps as well as does not involve any liquid dispersion in transferring the CNT film to another substrate.
3. A rotary pump vacuum oil was deployed as the carbon source in synthesizing a CVD-grown graphene [99]. During this process, a Cu foil substrate is placed into a tubular furnace and was evacuated to ~ 3 mTorr by a rotary pump, whereas the sample was heated to 1000 °C for 30 minutes. Finally, the graphene layer covers the entire Cu substrate when the film was cooled down to room temperature.
4. In a CVD process of synthesizing WSe_2 powder, WO_3 and Se powder were employed as the starting material inside a quartz tube furnace, where the vapours of both materials are brought to the targeted sapphire substrate through H_2/Ar flow gas [85]. The furnace was heated to a maximum temperature of 920 °C at the middle part of the furnace with Gaussian profile. A monolayer WSe_2 was grown on a sapphire substrate when the temperature was adjusted to 790 °C. Small WSe_2 domains

(monolayer, bilayer, or tri-layer) were continuously grown on WSe₂ monolayer by decreasing the sapphire substrate to 750 °C.

Although CVD method provides a more uniform material grown on a substrate with better quality than ME and LPE, CVD method requires hot substrate temperature for the flake transfer [100], as well as the synthesis process is more complicated [101] and cost ineffective [44]. In addition, the etching process of this method is rather difficult due to the utilization of toxic solutions and polymers [54]. The comparison among ME, LPE, and CVD are tabulated in Table 2. In the case where high-quality 2D nanosheet is required with a sufficient fabrication budget, CVD method is recommended. LPE is suggested when the production efficiency of 2D nanosheet is essential with a cheaper solution without emphasizing the quality of the synthesized products. ME is intermediately suggested when higher material quality than LPE and cheaper cost than CVD is anticipated.

Table 2: Comparison for ME, LPE and CVD methods.

Methods	Advantages	Disadvantages
ME	<ol style="list-style-type: none"> 1. Cost-effective. 2. Higher nanosheet quality than LPE. 3. Does not involve chemical procedures. 	<ol style="list-style-type: none"> 1. Low production efficiency. 2. Ease of optical damage and thermal effect by high power illumination.
LPE	<ol style="list-style-type: none"> 1. Cost-effective. 2. Synthesize large amount of nanosheet. 3. Does not involve toxic elements and polymers to transfer the film. 	<ol style="list-style-type: none"> 1. Difficulties in controlling the lateral size and thickness of the synthesized nanosheet. 2. Low uniformity and product quality.
CVD	<ol style="list-style-type: none"> 1. Synthesize large amount of nanosheet with less damage. 2. Nanosheet is uniformly grown with precise thickness. 3. High product quality. 	<ol style="list-style-type: none"> 1. Cost ineffective and complicated. 2. Requires hot substrate temperature for flake transfer.

2.4 Other material synthesis methods

Apart from ME, LPE and CVD, other techniques have been occasionally proposed in synthesizing the SA materials. The highlights of these techniques will provide a more thorough review of the material synthesis methods.

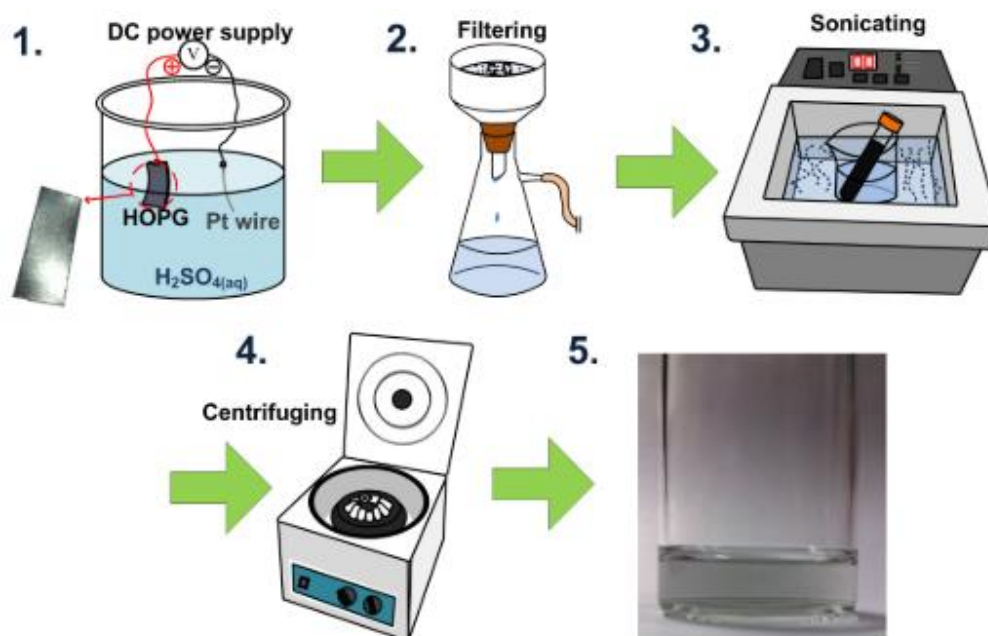
2.4.1 Modified Hummer's method

Modified Hummer's method is integrated in synthesizing graphene ethanol solution [102]. In this method, GO was stirred into hydrogen peroxide (H₂O₂) and sulphuric acid (H₂SO₄), rinsed with DI water, and heated to 1000 °C for 30 seconds. Then, the GO was ultra-sonicated in DI water and reduced by hydrazine hydrate at 95 °C for 12

hours. Finally, the graphene ethanol solution is obtained by ultra-sonication for 3 hours. In addition, the modified Hummer's method was also demonstrated in synthesizing GO and reduced graphene oxide (rGO) thin film by dispersing these materials in DI water and ultra-sonicated for an hour [103]. The ultra-sonication was performed with hydrazine monohydrate vapour and an aluminium substrate from 100 to 120 °C. The aluminium substrate is finally removed with HCl solution and the film was rinsed with DI water to remove the corrosion impurities. This method is recommended to synthesize graphene-based solution or thin-film in multiple layer thickness.

2.4.2 Electrochemical exfoliation

Electrochemical exfoliation is an alternative of the CVD to synthesize high-quality graphite nanosheet powder by exfoliating graphite foil using electrolysis mechanism [104]. In contrast to CVD, electrochemical exfoliation exfoliates the graphene flakes by applying DC bias to the anode (graphite foil) in a diluted H_2SO_4 solution. The electrochemically exfoliated graphite flakes are extracted by a porous filter. Next, the residues were rinsed with acetone in a sonicator bath at room temperature for 10 minutes and centrifuged at 1000 rpm for 2 minutes to obtain the graphite nanosheet powder. The procedures of electrochemical exfoliation in synthesizing graphite nanosheet powder are presented in Fig. 3. This method is recommended with the advantage of controllable size and thickness of the graphite nanosheet powder by the anodic oxidation with a biased electrolysis.



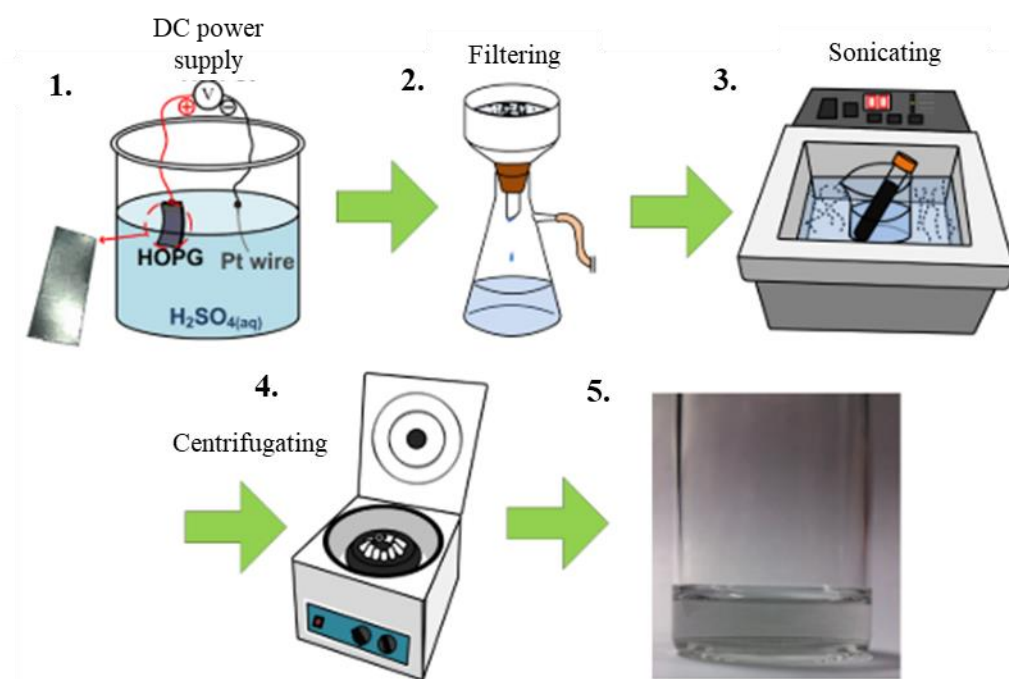


Fig. 3: Electrochemical exfoliation steps in synthesizing graphite nanosheet powder [104].

2.4.3 Colloidal chemistry method (CCM)

The CCM method has been proposed in synthesizing quantum dot (QD) material [105]. This method is recommended in preparing colloidal quantum dot (CQD) than other preparation methods such as epitaxial and solution approaches due to lower process cost and higher design flexibility. Besides CQD, a demonstration of CCM was presented in synthesizing TiS_2 nanosheet [106]. Firstly, 3.7 mL of oleylamine, 15 mL of octadecene, and 0.2 mmol titanium chloride (TiCl_4) were mixed together. This mixture was then stirred and heated to 220 °C in a concentrated Argon (Ar) gas ambient condition for 15 minutes. Meanwhile, carbon disulfide (CS_2) was immediately injected into the mixture and the temperature was increased to 300 °C. The cooling of the mixture takes 3 hours, and the mixture was centrifuged with hexane and anhydrous ethanol to produce the TiS_2 nanosheet.

2.4.4 Hydrothermal/solvothermal method

In contrast to LPE, the hydrothermal/solvothermal method produces the crystalline by stirring the materials in dissolving solvent with higher temperature, followed by centrifugation to remove large sediments. For instance, the mixture of MOF precursor in alcohol and DMF was thermally synthesized at 110 °C for 12 hours inside a Teflon-lined stainless-steel autoclave for the crystallization process [107]. After completing the crystallization process, the MOF precursor was cooled to room temperature. The precipitate was removed by centrifuging the products with DMF and alcohol with 11000 rpm for 12 minutes and dried with 55 °C for 12 hours inside an oven. Besides MOF, hydrothermal method was also used to synthesize [black](#)

phosphorus quantum dot (BPQD) and graphite carbon nitride (GCN). The BPQD was synthesized from bulk BP crystal in sodium hydroxide (NaOH) NMP solution under vigorous stirring for 6 hours with 140 °C in a nitrogen ambient condition [56][108]. The non-exfoliated BP crystal was centrifuged at 7000 rpm for 20 minutes. The hydrothermal process of synthesizing BPQD is illustrated in Fig. 4. In addition, the GCN was autoclaved with the surfactant of formamide, citric acid, and sodium acetate mixture at 230 °C for 3 hours [109]. The product was then centrifuged at 11000 rpm for 5 minutes to remove the precipitate with ethanol. Moreover, Ag₂S nanosheet was also prepared by hydrothermal method by mixing the AgS₂ powder with alcohol in a ratio of 1:3, which is then putting on a heating mixing table for 2 hours [110].

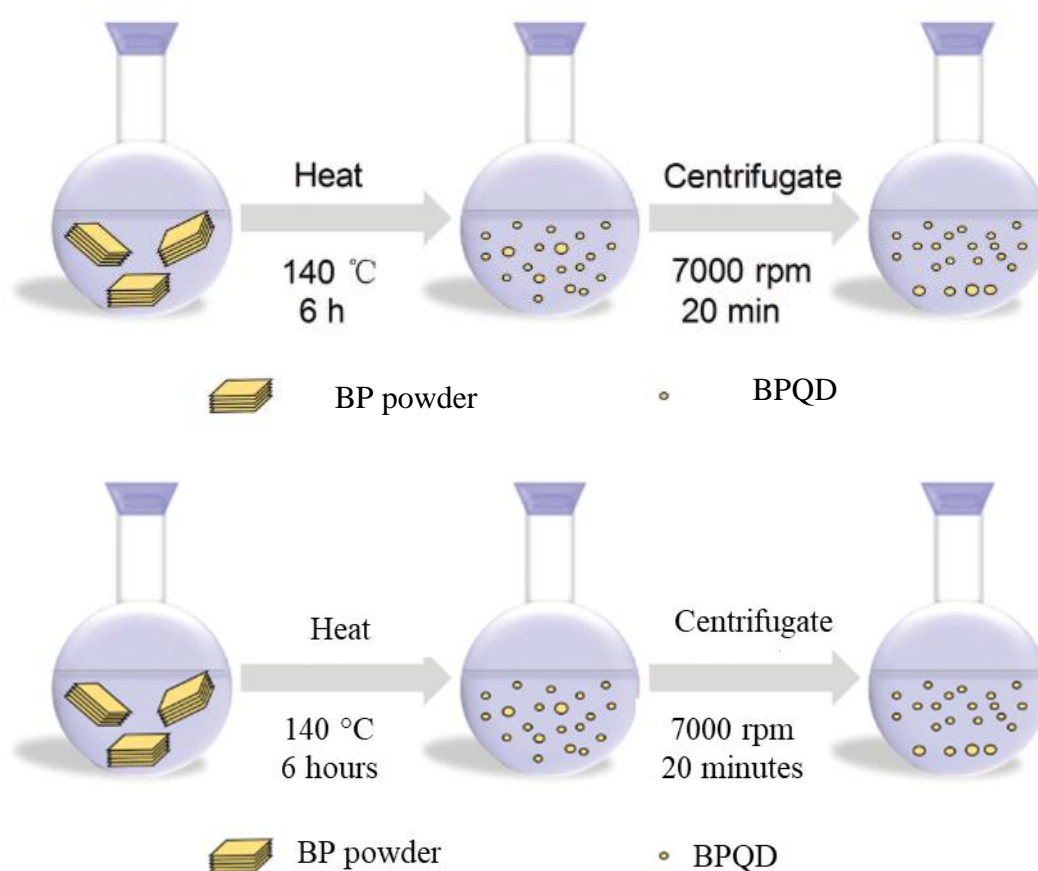


Fig. 4: Hydrothermal process of synthesizing BPQDs in NMP solution [56].

2.4.5 Hot injection method

The hot injection was proposed to synthesize lead sulfide (PbS) QD [111]. Initially, PbO, oleic acid, and 1-octadecene were heated to 120 °C inside a flask under vacuum condition to obtain transparent solution. Then, the S-precursor was prepared by adding S to the oleylamine inside the flask. Next, the S-precursor was immediately injected into the flask for the reaction to occur for 30 seconds under argon ambient condition. Subsequently, the mixture was cooled with an ice water bath and centrifuged with 12000 rpm for 3 minutes to extract the PbS QD from the ethanol

solution. Finally, the precipitate PbS QD was re-dispersed in cyclo-hexane to form a stable colloidal solution.

2.4.6 Vacuum filtration

As stated in LPE, vacuum filtration was employed to further clean or filter the synthesized material product after centrifugation process. However, a standalone vacuum filtration method was demonstrated to filter the material such as CNT from Nanointegris (Iso-Nanotubes) through Mixed Cellulose Ester (MCE) membrane to achieve several film thicknesses from 50 nm to 200 nm [112]. Besides, the fabrication of GO paper was presented by vacuum filtrating the GO suspension with a 0.22 μm PDVF membrane [113].

2.4.7 Magnetic sputtering deposition (MSD)

In contrast to LPE and CVD, MSD provides a simpler method to deposit the material on the targeted substrate with stronger linear conductivity [101]. During the deposition process, excitation is provided to an ionized Ar to bombard the high purity targets such as WS_2 [114], MoTe_2 [115] or WTe_2 [116] plasma plumes to be gradually deposited on the optical fiber, fiber tip, and silicon wafer, respectively inside a vacuum chamber. Apart from that, MSD was also employed in growing WS_2 - MoS_2 - WS_2 hetero-structure on the fiber facet inside a reaction chamber with a vacuum pressure of 1 mPa [101]. These hetero-structure layers were protected by coating a layer of ~ 300 nm thickness Au film.

3.0 SA materials

Most SAs are deployed with layered material due to the remarkable optical saturable absorption properties. A thorough review was done for SA materials which have been previously demonstrated as the mode-lockers [117][118]. An excellent mode-locker should exhibit most of these characteristics; ultrafast carrier dynamics, high nonlinear optical (NLO) response, broadband operation either with zero or scalable bandgaps, strong light-matter interaction, and ease of integration into an optical system.

3.1 SWCNT

In 2004, the earliest nanoscale mode-locker was proposed by Set et al. [22] with SWCNT-SA to generate high quality erbium-doped MLFL. The SWCNT possesses nanocylinder structure by rolling graphene sheet into tubular form as shown in Fig. 5 [119]. The fabrication of SWCNT is typically hybrid chiralities, leading to the distinct advantage as a SA candidate with high NLO susceptibilities, low saturation intensity, sub-picosecond relaxation time, broad operation bandwidth, and enhanced diameter ranging from 1.0 to 1.3 nm is in conjunction to the absorption peak at 1567 nm, which matches the optical spectrum of erbium-doped fiber laser (EDFL) [120]. Steinberg et al. [63] commented that a 1.0 nm tube diameter SWCNT is the optimized parameter to be implemented for 1.55 μm MLFL due to the analogous photon energy to EDFL as ~ 0.8 eV. Apart from C-band MLFL, the tube diameter of SWCNT

ranging from 1.3 to 1.6 nm is practical for 1.9 to 2.0 μm emission wavelength [121][122]. The first thulium-doped MLFL was demonstrated with CNT-SA in 2008 by Solodyankin et al. [123]. Additionally, Sobon et al. [112] investigated the effect of CNT thicknesses from 50 nm to 200 nm on the modulation depth (MD), centre wavelength, and pulse duration of a 1.9 μm MLFL. From the measurement, an optimized CNT thickness of 100 nm generates the shortest pulse width as 501 fs. Notably, the shortest pulse width integrating CNT-SA for thulium-doped MLFL was recorded as 152 fs in a slightly normal dispersion laser cavity after external compression [122].

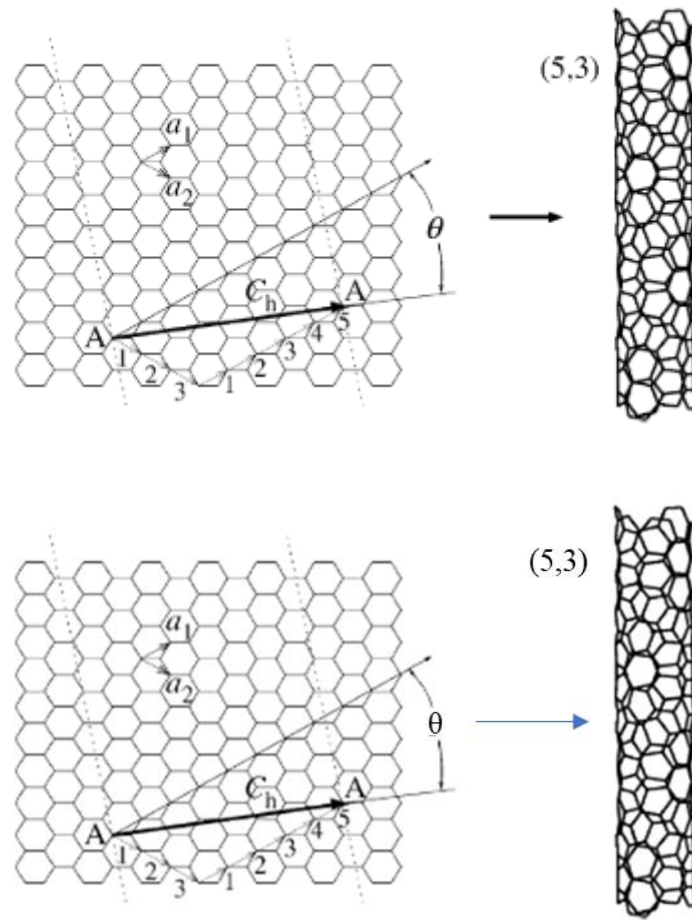


Fig. 5: Rolling of graphene sheet into tubular SWCNT [119].

The low non-saturable loss of SWCNT is always the merit of this material as a potential SA [124]. This SA characteristic can be tailored with MD through the diameter control and the reduced scattering loss of the SWCNT [125]. Both MD and non-saturable loss are higher with thicker SWCNT layers [126]. In contrary to the virtue of low non-saturable loss, SWCNT is confined as 1D material due to the high aspect ratio. The high aspect ratio of SWCNT causes the entangled morphology and ease of aggregation which degrades the distribution uniformity [127]. The formation of bundles and agglomeration affects the nonlinear absorption [128] and increases the non-saturable loss [129] of the SWCNT-SA, respectively. Higher loss is induced

when the CNT was dispersed with polymer to form the composite [112]. The chemical etching can minimize the aspect ratio or the surface energy of the SWCNT. This approach creates surface defects and thus damage the SWCNT [130]. In short, the SWCNT is recommended when chirality control and low aspect ratio are provided with an advanced material synthesis method as well as know-how tube diameter design for the desired wavelengths.

3.2 Graphene

Graphene is the first discovered 2D material [67] and was firstly proposed as SA in 2009 [23]. A review of graphene with the photonics and optoelectronics properties was done by Ferrari et al. [131]. This material possesses a honeycomb lattice formed with hybridization of sp^2 band structure. The 2D structure has awarded graphene with zero bandgap, ultra-broadband operating wavelength range from ultraviolet to terahertz, ultrafast recovery time, low saturation intensity, ease of synthesis, and flexibility of integration into fiber laser system [2][131][132][133]. Few layer graphene was presented with strong nonlinear refractive index of $\sim 10^{-7} \text{ cm}^2/\text{W}$, which is seven magnitude orders larger than other conventional bulk materials [134]. This characteristic induces significant nonlinear phase shifts for the generation of desired nonlinearity applications. Moreover, the lower saturation absorption intensity of graphene compared to SWCNT is beneficial in generating MLFL with a lower power threshold [23][135].

The thickness of monolayer graphene was measured as $0.33 \pm 0.05 \text{ nm}$ [136]. Experiments were conducted to investigate the influence of graphene layers from 1 to 15 layers [99], 3 to 12 layers [88], and 9 to 48 layers [17] on the MD. Based on these articles, higher MD was obtained with thicker graphene layers as presented in Fig. 6. Graphene acts as a SA with high crystalline quality [127]. Therefore, a minor level of structural defects in graphene will induce phonon and electron scatterings which affect the saturable absorption performance [137]. For instance, the structural defects cause higher non-saturable loss, higher saturation intensity, and lower MD [138]. The defects of the graphene can be investigated through Raman mapping characteristics, in which higher defects level is associated with increased graphene layers [139]. Despite the popularity of graphene as the SA, this material suffers from certain limitations. For instance, a hydrogen ambient environment is required in synthesizing graphene via CVD due to the ease of oxidation for this material [127]. Apart from that, the weak absorption efficiency of graphene in absolute terms is rather low as less than 2.3% of incident light per graphene layer [121][140][141]. This induces small carrier density [142] and significantly hinders the light modulation ability to strong-light interaction [106]. Moreover, the obstacle in creating optical bandgap for graphene has limited the integration of this material in optoelectronic applications [143].

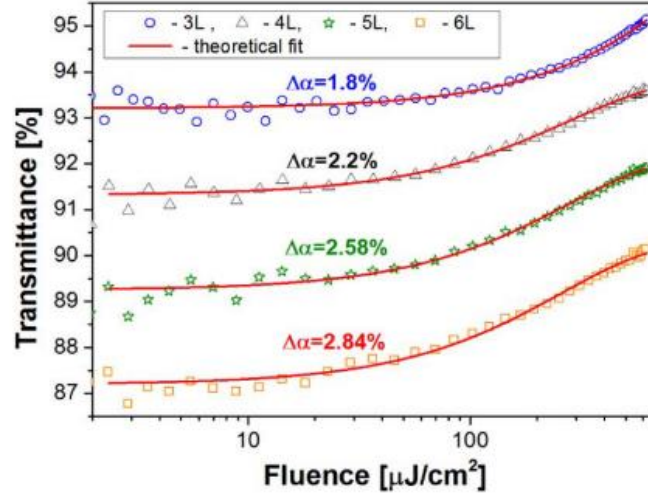


Fig 6: Nonlinear saturable transmittance from 3 to 6 graphene layers, $\Delta\alpha$ is MD [88].

The graphene oxidizes in the ambient environment to form graphene oxide (GO). The GO was experimentally proven with ultrafast carrier relaxation, large MD, and large optical nonlinearities [144][145][146]. This denotes that the oxidation of graphene primarily takes place at the edge areas which negligibly affects the ultrafast dynamics [145]. An experiment was conducted to scale the pulse width with highly soluble GO paper from 1 to 4 layers [113]. Based on the findings, the shorter pulse width was achieved with thicker GO layers. GO would be reduced to synthesize rGO, but with lower quality than pure graphene in terms of lower MD and higher defects density [147]. Ultra-small nanoparticles supported reduced graphene oxide (US-NPs/rGO) was synthesized with simultaneous reduction and GO doping through a one-step photochemical process [148]. The synthesized rGO has an average thickness of less than 3 nm, which provides strong nonlinear absorption and ultrafast nonlinear response, as well as enhancing the light-matter interaction.

Apart from that, Lin et al. [138] triturated five types of nano-scale carbon-based materials with few layer graphene nanosheet, graphite nanoparticles, GO nanoparticles, carbon black, and charcoal nanoparticles. The defect density of few layer graphene nanosheet and graphite nanoparticles is one magnitude order lower than the GO nanoparticles, carbon black, and charcoal nanoparticles. This is because GO nanoparticles are exposed to the extensive oxidation process, whereas carbon black and charcoal nanoparticles exist in the amorphous graphite phase. Higher defect density increases the non-saturable loss and reduces the MD of the SA. Therefore, few layer graphene nanosheet and graphite nanoparticles are recommended among the tested nano-scale carbon-based materials. Besides that, detonation nanodiamond (DND) was proposed with a sp^3 hybridization structure of carbon orbital, strong nonlinearity, and intensity dependence transmittance due to saturation of light absorption [149]. Despite the saturable absorption capabilities, the DND shows higher saturation intensity and larger non-saturable loss than graphene and CNT.

3.3 Other organic carbon materials

Glycerin is an organic liquid with a conjugated chain structure, composed of carbon hydrogen bonds (C-H), carbon oxygen bonds (C-O), oxygen-hydrogen bonds (O-H), and carbon-carbon bonds (C-C) [150]. This material has a broadband absorption ranging from 1500 to 2000 nm owing to the stretching vibration and flexural vibration of different covalent bonds [150]. Glycerin shows the advantages of less volatility and lenient packaging challenges to keep the mode-locking abilities to typical alcohol [151]. Next, graphdiyne is a newly discovered all carbon nanostructured materials with a planar layer of atomic thickness comprising of sp and sp² hybridization [152]. The carrier mobility of graphdiyne is about 10⁴ to 10⁵ cm² (V s)⁻¹ at room temperature [153]. Different from the zero band gap of graphene, the graphdiyne has a direct bandgap measured from 0.46 to 1.1 eV [154]. The flexible bandgap of the graphdiyne enables this material to exhibit excellent nonlinear optics properties, particularly the nonlinear refractive index of the graphdiyne is reported up to 10⁻⁵ cm²W⁻¹ which is suitable for multifunctional photonic devices [155].

3.4 Transition metal dichalcogenides (TMD)

TMD is a 2D anisotropic layered compound, typically formulae as MX₂, in which M is the transition-metal atom from the group IV, V, or VI columns of the periodic table such as molybdenum and tungsten, whereas X is one of the chalcogens, sulphur, selenium, or tellurium [144][156]. The TMD possesses a strong covalent bond in the atoms within the layers and weak Van der Waals' force between the stacked individual layers [68][157]. These bonding facilitate the exfoliation of the TMD into single or few layer structures. The characteristics of TMD bandgap are highly dependent on material thickness. For instance, bulk and monolayer TMD such as WS₂ was characterized as indirect and direct bandgap, respectively [68]. Moreover, the electronic properties of the TMD are determined by the coordination and oxidation states of the M atoms, which can be presented with metal, semiconductor, or insulator [158][159]. Therefore, the thickness-dependent bandgap and electronic band structure of TMDs are attractive in contrast to graphene, especially for optoelectronics applications.

The four most popular studied TMDs are MoS₂, WS₂, MoSe₂, and WSe₂ [160]. The MoS₂ and WS₂ have spurred huge research interests to replace graphene due to ultrafast carrier dynamics [161] and strong third-order NLO response in few layer structures [162]. For instance, MoS₂ was not only presented with faster ultrafast saturation absorption than graphene for femtosecond pulse in 800 nm [163], but also shown with higher optical nonlinear response than graphene [94]. However, MoS₂ has a lower optical damage threshold than graphene due to weaker thermal conductivity and mechanical characteristics [94]. In addition, monolayer MoS₂ shows a similar disadvantage to graphene in terms of oxidation issue under high-energy laser irradiation and weak light-matter interaction thus hinders the modulation of the laser pulse [164][165]. As a result, multilayer MoS₂ is more suitable than monolayer MoS₂ to generate MLFL. The current status and future development of MoS₂ in MLFL was thoroughly reviewed in [166].

Bulk MoS_2 and WS_2 are indirect semiconductor which consists of metal atoms positioned in between two layers of chalcogen atoms [167]. The bandgaps for a bulk MoS_2 and WS_2 are 1.29 and 1.35 eV, respectively [44]. Due to the thickness-dependent properties, monolayer MoS_2 exhibits a direct bandgap of 1.9 eV [157], whilst monolayer WS_2 shows the direct bandgap of 1.3 eV [43]. Wang et al. [168] demonstrated the reduction of optical bandgap in MoS_2 from 1.08 to 0.08 eV by introducing sulfur defects to MoS_2 . The reduction of the bandgap is achieved when the Mo:S ratio was increased from 2 to 2.09. In this regard, the lower bandgap is attained with heavier chalcogen atoms [87]. The reduction in bandgap is beneficial for longer wavelength operation which addresses the limitation of large bandgap TMD to be integrated into infrared (IR) region [169]. In terms of the application as SA, the first MoS_2 -SA was proposed in 1.06 μm MLFL by Zhang et al. [24], whereas the first WS_2 -SA was demonstrated in 1.56 μm MLFL by Mao et al. [68].

In comparison to MoS_2 and WS_2 , MoSe_2 and WSe_2 exhibit similar molecular structures with lower bandgap due to larger mass of Se than S chalcogen atoms. In particular, bulk MoSe_2 and WSe_2 have indirect bandgap with 1.09 and 1.20 eV, respectively [44]. Moreover, monolayer MoSe_2 and WSe_2 exhibit a direct bandgap of 1.57 and 1.67 eV, respectively [170]. Figure 7 compares the experimental and theoretical measurement for the bandgaps of MoS_2 , WS_2 , MoSe_2 , and WSe_2 in bulk and monolayer forms through photoluminescence (PL). The lower bandgap between monolayer and bulk TMDs with Se in contrast to S chalcogen atoms provides a broader saturable absorption band for MLFL [67]. Nevertheless, the selection of TMD with Se chalcogen is restricted to weaker chemical reactivity than S chalcogen atom [85].

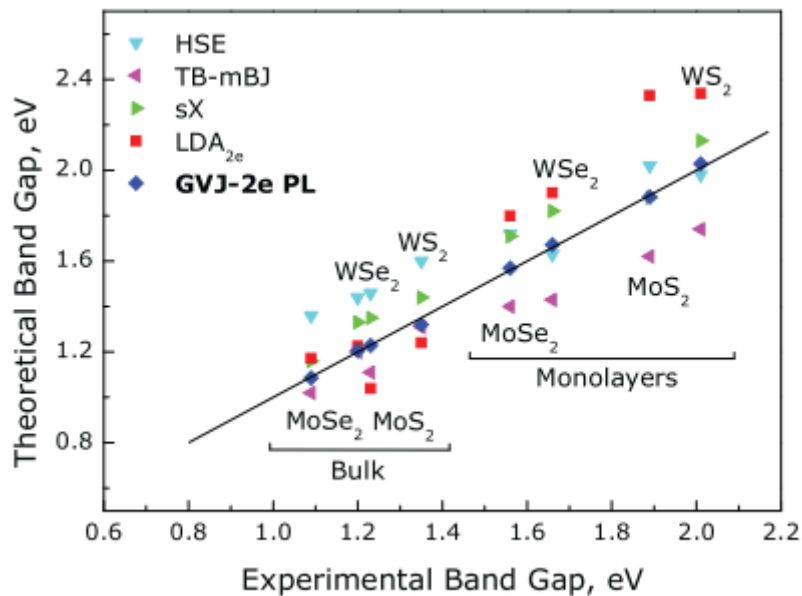


Figure 7: Comparison of theoretical and experimental bandgap for TMDs with PL. HSE, TB-mBJ, sX, and LDA_{2e} values are referred from literatures [170].

Titanium disulfide (TiS₂) and platinum diselenide (PtSe₂) possess typical TMD characteristics with scalable bandgap due to the exfoliation feasibility at the weak Van der Waals' force between the interlayer bonding. The bandgap of TiS₂ is scalable by tailoring from 0.05 to 2.5 eV, showing the characteristic of semiconductor [171]. Therefore, TiS₂ has nearly zero bandgap structure with broadband NLO response from 400 to 1930 nm, high carrier mobility, and good electrical conductivity [106]. On the other hand, PtSe₂ exhibits widely tunable bandgap from indirect bandgap of 1.2 eV for monolayer, 0.21 eV for bilayer and zero bandgap for more than trilayer structures [172]. Therefore, the PtSe₂ can be designed in either semiconductor or semi-metal by tailoring the number of layers [173]. Significantly, PtSe₂ is a good alternative to graphene, in addition to tunable bandgap characteristics by layer and defect engineering [174]. Additionally, PtSe₂ possesses high carrier mobility of more than 3500 cm²·V⁻¹·s⁻¹, which generates a fast NLO response towards incident light to achieve ultrashort pulses [92][175].

Rhenium disulfide (ReS₂) is another TMD with weak interlayer coupling in the 1T structure [176]. The weak interlayer coupling results in nearly identical band structure for the monolayer and bulk forms of ReS₂ [93]. Particularly, monolayer and bulk ReS₂ exhibit direct bandgap with 1.44 and 1.35 eV, respectively [177]. This characteristic is different from conventional TMDs with thickness-dependent bandgap. Hence, ReS₂ is more rigid in terms of operating wavelength and absorption intensity [93]. In contrast to other SA material which is easily oxidized, ReS₂ exhibits better environmental stability [176]. Moreover, the anisotropic NLO characteristic of ReS₂ is suitable for the SA application [178]. A similar layer-independent bandgap and anisotropic crystal structure to ReS₂ was shown in tin disulphide (SnS₂) with nonlinear absorption coefficient of 9.9×10^{-10} m/W [58]. However, a bulk SnS₂ is semiconductor with an indirect bandgap of 2.2 eV, in which the bandgap characteristic is maintained for monolayer structure as 2.033 eV [41]. In addition, tin diselenide (SnSe₂) is another TMD material with a hexagonal close-packed layered structure with each Sn atom octahedrally surrounded by six Se atoms [179]. SnSe₂ exhibits an electronic bandgap of 0.94 eV, 1.51 eV, and 1.29 eV for bulk, monolayer, and bilayer nanosheet structure [180]. Palladium disulfide (PdS₂) has a pentagonal crystal structure different from the hexagonal structure which was normally seen in MoS₂ or WS₂. A monolayer PdS₂ was found to have an indirect bandgap of 1.6 eV [181], whereas a bilayer to bulky PdS₂ exhibits semi-metallic properties [182].

Two experimental works were reported on indium selenide with different chemical formulae, InSe in 1.06 μm MLFL [79] and In₂Se₃ in 1.55 μm MLFL [183]. The InSe consists of covalently bonded Se-In-In-Se atomic planes, whereas the In₂Se₃ consists of covalently bonded Se-In-Se-In-Se quintuple planes. Few layer InSe has an indirect bandgap of 1.4 eV, whereas the bulk InSe exhibits 1.2 eV bandgap due to the suppression of interlayer coupling [79]. On the other hand, the bandgap of In₂Se₃ is highly layer-dependent, 1.45 eV for thick nanosheet, and 2.8 eV for 3.1 nm thin nanosheet [183]. Therefore, the bandgap characteristic of InSe is close to ReS₂,

whereas thin In_2Se_3 nanosheet has the largest bandgap among the aforementioned TMDs, which is not recommended for MLFL in IR range. A new chalcogenide material, titanium trisulfide (TiS_3) was also reported with thickness related bandgap structure such as those observed in MoS_2 . For instance, a bulk TiS_3 has an indirect bandgap of 0.94 eV, whereas a monolayer TiS_3 has an indirect bandgap of 1.02 eV [81].

Apart from S and Se chalcogen, Te chalcogen was demonstrated for Mo and W metals. The molybdenum telluride (MoTe_2) achieves the shortest pulse duration of 229 fs among the TMDs in 1.55 μm MLFL and was firstly demonstrated in 2 μm MLFL [115]. The monolayer MoTe_2 has a direct bandgap of 1.1 eV and an indirect bandgap of 0.93 eV for bulk crystal [42]. These bandgaps are not feasible for ytterbium-doped fiber laser (YDFL). In comparison to the aforementioned five TMDs, monolayer WTe_2 has the smallest direct bandgap value of 0.7 eV, which is suitable for longer waveband applications [184].

Despite those numerous demonstrations on TMD-SA have been presented in recent works, MoS_2 -SA receives the most attention for MLFL. Therefore, research efforts were spurred to improve the performance of MoS_2 -SA with GO/ MoS_2 hetero-structure [164]. This structure was synthesized by wrapping the surface of MoS_2 nanosheet with a monolayer GO membrane. Therefore, the advantages of both materials are presented with resistance properties of GO to overcome the oxidation issue of MoS_2 nanosheet, whereas the strong light-matter interaction of MoS_2 addresses the weak absorption efficiency of monolayer GO [157]. In addition, graphene- WS_2 [185], MoS_2 - WS_2 [186] and WS_2 - MoS_2 - WS_2 [101] hetero-structures have been proposed with enhanced light-matter interaction and ultrafast NLO properties. In particular, the NLO properties of these 2D monolayer hetero-structures are scalable with optical bandgap from near-IR to the visible spectral range by stacking different TMDs or utilizing different thickness of each layer. Apart from that, a recently proposed monolayer hafnium disulfide (HfS_2) shows carrier mobility of $1800 \text{ cm}^2 \text{ V}^{-1} \text{ s}^{-1}$, broadband absorption from 200 to 2000 nm, and smaller bandgap than monolayer MoS_2 as 1.2 eV [48]. This TMD may appear to be a new alternative to MoS_2 in generating MLFL in a longer wavelength.

Conventional TMD shows several limitations. The large bandgap of some bulk TMDs in visible and IR regions limits the applications in optoelectronic devices [56][140]. Another issue of the TMD is the low optical damage threshold when exposed to high power illumination [162]. In summary, TMD is recommended with larger MD than graphene and scalable bandgap properties with flexible defect engineering. However, the integration of TMD-SA in high power applications should also take the low optical damage threshold issue of the TMD into account with better heat dissipation mechanism.

3.5 Transition metal oxides

An atomic layer thickness molybdenum trioxide (MoO_3) was demonstrated with enhanced plasmonic resonance for nonlinear saturable absorption, providing an MD of 34.96% in contrast to pristine MoO_3 nanosheet with MD of 19.31 % [142]. The NLO response of the 2D plasmonic MoO_3 with an intense optical field is triggered by strong light-matter interaction and structural low dimensionality. In particular, the proposed MoO_3 possesses 200 fs of hot electron relaxation time with fast switching behaviour, which makes MoO_3 a suitable SA candidate. Nevertheless, this MoO_3 -SA was integrated into 1.06 μm MLFL. Next, Fe_3O_4 was lately reported for its high nonlinear optical absorption, large third-order optical nonlinearity, and ultrafast response time which is suitable to be an excellent SA [187].

3.5 BP

BP is a 2D material with basic cells of intrinsic in-plane anisotropy and puckered-honeycomb structure, possessing strong light-matter interaction and tunable direct-bandgap over broadband wavelength [3][66][77][140][188]. A simple method to synthesize BP is by direct heating the red phosphorus with 1000 °C at 10 kbar constant pressure inside an anvil-type apparatus, and the temperature was reduced to 600 °C with a cooling rate of 100 °C per hour [189]. Among different kinds of phosphorus such as white, red, and violet phosphorus, BP is most thermodynamically stable with high carrier mobility [3][56]. The high carrier mobility of BP was measured as 1000 $\text{cm}^2/(\text{V.s})$ [190], contributed by the direct bandgap characteristic [66]. In comparison to the zero bandgap graphene and conventional TMD with typical large bandgap, BP shows direct bandgap characteristic for all thicknesses [77], as well as scalable bandgap from 0.3 to 2.0 eV for bulk and monolayer BP structures, respectively [52]. This benefits the ultrafast carrier dynamics for MLFL in broadband wavelengths from visible spectral region to 1930 nm [191], 2100 nm [192], 2800 nm [52], and 3680 nm [140]. Apart from that, BP is attractive in terms of tunable linear and nonlinear optical properties by the film thickness [189], and higher absorbance per layer of 2.8% than graphene [193]. Strong third order NLO response promises BP as a SA candidate with a measured nonlinear refractive index of $10^{-5} \text{ cm}^2/\text{W}$ and third order nonlinear susceptibility of 10^{-8} e.s.u. [194].

However, BP shows the limitation in poor environmental stability towards photo-oxidation or water absorption within several hours to days, especially for monolayer and few-layer BP structures [169][195][196]. The induced defects by this issue alter the electronic band structure of BP [197]. Several suggestions have been proposed to solve the oxidation issue in BP such as encapsulate BP with polymer matrix [198] or using NMP to exfoliate BP [56][75]. Despite this established issue for BP, an oxidized BP (OBP) was commented with comparable saturable absorption to BP with similar direct bandgap characteristic [64]. The oxygen-induced defects contribute to the self-defocusing mechanism in OBP, which enhances the nonlinear refractive index [197]. Moreover, the bandgap of OBP is scalable with 1.178, 1.206, and 0.536 eV for $\text{PO}_{0.125}$, $\text{PO}_{0.25}$, and $\text{PO}_{0.5}$, respectively [197]. Significantly, BP substitutes graphene

with higher absorbance per stacking layers and recommended with broadband wavelength operation.

3.7 QD materials

QD is an ultra-small size, zero dimensional (0D) nanomaterials [199] with scalable bandgap by quantum confinement and edge effects [200]. QD Materials have stronger third order nonlinearity than the bulk material and tunable absorption wavelength by changing the size of QD [105].

The BPQD is dubbed as phosphorene. The bandgap of phosphorene decreases with thicker layers. For instance, 1.73 eV, 1.15 eV, 0.83 eV, and 0.35 eV were measured in mono-, bi-, tri-layers, and bulk phosphorene, respectively [3]. The synthesis of phosphorene was demonstrated through LPE method with a lateral size of $2.6 \text{ nm} \pm 0.9 \text{ nm}$ [49] and a thickness of 1.5 nm [201]. In addition, a smaller lateral size phosphorene of $2.1 \text{ nm} \pm 0.9 \text{ nm}$ was synthesized through the solvothermal method with NMP solvent [56]. NMP protects the phosphorene dispersion from degradation [49]. Phosphorene is recommended as an alternative to BP, which has been demonstrated with a saturation intensity of two magnitude orders lower than BP nanosheet [56].

Antimonene is a mono-elemental material purely consisting of antimony (Sb) [61]. Antimonene possesses excellent thermal conductivity [202], strained-induced band transition [203], high carrier mobility and covers a bandgap from 1.18 to 2.28 eV in α - and β -phases, respectively [204]. Moreover, antimonene has direct bandgap properties in α -phase whereas indirect bandgap is presented in β -phase [204]. However, the indirect bandgap of antimonene in β -phase is not recommended as the SA, which causes low photoelectric response thus restricts the integration for ultrafast photonics application [71]. In comparison to phosphorene, antimonene has a larger absorption cross section at the cost of lower stability [81].

Bismuthene is a mono-elemental semiconductor with a low-buckled hexagonal structure [205]. Zhang et al. [204] proposed the direct bandgap of α - and β -phases for the bismuthene as 0.36 eV and 0.99 eV, respectively. This promises bismuthene as broadband optical material for terahertz (THz), mid-IR and near-IR regions. For instance, bismuthene was presented with broadband absorption from 300 to 1680 nm with absorption peak values from 0.747 to 1.028 eV by stacking the bismuthene from one to six layers [57]. Bismuthene shows enhanced stability in terms of electronic and mechanical properties than the aforementioned QDs at the cost of lower nonlinear refractive index and third order nonlinear susceptibility than BP [57]. In summary, bismuthene is recommended in designing SA with high stability from near-IR to THz range.

Tellurene was lately discovered as a single layer form of bulk tellurium in group VIA. The first 2D tellurene was synthesized with 30 nm thickness by van der Waals epitaxy growth [206]. An experimental work has been done to prove the stability of 2D

tellurene in nature, with a 2-3 orders of higher carrier mobility than MoS₂ [207]. A monolayer tellurene was prepared by MBE technology and the bandgap is controllable from 0.33 eV to 0.92 eV for the bulk tellurium and tellurene, respectively [208].

PbS-QD is a group IV-VI semiconductor with a large Bohr exciton radius of 18 nm, high third order nonlinearity coefficient, multiple exciton generation, and tunable bandgap by modifying the thickness of QD [209][210][211]. The bandgap of PbS-QD 0.41 eV for bulk material [111] and experimentally measured as 0.8 to 1.15 eV by reducing the thickness of PbS-QD from 8 to 4 nm [210]. In addition, PbS-QD was investigated in broadband absorption from 1000 to 1650 nm as shown in Fig. 8 [111]. The high linear absorption in 1.06 μm and 1.55 μm denotes the potential of PbS-QD as the SA. However, the PbS-QD has only been demonstrated as the SA in C-band MLFL [111][209]. Therefore, further investigation on PbS-QD in different wavebands, especially 1.06 μm is recommended due to the strong linear absorption in this band which is supported by a 4 nm thickness PbS-QD with the bandgap of 1.15 eV [210].

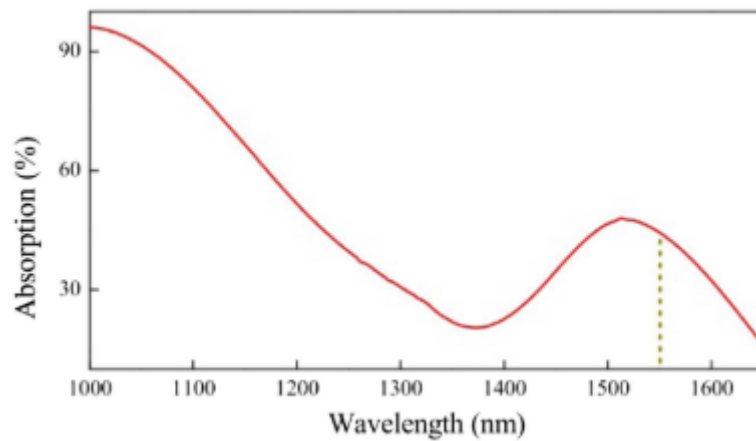


Fig. 8: Linear absorption spectrum of PbS-QD [111].

3.8 Gold nanorods (GNRs)

GNRs are plasmonic rod-shaped gold nanoparticle with uniform shape and narrow size distribution, which has been extensively synthesized through seed-mediated growth [212][213][214][215]. GNRs have large third order nonlinearity, fast response time, good compatibility with optical fiber, controllable aspect ratio to shift the localized surface plasmon resonance absorption peaks from 800 to 1500 nm, and broadband absorption from 1000 to 3000 nm [212][213]. The aspect ratio of GNRs can be widely tuned in longitudinal surface plasmon resonance (SPR) absorption peak [214]. The tunable aspect ratio is beneficial in providing different wavebands for the GNRs. For instance, an average aspect ratio of ~ 4.5 is employed for 1.06 μm MLFL [216], whereas the 1.56 μm MLFL was demonstrated with the average aspect ratio of 5.5 [217]. However, an intrinsic limitation of GNRs during the synthesis process is

the photo-thermal effect which would optically damage the GNRs [218]. In addition, the photo-thermal effect with high peak power limits the pulse duration to a maximum of up to tens of picoseconds [216][217]. The photo-thermal effect was addressed by the integration of microfiber [219] or coating the GNRs with SiO₂ to form the core/shell structure [215]. Both mechanisms improve thermal stability and preserve the intrinsic properties of GNRs. In summary, GNRs are recommended as broadband SAs by controlling the aspect ratios. Nevertheless, the research gap on GNRs in longer wavebands than 1.56 μm MLFL is yet for further investigation.

3.9 Metal-organic framework (MOF)

MOF is a porous crystalline material that is built from transition metal joints and organically linked to form nanometer-sized space, large surface area, and ordered crystalline structure [107]. A crystalline nickel-p-benzenedicarboxylic acid MOF (Ni-MOF) was presented with a 2D layered structure and tunable bandgap from 0.85 to 3.12 eV by decreasing the doping of Ni-ions in MOF [107]. Moreover, the Ni-MOF was investigated with broadband NLO response from 800 to 1800 nm and optical amplitude modulation for optoelectronics applications. The Ni-MOF was employed in the generation of both 1.06 and 1.56 μm MLFLs. Nevertheless, the demonstration of MOF as SA is still in the infancy stage, which requires further exploration of the saturable absorption properties of MOF in ultrafast laser.

3.10 Silicon carbide (SiC)

SiC is a semiconductor containing silicon and carbon. Cheng et al. [220] demonstrated a phase-epitaxial CVD-grown SiC film with C:Si composition ratio of 1.83 to transform the two-photon absorption to nonlinear saturable absorption. In particular, the transmittance of SiC decreases from 0.68 to 0.3 when the C:Si composition ratio was reduced from 1.83 to 0.51. Therefore, low silicon composited SiC or C-rich SiC is desirable for MLFL due to lower intra-cavity loss. Moreover, a C-rich SiC possesses sp^2 orbital hybridization to reduce the lattice constant and effective mass than sp^3 orbital hybridization thus increasing the nonlinear refractive index. The highest nonlinear refractive index is achieved when SiC is designed with a similar lattice structure to graphene. In contrast to graphene, SiC is recommended due to intrinsic advantages such as higher thermal damage threshold [221] and wider choices of the substrates for deposition, such as glass, quartz, and silicon [220].

3.11 Deoxyribonucleic acid (DNA)

The aforementioned nanomaterials may affect human health after long term exposure [222]. Therefore, bio-compatible alternative drives the research avenue into a more environmentally friendly and non-hazardous material as the SA. In this regard, two types of DNA thin films were employed for the ultrafast erbium-doped MLFL generation, DNA in aqueous solution and, DNA-cetyltrimethylammonium chloride (CTMA) in organic solvent [223]. DNA/CTMA film was presented with higher nonlinear absorption coefficient as $8.89 \times 10^{-9} \text{ m/W}$, larger nonlinear refractive

index as $1.82 \times 10^{-11} \text{ cm}^2/\text{W}$, and larger third order susceptibility as $4.11 \times 10^{-9} \text{ e.s.u.}$ than pure DNA film as $1.78 \times 10^{-9} \text{ m/W}$, $3.44 \times 10^{-12} \text{ cm}^2/\text{W}$, and $8.42 \times 10^{-10} \text{ e.s.u.}$, respectively at 1570 nm. These characteristics offer DNA/CTMA film a better SA than DNA film with a shorter pulse duration of 323 fs. In summary, the investigation on DNA-based SA is bio-compatible which brings less hazardous syndrome to human health and is recommended for further analysis as a potential SA candidate.

4.0 SA material with polymer

Polymer is employed to form a composite with SA material or deposited on the material film as the protective layer. The polymer assists the SA for the integration into MLFL system due to fabrication feasibility such as embossing, stamping, sawing, as well as dry and wet etching in a cost effective room-temperature fabrication condition [55]. A suitable polymer to form the composite with SA material should possess most of these characteristics, such as high transparency at the MLFL operating wavelength, as well as mechanically, thermally, and chemically stable in various harsh circumstances to reduce non-saturable losses [55]. In addition, the formation of material-polymer composite contributes to larger nonlinear absorption, especially in monolayer or few-layer graphene [224].

Several types of the polymer have been demonstrated to form thin film, dispersion, or composite with the SA material. An example of the polymer is polyvinyl alcohol (PVA), which has a smooth surface, mechanically stable, colourless and highly soluble in water [62][125][135]. The PVA was employed to form the composite with numerous SA materials, such as SWCNT and GO [126], MoS₂ [69], WS₂ [68][50], MoSe₂ [11][67][225], WSe₂ [44], ReS₂ [70], SnSe₂ [226], MoO₃ [142], PbS/CdS-QD [209], and PtAg/N-G nanoparticles [62]. Significantly, the PVA is invulnerable to a humid environment and strongly absorbed from 1300 to 1700 nm due to the presence of O-H bonds [55]. Hypothetically, these issues appear to be the disadvantages of PVA. In the contrary, these characteristics recommend PVA to form a composite with water-dispersed SA materials due to high water solubility, which is absent in other polymers such as PMMA and polydimethylsiloxane (PDMS). Moreover, another limitation of PVA and other polymers is the generation of higher optical loss, which was presented with a reduction in transmittance from 92 to 86 % when PVA was employed to form a composite with SA material [79].

Apart from that, PVA was used together with PMMA as the stacked layer on a glass substrate for the deposition of MoS₂ flakes with adhesive tape as support [45]. Next, the stacked substrate with MoS₂ flakes was immersed in DI water bath for 24 hours to remove the PVA layer and the MoS₂/PMMA film was detached from the glass substrate. Moreover, PMMA layer is frequently employed in CVD-grown material to transfer the thin film between two substrates [85]. A polymerized PMMA heated to 120 °C increases the adhesion force of monolayer graphene [89][227], multilayer graphene [88], graphite [36], and WS₂ [227] on the fiber substrates such as D-shaped fiber and tapered fiber. The PMMA layer can be etched away with acetone solution,

leaving only the SA materials on the fiber substrate [91][227]. Based on [53], the etching of PMMA layer improves the SA transmission by 16 %. Hence, the PMMA is mostly employed as a layer-structured to assist the deposition of SA material on the desired substrate, rather than forming a composite with the SA material.

In contrast to PMMA with a refractive index of 1.49 [227], PDMS forms the material/polymer with a lower refractive index of 1.404 [224]. A simulation work presents that the refractive index of pure PDMS and the composite is almost similar [224]. The PDMS was demonstrated to form a composite with graphene at a lower refractive index than conventional silica fiber core to allow light propagation through total internal reflection (TIR) [228]. The graphene/PDMS composite is important to fabricate SA with a microfiber structure. This is because the deposition of pure graphene dispersion or film with a higher refractive index on the evanescent region will tremendously increase the optical loss and light scattering to the ambient environment due to the absence of TIR. However, the PDMS can only be dispersed in an organic solvent such as NMP, IPA, and chloroform, which is reverse to PVA.

Sodium carboxymethylcellulose (Na-CMC) has been demonstrated as both dispersant and host-polymer for the fabrication of SWCNT-SA [60][229]. In contrast to PVA with strong moisture absorption at 1.5 μm , Na-CMC is more stable to a humid environment and possesses higher transmittance [125]. However, both water-soluble PVA and Na-CMC provide flexible control over parameters such as thickness of polymer film, physical orientation, distribution and bundle size of SWCNT within the composite [230]. Apart from SWCNT, Na-CMC was mixed with mesoporous carbon nanospheres (MCNs) [231] and GNRs [214] to form thin film composite. The Na-CMC/MCNs and Na-CMC/GNRs composites possess strong absorption from 500 to 2500 nm and from 400 to 1800 nm, respectively. Significantly, pure Na-CMC has weak absorption within the wavelength ranges in both works thus contributing a negligible effect on the saturable absorption performance.

Styrene methyl-methacrylate (SMMA) forms a surfactant-free nanocomposite with graphene, presenting broadband optical transparency from 200 to 3000 nm, high glass transition temperature, and high stability in 60 °C humid environment at the cost of low moisture absorption [55]. NMP was found to be a good solvent to SMMA in exfoliating graphene effectively without surfactants thus synthesizing low defect graphene/SMMA composite [55]. Apart from graphene/SMMA composite, chitosan was proposed with flat absorption from 1520 to 1620 nm with high transmission over 90 % to form the composite with graphene [232]. However, both chitosan and NMP are harmful to human health [67]. In addition, the integration of polymer may degrade the optical damage threshold of the SA due to the low softening point of the polymeric film [112][143]. The advantages and drawbacks of the proposed polymers are summarized in Table 3, which provides better insight to the readers in designing composite-based SAs.

Table 3: Advantages and disadvantages of polymers.

Polymers	Advantages	Disadvantages
PVA	<ol style="list-style-type: none"> 1. Mechanically stable. 2. Easily forms composite with SA material. 3. Highly soluble in water. 	<ol style="list-style-type: none"> 1. Non-soluble in organic solvent.
PMMA	<ol style="list-style-type: none"> 1. Transfer CVD-grown material between two substrates. 2. Increases adhesion force of material to the substrate. 3. Can be easily etched away with acetone solution. 	<ol style="list-style-type: none"> 1. Commonly employed as supporting layer rather than direct interaction to SA material to form the composite.
PDMS	<ol style="list-style-type: none"> 1. Low refractive index. 2. Stable refractive index even in composite form. 2. Enhances TIR in microfiber-SA. 	<ol style="list-style-type: none"> 1. Non-soluble in water.
Na-CMC	<ol style="list-style-type: none"> 1. Acts as both dispersant and polymer. 2. Stable in humid environment. 3. Flexible control over physical mechanism of the composite. 	<ol style="list-style-type: none"> 1. Low absorbance from 400 to 2500 nm.
SMMA	<ol style="list-style-type: none"> 1. Broadband optical transparency. 2. High glass transition temperature. 	<ol style="list-style-type: none"> 1. Low moisture absorption.
Chitosan	<ol style="list-style-type: none"> 1. Flat absorption from 1520 to 1620 nm. 2. High transmission of more than 90 % from 1520 to 1620 nm. 	<ol style="list-style-type: none"> 1. Harmful to human health.

5.0 SA structure and deposition techniques

Fiber ferrule structure provides the easiest SA structure with excellent fiber compatibility and flexibility. This structure integrates the material between two fiber ferrules via a fiber connector in a sandwich structure or depositing the material on the fiber end facet as the SA mirror. Several techniques of depositing material on the fiber ferrule have been proposed such as transferring the thin film between two fiber ferrules [128], optical depositing the material around the fiber core region of the fiber ferrule with continuous wave laser [102][233], electron beam evaporating carbon atoms from nickel source surface on the fiber ferrule [234], and inkjet printing the material on a polyethylene terephthalate (PET) substrate [72]. Notably, a fiber ferrule SA was proposed by wrapping the ethanol around the fiber ferrule with polyethylene (PE) film and further coating with paraffin to avoid the evaporation of ethanol [151]. Apart from single-mode fiber ferrule, BP flakes were sealed between the fiber ferrule of fluoride gain fiber (FGF) and power-delivering multimode fluoride fiber (PDMFF) to form the SA [37]. Moreover, the fiber ferrule SA mirror was employed by coating the SA material with gold-coated end facet using graphene [127], graphite carbon

nitride [109], MoS₂ [163] and BP [52]. The generation of soliton pulse in reflection-type SA is simpler than transmission-type SA due to the simultaneously enlarged nonlinearity-induced self-amplitude MD when interacting with the material twice in the retro-reflector design [127]. However, fiber ferrule SA structure shows several limitations such as weak absorption due to short interaction length to the material [96], laser scattering, mechanical and thermal damage which are contributed by physical contact between fiber ferrule and the SA material [235]. For instance, the interaction length by placing the SA materials between the fiber ferrule is less than depositing around the microfiber [93]. The evanescent field interaction of the microfiber makes full use of the nonlinear absorption of the materials rather than fiber ferrule SA [236]. Moreover, fiber ferrule SA shows a lower damage threshold than microfiber-SA, since the illumination is focused on the material and the physically touching mechanism causes the aforementioned damages to the material [89]. In particular, the thermal damage causes pulse breaking thus limiting high power application [224].

The microfibers are composed of D-shaped fiber and tapered fiber. The D-shaped fiber is fabricated by polishing a polymer-stripped bent optical fiber [53][177]. Several techniques of depositing material on the D-shaped fiber have been demonstrated such as film attachment [2][227], drop casting with nanosheet solution [107], scotch tape exfoliation and stamping on the D-shaped fiber [36], immersion in nanosheet solution which has good resistivity to oxidation [235], in-situ deposition [234] and pulsed laser deposition [237] by bombarding material atoms to the fiber interface, as well as optical deposition of nanosheet dispersion with continuous wave laser through in-situ optical loss monitoring [44][68]. The D-shaped fiber is attractive due to long nonlinear interaction length, high optical damage threshold, and high compatibility to optical fiber and scalable MD by adjusting beam power [54][90][96][238]. Moreover, D-shaped fiber has lower evanescent wave intensity interacting with the SA than fiber ferrule SA thus generating higher output power [235]. In contrast to tapered fiber, the D-shaped fiber is more robust [93]. However, D-shaped fiber SA shows the limitation in generating polarization dependent loss (PDL) based on transverse electric (TE) and transverse magnetic (TM) polarizations. For instance, the TE and TM losses of D-shaped fiber SAs with graphene, ReS₂ and MoS₂ are measured as 20 dB and 6.1 dB [227], 4.4 dB and 2.6 dB [93], and 21.9 dB and 5.84 dB, respectively [45]. The PDL causes instability in SA performance which requires precise control of polarization state.

Tapered fiber shows a similar advantage to D-shaped fiber by providing a non-blocking configuration [89]. Apart from the conventional fused tapering procedure, a chemical wet etching technique was demonstrated to fabricate tapered fiber with a non-toxic solution of NH₄F and (NH₄)₂SO₄ [228]. Tapered fiber provides evanescent interaction with the SA material which efficiently improves the optical damage threshold due to good heat dissipation mechanism and induces large modulation due to long nonlinear interaction length [86][162]. Several techniques of depositing material on the tapered fiber have been presented such as covering the tapered fiber

with a thin film on an MgF_2 substrate [51] and optical depositing the nanosheet solution on the cross section of the tapered fiber with ASE light source [64] or continuous wave laser via in-situ monitoring [49][65][213]. In addition, numerous techniques have been proposed to improve the conventional film transfer and optical deposition methods. For instance, a dry transfer method was demonstrated by integrating polyethylene terephthalate and silica gel to transfer the thin film with cleaner procedures, low doping level, high optical conductivity and high transmittance in contrast to transfer method using thermal release tape or PMMA [92]. Moreover, a material-clad tapered fiber structure was proposed by wrapping graphene [89][141] or monolayer MoS_2 [94] films around the tapered fiber to increase the area of the evanescent field for light matter-interaction and improves the optical damage threshold. Next, an inner air cavity was fabricated inside an optical fiber by femtosecond laser machining and fusion splicing, showing better robustness and stronger evanescent field than tapered fiber [239]. The nanosheet solution is spin coated on the surface of this optical fiber and the solvent inside the inner air cavity is evaporated to generate the SA. Though, tapered fiber is polarization sensitive with dissimilar absorption in TE and TM modes [59][92]. In addition, tapered fiber is fragile and induces evanescent optical loss due to the small core size [212]. Significantly, the tapered fiber should be fabricated with low insertion loss to reduce the scattering for precise deposition of SA materials [48].

Apart from microfiber, a cell-type SA was demonstrated by filling the nanosheet solution into the micro-hole array of a single-mode photonic crystal fiber (PCF) [15][48][143][240]. The nanosheet can penetrate through the evanescent field of the fiber core and exhibits strong light-matter interaction. This method shows advantages in terms of better robustness than microfiber and controllable thickness of the deposited nanosheet [48]. However, this SA structure shows several limitations such as large splicing loss between PCF and single-mode fiber (SMF), high insertion loss from long PCF, and distortion in the guiding mode of the PCF [15]. These issues are addressed with short PCF of 90 μm to form the entire SA and dehydration of liquid column in PCF to compensate of the splicing loss between PCF and SMF. The comparison among the SA structures is summarized in Table 4. In short, fiber ferrule structure is recommended due to the simplest procedures and configuration, both D-shaped and tapered fiber structures are recommended for high power operation with evanescent field interaction, whereas PCF structure is recommended to address the fragility issue in tapered fiber.

Table 4: Advantages and disadvantages of SA structures.

SA structures	Advantages	Disadvantages
Fiber ferrule	1. Simple configuration. 2. Reflector-type SA improves MD.	1. Short interaction length. 2. Low thermal damage threshold. 3. Not suitable for high power application.

D-shaped fiber	1. Long nonlinear interaction length 2. High optical damage threshold. 3. Robust.	1. Polarization sensitive. 2. Induces evanescent optical loss.
Tapered fiber	1. Long nonlinear interaction length. 2. High optical damage threshold. 3. Larger area for evanescent interaction than D-shaped fiber.	1. Fragile. 2. Polarization sensitive. 3. Induces evanescent optical loss.
Cell-type PCF	1. Robust. 2. Controllable thickness of deposited nanosheet.	1. Large splicing loss between PCF and SMF. 2. Distortion in guiding mode of the PCF.

6.0 MLFL

MLFL is generated by integrating the SA inside a laser cavity. Three regimes are generated by controlling the group velocity dispersion (GVD) of the laser cavity, which are anomalous, normal, and zero dispersion. Kelly's sidebands are produced from the intra-cavity periodic perturbation when the laser cavity is operated in anomalous dispersion. The net anomalous dispersion generates soliton pulses by balancing the cavity dispersion and Kerr nonlinearity. Guo et al. [80] studied six types of dip-sideband patterns by manipulating the pump power and carefully adjusting the PC orientation. On the other hand, normal dispersion generates dissipative soliton with a rectangular pulse profile. In comparison to anomalous dispersion, normal dispersion generates a chirped pulse with larger pulse energies [241]. The compression of the chirped pulse can achieve an ultrashort pulse of fewer than 100 fs [242]. Nonetheless, a chirped pulse is difficult to be compressed outside the laser cavity due to the large nonlinear effect of dissipative soliton [243]. Therefore, the generation of anomalous dispersion is relatively simpler than normal dispersion regimes [244]. Dispersion-managed (DM) soliton has nearly zero dispersion with periodic compression, often called as stretched pulse, which has smooth Gaussian-shaped spectral profile. The DM soliton shows distinct advantages such as low noise, high pulse energy, and short pulse duration [243]. The pulses in DM regime experience periodic broadening and compression in each round trip to compensate larger nonlinear phase shift than soliton pulses thus leading to extremely short pulse duration [72]. Wang et al. [245] commented that DM pulses should be constructed with large normal and anomalous fiber to maintain the minimum pulse width within a small segment of the cavity while reducing the nonlinear optical effect. The dispersions in anomalous, normal and zero regimes were tailored by dispersion compensating fiber (DCF) to achieve larger normal dispersion, whereas lengthening of SMF helps to achieve larger anomalous dispersion within the laser cavity [94]. The optical spectrum of the ultrashort pulses with different dispersion regimes is presented in Fig. 9.

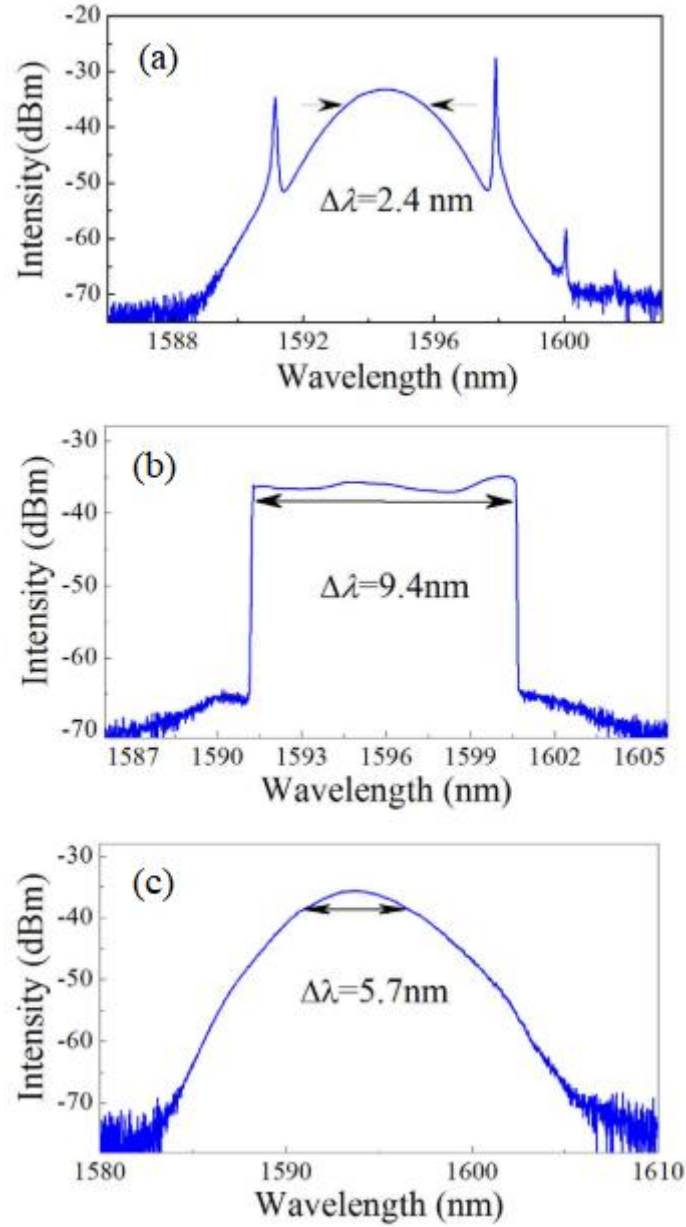


Fig. 9: Optical spectrum for MLFL in (a) anomalous dispersion, (b) normal dispersion, and (c) DM regimes.

A ring cavity laser is the most common configuration to generate MLFL in 1.0 μm [24][109], 1.52 to 1.62 μm [12][94], 1.9 to 2.0 μm [97][86], and 2.0 to 2.1 μm [14][88]. In 1.0 μm , the design of anomalous dispersion is challenging due to the limited source of optical fiber which can compensate for the normal dispersion of YDF. For instance, short YDF of 0.4 m and long SMF of 8.5 m were utilized to control the GVD to be close to zero [246]. From 1.52 to 1.62 μm , the optical attenuation is typically lower than other wavebands. This promises the erbium-doped MLFL in both telecommunication and long-haul applications [229]. From 1.9 to 2.0 μm region, sharp dips are generated due to the absorption of water and carbon dioxide molecules [247], which are spectrally matched to the simulated water lines in [47]. A re-compression mechanism was presented on a 1.9 μm soliton-pulses from 656 to 260

fs as well as producing high pulse energy of 1 nJ [248]. From 2.0 to 2.1 μm , the suitable active gain medium is holmium-doped fiber (HDF), which is pumped by 1.95 μm through ground state absorption. Significantly, wavelengths longer than 1.9 μm are feasible for eye-safe application [249]. Aside from these popular wavelengths, other wavelengths were demonstrated such as 1.2 μm MLFL using fluoride-based HDF [250], S-band MLFL using fluoride-based thulium-doped fiber [62], and 2.8 to 2.9 μm MLFL using Er:ZBLAN fiber [37][52]. To improve the conventional laser cavity which is polarization sensitive, Sobon et al. [91][112][251][252] presented polarization maintaining (PM) laser cavity which does not require the integration of polarization controller (PC). An investigation of modifying the dispersion from normal to anomalous for a PM-MLFL was demonstrated with a pulse duration ranging from 0.34 to 2.1 ps [253].

Apart from single wavelength MLFL, a tunable MLFL from 1025 to 1037 nm with modification in fiber cavity birefringence and pump powers [254], 1525 to 1559 nm with the integration of a wideband tunable filter [60], 1532 to 1555 nm with birefringence filtering effect [255], 1860 to 2060 nm with diffraction grating based mirror [121], as well as 1949.6 to 1972.0 nm and 1953.8 to 1976.2 nm by stretching the tapered fiber [256]. Additionally, the generation of switchable pulses between normal and DM regimes was presented in a 1.56 μm bidirectional laser setup [257]. This bidirectional setup was also presented with SWNT-SA which produces simultaneous mode-locked pulses at 1954.5 nm and 1951.6 nm at 35.15 MHz [258]. Next, dual-wavelength MLFL in the similar band was demonstrated in 1530 and 1545 nm with the adjustment of cavity chromatic dispersion [259], 1532 and 1555 nm with birefringence filtering effect [255], 1533 and 1558 nm by using polarization beam splitter [75], as well as 1956.8 and 1979.2 nm by adjustment of pump power and PC orientation [256]. In addition, the adjustment of pump power and PC in the laser cavity also generates simultaneous dissipative soliton and soliton pulses at 1923.6 nm and 1997.4 nm, respectively [260]. Moreover, a dual-band MLFL was achieved by sharing gain fiber, Tm^{3+} :ZBLAN fiber at the emission wavelength of 1480 nm and 1845 nm [132]. A recent 3 μm wavelength with 2865.2 nm centre wavelength [19] and from 2836.2 nm to 2906.2 nm [261] mode-locked Ho^{3+} -doped ZBLAN fiber laser was demonstrated with SWCNT-SA.

Harmonic mode-locking (HML) generates a pulse breaking mechanism from high-order nonlinear effect by high pump power or long-period interaction solitons [244]. This regime increases the pulse repetition rate of the MLFL with higher harmonics order. For instance, fundamental MLFL is generated at 338.9 mW with repetition rate of 7.8 MHz. The 21st order HML was generated at 517.4 mW pump power with repetition rate of 164.6 MHz [2]. In other word, the repetition rate at higher harmonics is the approximately the multiplication of the harmonic order (M integer) and the fundamental repetition rate. Fig. 10 illustrates that the pulse repetition rate is increased with higher pump power for HML. Nevertheless, a single pulse possesses higher pulse energy [115] and better spectral purity [69] than multiple pulses with a

higher repetition rate. A coexistence of fundamental and harmonic pulses is demonstrated in a dual-wavelength MLFL by adjusting the intra-cavity polarization state, with HML repetition rate from 0.324 to 1.138 GHz and fundamental repetition rate of 4.765 MHz [262]. The HML was also lately reported with the harmonics at 229th order from a fundamental repetition rate of 4.65 MHz to 1.1 GHz [110], and also the highest repetition rate up to 2.415 GHz at 213rd order harmonics [263]. A theoretical and experimental results showing the dynamics of HML generation and the interaction of acoustic mode in the SMF with the resonant frequency was modelled in [264].

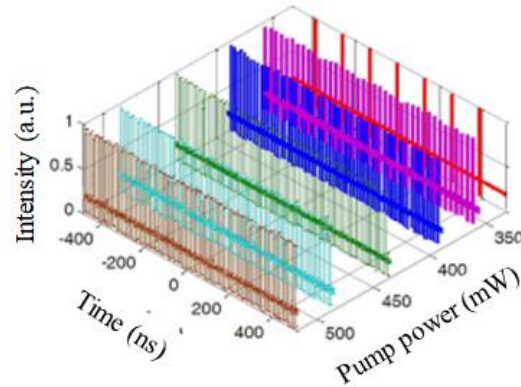


Fig. 10: Evolution of pulse train for the HML [2].

Time bandwidth product (TBP) is the lowest achievable of K value whereby any pulse cannot be lower than this value, which is expressed as

$$\Delta\tau.\Delta\nu \geq K, \quad (1)$$

where $\Delta\tau$ and $\Delta\nu$ are specified with FWHM value in the time domain, and frequency domain, respectively. The minimum K values for Gaussian, sech^2 , and Lorentzian pulses are 0.441, 0.315 and 0.221, respectively.

Table 5 summarizes the recent development of the MLFL from the year 2015 to 2020. Based on the summary, most SA materials are fabricated through ME, LPE, and CVD methods. In addition, the MLFL is primarily demonstrated with a ring cavity and anomalous dispersion. The TBP of the anomalous dispersion regime is typically closer to the K values than DM and normal dispersion regimes. Moreover, a DM soliton is recommended to design MLFL with shorter pulse duration.

Table 5: Summary of the overall performances for MLFL.

Year	Fabrication Method	Material	SA Structure	Deposition Technique	Laser cavity structure	Net cavity GVD	Wavelength (nm)	Bandwidth (nm)	Pulse duration (fs)	TBP	Repetition rate (MHz)	Ref.
2015	CVD	Monolayer graphene	D-shaped fiber	Film attachment	Ring	Anomalous	1879.4 nm	1.8 nm	4.7 ps	0.714	7.8 MHz	[2]
2015	CVD	Monolayer graphene	D-shaped fiber	Film attachment	Ring	Anomalous	1607.7 nm	8.6 nm	377 fs	-	37.72 MHz	[96]
2015	CVD	Graphene	1) Fiber ferrule 2) D-shaped fiber	Electron beam evaporation	Ring	Anomalous	1) 1571.96 nm 2) 1559 nm	1) 0.75 nm 2) 3.44 nm	1) 2.6 ns 2) 910 fs	1) – 2) 0.386	1) 15.06 MHz 2) 8.93 MHz	[234]
2015	CVD	15 layer graphene/PMMA	Fiber ferrule	Film attachment	Ring	Anomalous	1563 nm	4.5 nm	627 fs	0.346	14.3 MHz	[99]
2015	CVD	24 layer graphene/PMMA	Fiber ferrule	Film attachment	Ring	Anomalous	1876 nm	6.6 nm	603 fs	0.341	41.46 MHz	[91]
2015	CVD	12-48 layer graphene/PMMA	Fiber ferrule	Film attachment	Ring	Anomalous	1) 1557 – 1561.5 nm 2) 1910.8 – 1943.4 nm	1) 7.06 – 10.1 nm 2) 5.04 – 5.83 nm	1) 345 – 406 fs 2) 737 – 832 fs	1) 0.352 – 0.467 2) 0.317 – 0.348	1) ~ 54 MHz 2) ~ 28 MHz	[17]
2015	-	Graphene/DMF solution	Inner-air cavity optical fiber	Spin coating	Ring	Anomalous	~1558 nm	Small (CW components)	674 fs	-	8.655 MHz	[239]
2015	CVD	1) Transmission-type graphene 2) Reflection-type graphene	Fiber ferrule	Film attachment	Ring	Anomalous	1) 1572 nm 2) 1567 nm	1) 6.1 nm 2) 3.3 nm	1) 441 fs 2) 796 fs	1) ~ 0.33 2) ~ 0.32	1) 28.57 MHz 2) 16.66 MHz	[127]
2015	Vacuum filtration	GO paper	Fiber ferrule	Film attachment	Ring	Anomalous	1) 1564.4 nm 2) 1961.6 nm	1) 4.2 nm 2) 4 nm	1) 613 fs 2) 1.36 ps	1) 0.315 2) 0.424	1) 37.2 MHz 2) 27.37 MHz	[113]
2015	Hydrothermal method	MoS ₂ /graphene nanocomposite	Fiber ferrule	Drop casting	-	Anomalous	1571.8 nm	1.5 nm	2.2 ps	0.405	3.47 MHz	[157]
2015	LPE	MoS ₂ nanosheet	D-shaped fiber	Optical deposition	Ring	Anomalous	1530.4 nm	2.1 nm	1.21 ps	0.33	8.968 MHz	[265]
2015	Li chemical intercalation	MoS ₂ solution	D-shaped fiber	Spin coating	Ring	1) Anomalous 2) Normal	1) 1584 nm 2) 1570 nm	1) 9.96 nm 2) 18.2 nm	1) 521 fs 2) 11.9 ps	-	1) 25.21 MHz 2) 26.02 MHz	[54]
2015	LPE	MoS ₂ /PVA	Fiber ferrule	Film	Linear	DM	1556.3 nm	6.1 nm	935 fs	-	463 MHz	[69]

			reflector	attachment								
2015	LPE	1) WS ₂ 2) WS ₂ /PVA	1) D-shaped fiber 2) Fiber ferrule	1) Optical deposition 2) Film attachment	Ring	Anomalous	1) 1557 nm 2) ~1558 nm	1) 2.3 nm 2) 3.1 nm	1) 1.32 ps 2) 1.20 ps	1) 0.38 2) 0.34	1) 8.86 MHz 2) 8.96 MHz	[68]
2015	LPE	WS ₂ /PVA	Fiber ferrule	Film attachment	Ring	Anomalous	1572 nm	5.2 nm	595 fs	-	25.23 MHz	[50]
2015	1) Li chemical Intercalation 2) CVD	WS ₂	D-shaped fiber	1) spin coating 2) Film attachment	Ring	Anomalous	1) 1566 nm 2) 1565 nm	1) 5.6 nm 2) 8.23 nm	1) 467 fs 2) 332 fs	-	1) 21.07 MHz 2) 31.11 MHz	[53]
2015	-	WS ₂	D-shaped fiber	PLD	Ring	Anomalous	1) 1558.5 nm 2) 1559.7 nm	1) – (cw competing peak) 2) 6.6 nm	1) 675 fs 2) 452 fs	1) – 2) 0.367	1) 19.58 MHz 2) 1.04 GHz (53 th harmonics)	[237]
2015	-	Commercially available WS ₂ solution	PCF	Core filling	Ring	Anomalous	1563.8 nm	5.19 nm	524 fs	0.333	19.57 MHz	[143]
2015	LPE	MoSe ₂ /PVA	Fiber ferrule	Film attachment	Ring	Anomalous	1558.25 nm	1.76 nm	1.45 ps	0.316	8.028 MHz	[67]
2015	ME	BP	Fiber ferrule	Scotch tape exfoliation	Ring	Anomalous	1571.45 nm	2.925 nm	946 fs	0.328	5.96 MHz	[25]
2015	Direct heating	BP	Fiber ferrule	Film attachment	Ring	Anomalous	1558.7 nm	6.2 nm	786 fs	0.6	14.7 MHz	[189]
2015	LPE	Few-layer BP	Microfiber	Drop casting	Ring	Anomalous	1566.5 nm	3.39 nm	940 fs	0.38	4.96 MHz	[77]
2015	ME	Phosphorene	Fiber ferrule	Scotch tape transfer	Ring	Anomalous	1910 nm	5.8 nm	739 fs	0.352	36.8 MHz	[47]
2015	Seed-mediated growth	GNRs/PVA	Fiber ferrule	Film attachment	Ring	Anomalous	1559.8 nm	6.93 nm	379 fs	0.324	8.93 MHz	[215]
2015	Seed-mediated growth	GNRs/NaCMC	Fiber ferrule	Film attachment	Ring	1) Normal 2) Anomalous	1) 1039 nm 2) 1560 nm	1) 0.9 nm 2) 1.5 nm	1) 460 ps 2) 2.91 ps	1) 119.6 2) 0.523	1) 43.5 MHz 2) 35.6 MHz	[214]
2015	CVD	SiC	Fiber ferrule	Film attachment	Ring	Anomalous	1570 nm	5.13 nm	470 fs	0.319	29.89 MHz	[220]
2015	-	Ethanol	Fiber ferrule	Sealed with PE film	Ring	Anomalous	1594.6 nm	3.33 nm	972 fs	0.38	20.97 MHz	[151]
2016	LPE	SWCNT solution	PCF	Siphon	Ring	Anomalous	1566.36 nm	5.16 nm	1.003 ps	0.633	9.1 MHz	[15]
2016	CVD	SWCNT film	Fiber ferrule	Dry transfer	Ring	Anomalous	1560.2 nm	1.5 nm	1.7 ps	-	50.3 MHz	[98]

2016	Arc-discharge	CNT/CMC composite	Fiber ferrule	Film attachment	Ring	Normal	1927 nm	52.83 nm	152 fs	0.66	25.76 MHz	[122]
2016	Arc-discharge	CNT/CMC composite	Fiber ferrule	Film attachment	Ring	1) Anomalous 2) DM 3) Normal	~1950 nm	1) 4.0 nm 2) 7.5 nm 3) 6.2 nm	1) 1.0 ps 2) 0.85 ps 3) 0.95 ps	1) 0.31 2) 0.49 3) 0.64	12.6 MHz	[243]
2016	Vertical evaporation	1) 3 layer SWCNT 2) 4 layer GO	Fiber ferrule	Film attachment	Ring	Anomalous	1) 1557 nm 2) 1558 nm	1) 4.53 nm 2) 2.9 nm	1) 827.8 fs 2) 953.8 fs	-	-	[126]
2016	CVD	Monolayer graphene	D-shaped fiber	Film attachment	Ring	Anomalous	1910 nm	5.14 nm	773 fs	0.33	19.31 MHz	[90]
2016	CVD + thermal evaporation	Monolayer graphene	D-shaped fiber	Graphene layer transfer	Ring	Normal	~ 1570 nm	51 nm	120 fs	-	7.238 MHz	[95]
2016	CVD	Monolayer Graphene	D-shaped fiber	Film attachment	Ring	Anomalous	1557 nm	10.47 nm	256 fs	0.331	12.29 MHz	[227]
2016	-	Graphene	Fiber ferrule	-	Linear	Anomalous	1) 1480 nm 2) 1845 nm	1) 4.48 nm 2) 3.54 nm	1) 610 fs 2) 1.68 ps	1) 0.37 2) 0.52	12.3 MHz	[132]
2016	CVD	Graphene	Clad-microfiber	Film wrapping	Ring	Anomalous	1533.82 nm	2.08 nm	1.21 ps	0.322	1.89 MHz	[89]
2016	CVD	9 layer graphene/PMMA composite	Fiber ferrule	Film attachment	Ring	Anomalous	2078.4	7.0 nm	811 fs	0.326	34 MHz	[88]
2016	-	GO solution	Tapered fiber	Drop casting	Ring	Anomalous	1556.5 nm	8.5 nm	615 fs	0.64	17.09 MHz	[228]
2016	Hydrothermal	Graphitic carbon nitride solution	Fiber ferrule mirror	Drop casting	Ring	Normal	1070 nm	0.9 nm	420 ps	Chirped	7.65 MHz	[109]
2016	LPE	Graphene/SMMA composite	Fiber ferrule	Film attachment	Ring	Anomalous	1557 nm	9.78 nm	326 fs	0.33	-	[55]
2016	LPE	Graphene/BPQD solution	D-shaped fiber	Immersion	Ring	Anomalous	1531 nm	19.4 nm	148 fs	0.37	7.5 MHz	[66]
2016	CVD	MoS ₂	Clad-microfiber	Film wrapping	Ring	1) Normal 2) DM 3) Normal	1) 1596 nm 2) 1594 nm 3) 1595 nm	1) 9.4 nm 2) 5.7 nm 3) 2.4 nm	1) 121 ps 2) 1.65 ps 3) 2.5 ps	1) 134 2) 1.1 3) 0.7	1) 3.63 MHz 2) 1.61 MHz 3) 1.315 MHz	[94]
2016	Bath sonication	MoSe ₂ /PVA composite	D-shaped fiber	Deposition	Ring	Anomalous	1557.3 nm	5.1 nm	751 fs	0.473	3.27 GHz (212 th harmonics)	[11]
2016	LPE	1) WSe ₂ 2) MoSe ₂ 3) WSe ₂ /PVA 4) MoSe ₂ /PVA	1,2) D-shaped fiber 3,4) Fiber ferrule	1,2) Optical deposition 3,4) Film attachment	Ring	Anomalous	1) 1556.7 nm 2) ~1557.5 nm 3) ~1558 nm 4) ~ 1561 nm	1) 2 nm 2) 2.3 nm 3) - 4) -	1) 1.31 ps 2) 1.09 ps 3) 1.25 ps 4) -	1) - 2) 0.316 3) - 4) -	1, 3) 5.31 MHz 2, 4) 5.03 MHz	[44]

2016	LPE	TiS ₂	Tapered fiber	Optical deposition	Ring	Anomalous	1563.3 nm	4.75 nm	1.25 ps	0.469	22.7 MHz	[65]
2016	LPE	BP nanoflakes	Fiber ferrule	Deposition	Ring	Anomalous	1559.5 nm	3.8 nm	670 fs	0.32	8.77 MHz	[76]
2016	LPE	BP	Tapered fiber	Optical deposition	Ring	Anomalous	1569.24 nm	9.35 nm	280 fs	0.32	60.5 MHz	[16]
2016	LPE	OBP	Tapered fiber	Optical deposition	Ring	Anomalous	1571.5 nm	4.15 nm	727 fs	0.366	11 MHz	[64]
2016	Hydrothermal	Phosphorene/PVdF composite	Fiber ferrule	Film attachment	Ring	Anomalous	1567.5 nm	2.4 nm	1.08 ps	0.316	15.25 MHz	[56]
2017	Arc-discharge	Commercial SWCNT	Fiber ferrule	Film attachment	Linear	Anomalous	1) 1860 nm 2) 2010 nm	~ 3 nm	1) 2.38 ps 2) 2.83 ps	0.567	18.4 MHz	[121]
2017	Vacuum filtration + bath sonication	CNT	Fiber ferrule	Film attachment	Ring	Anomalous	1928 nm	8.5 nm	501 fs	0.343	56.368 MHz	[112]
2017	CVD	DWCNT-PVA	Fiber ferrule	Film attachment	Ring	Anomalous	1880 nm	6.3 nm	560 fs	-	-	[97]
2017	LPE	1.0 nm diameter CNT/polymer composite	Fiber ferrule	-	Ring	Anomalous	1557 nm	7.5 nm	560 fs	-	45 MHz	[63]
2017	CVD	Graphene/PMMA composite	Fiber ferrule	Film attachment	Ring	DM	1945 nm	27.5 nm	205 fs	-	58.87 MHz	[251]
2017	CVD	37 layers graphene/PMMA	Fiber ferrule	Film attachment	Ring	Anomalous	1563.3 nm	20.2 nm	148 fs	0.365	101.32 MHz	[252]
2017	LPE	Nitrogen-doped graphene sheets	Fiber ferrule	Film attachment	Ring	Anomalous	1506 nm	0.76 nm	4.4 ps	0.44	6.85 MHz	[62]
2017	ME	MoS ₂ flakes	D-shaped fiber	Adhesive tape transfer	Ring	Anomalous	1560 nm	20.5 nm	200 fs	0.505	14.53 MHz	[227]
2017	LPE	MoSe ₂ /PVA composite	D-shaped fiber	Drop casting	Ring	Anomalous	1912.6 nm	4.62 nm	920 fs	0.348	18.21 MHz	[225]
2017	LPE	WS ₂ nanosheet solution	D-shaped fiber	Immersion	Ring	Anomalous	(a) 1557 nm (b) 1563.7 nm	(a) 4 nm (b) 3.9 nm	(a) 660 fs (b) 710 fs	(a) 0.327 (b) 0.34	(a) 10.2 MHz b) 460.7 MHz (45 th harmonics)	[235]
2017	CVD	WSe ₂	Tapered fiber	Film attachment	Ring	Anomalous	1) 1556.42 nm 2) 1886.22 nm	1) 6.06 nm 2) 3.29 nm	1) 477 fs 2) 1.18 ps	-	1) 14.02 MHz 2) 11.36 MHz	[85]
2017	CVD	MoTe ₃	Tapered fiber	MSD	Ring	Anomalous	1915.5 nm	3.13 nm	1.25 ps	0.32	18.72 MHz	[116]

2017	CVD	ReS ₂	D-shaped fiber	Wet chemical transfer	Ring	Anomalous	1564 nm	2.6 nm	1.25 ps	0.4	3.43 MHz	[93]
2017	LPE	SnS ₂ /PVA	Fiber ferrule	Film attachment	Ring	Normal	1062.66 nm	8.63 nm	656 ps	1504	39.33 MHz	[78]
2017	CCM	PbSe ₂ /UV gel	Fiber ferrule	Mixture transfer	Ring	Normal	1068 nm	4.5 nm	70 ps	-	8.3 MHz	[105]
2017	MSD	WS ₂ -MoS ₂ -WS ₂ hetero-structure	Fiber end facet	Vertically grown	Ring	Anomalous	1562.66 nm	16.03 nm	296 fs	-	36.46 MHz	[101]
2017	LPE	BP dispersed in NMP solution	Fiber ferrule	Solution deposition	Ring	Anomalous	2094 nm	4.2 nm	1.6 ps	-	1) 29.1 MHz 2) 290 MHz (10 th harmonics)	[74]
2017	LPE	BP nanosheet	Fiber ferrule	Deposition	Ring	Anomalous	1) 1533 nm, 1558 nm 2) 1558 nm	1) 3.7 nm, 6.9 nm 2) 7.1 nm	1) – 2) 700 fs	1) – 2) 0.6	1) ~20.82 MHz 2) 20.82 MHz	[75]
2017	LPE	Phosphorene	Tapered fiber	Optical deposition	Ring	Anomalous	1561.7 nm	3 nm	882 fs	0.325	5.47 MHz	[49]
2017	LPE	Antimonene	Tapered fiber	Optical deposition	Ring	Anomalous	1557.68 nm	4.84 nm	552 fs	0.33	10.27 MHz	[61]
2017	Vacuum filtration	1) DNA 2) DNA-CTMA	D-shaped fiber	1) Optical adhesion 2) Film attachment	Ring	Anomalous	1) 1567 nm 2) 1562 nm	1) 6.66 nm 2) 8.80 nm	1) 417 fs 2) 323 fs	-	1) 29.29 MHz 2) 28.73 MHz	[223]
2018	LPE	SWCNT-CMC polymer composite	Fiber ferrule	Film attachment	Ring	Anomalous	1525 nm to 1559 nm	6 nm to 1.2 nm	545 fs to 6.1 ps	0.408	17.4 MHz	[60]
2018	LPE	SWCNT/PVA-SDBS matrix composite	Fiber ferrule	Film attachment	Ring	-	~1560 nm	-	550 fs	-	18.5 MHz	[59]
2018	Hydrothermal method	CNT	AFI	Fabrication of aligned CNT in AFI nanochannels	Ring	Anomalous	1563.1 nm	1) 5.51 nm	1) 386 fs	-	23.2 MHz	[266]
2018	LPE	CNT/PVA	Fiber ferrule	Film attachment	Ring	Anomalous	1192 nm	0.48 nm	4.3 ps	0.4358	18.47 MHz	[250]
2018	Electric arc discharge	SWCNT/PVA	Fiber ferrule	Film attachment	Ring	DM	1031.5 nm	20.2 nm	175 fs	38.62 (Before dechirp)	21.2 MHz	[246]
2018	Carbon/silica	MCNs/NaCMC	1) Fiber	1) Film	Ring	1) Normal	1) 1036 nm	1) -	1) 445 ps	1)	1) 46.27	[231]

	carbonization	composite	Ferrule 2) Tapered fiber	attachment 2) Film deposition		2) Anomalous	2) 1953 nm	2) -	2) 1.54 ps	Chirped 2) -	MHz 2) 26.3 MHz	
2018	-	Graphene/PMMA	Fiber ferrule	Film attachment	Ring	DM	2060 nm	53.6 nm	190 fs	0.72	20.98 MHz	[14]
2018	CVD	Graphene/PMMA	Fiber ferrule	Film attachment	Ring	Anomalous	1) 1533.4 nm 2) 1556.11 nm	1) 2.75 nm 2) 3.14 nm	1) 900 fs 2) 940 fs	1) 0.32 2) 0.37	1) 8.4 MHz 2) 9.1 MHz	[267]
2018	ME	graphite/PMMA	D-shaped fiber	Film attachment	Ring	DM	1567 nm	21 nm	220 fs	0.564	15.7 MHz	[36]
2018	Modified Hummer's method	1) GO 2) rGO	D-shaped fiber	Wet transfer	Ring	Anomalous	1566 nm	1) 27.2 nm 2) 24.1 nm	190 fs	1.00	15.73 MHz	[103]
2018	ME	MoTe ₂	Tapered fiber	Film deposition	Ring	Anomalous	1) 1559.57 nm 2) 1934.85 nm	1) 11.76 nm 2) 3.2 nm	1) 229 fs 2) 1.3 ps	1) 0.332 2) 0.333	1) 26.6 MHz 2) 15.37 MHz	[42]
2018	CCM	TiS ₂ nanosheet	Fiber ferrule	Optical deposition	Ring	Anomalous	1569.5 nm	2.63 nm	1.04 ps	0.34	5.34 MHz	[106]
2018	LPE	HfS ₂ nanosheet	Tapered fiber	PCF-assisted deposition	Ring	Anomalous	1561.8 nm	12.2 nm	221.7 fs	0.331	21.45 MHz	[48]
2018	LPE	SnS ₂ /PVA	Fiber ferrule	Film attachment	Ring	Anomalous	1562.01 nm	6.09 nm	623 fs	0.466	29.33 MHz	[58]
2018	CVD	PtSe ₂	Tapered fiber	Film attachment	Ring	Anomalous	1563 nm	6 nm	1.02 ps	-	23.3 MHz	[92]
2018	CVD	Monolayer WSe ₂	Tapered fiber	Film attachment	Ring	Anomalous	1863.96 nm	3.19 nm	1.16 ps	0.32	11.36 MHz	[87]
2018	CVD	MoTe ₂	Tapered fiber	Film Attachment	Ring	Anomalous	1930.22 nm	4.45 nm	879 fs	0.315	14.353 MHz	[86]
2018	LPE	ReS ₂ /PVA	Fiber ferrule	Film attachment	Ring	Anomalous	~1557 nm	1.85 nm	1.6 ps	-	5.48 MHz	[70]
2018	LPE	MoO ₃ /PVA composite	Fiber ferrule	Film attachment	Ring	Normal	1067 nm	0.242 nm	130 ps	7.8	17 MHz	[142]
2018	LPE + vacuum filtration	ReS ₂ -ReS ₂ /PDMS	Tapered fiber	Sandwich adhesion	Ring	Anomalous	1563.3 nm	8.2 nm	3.8 ps	-	1.78 MHz	[51]
2018	LPE	InSe/PVA	Fiber ferrule	Film attachment	Ring	Normal	1068.36 nm	1.72 nm	1.37 ns	61.9	1.76 MHz	[79]
2018	ME	BP flakes	Sandwich structure between FGF and PDMFF	Adhesion	Forward pumping	-	2771.1 nm	4.9 nm	10 ps (estimation)	-	27.4 MHz	[37]

2018	LPE	BP flakes	Fiber ferrule	Inkjet printing	Ring	DM	1555 nm	40 nm	102 fs	0.51	23.9 MHz	[72]
2018	Hydrothermal method	Bismuthene	Tapered fiber	Optical deposition	Ring	Anomalous	1559.18 nm	4.64 nm	652 fs	-	8.83 MHz	[57]
2018	LPE	Bismuthene nanosheet	Tapered fiber	Film attachment	Ring	Anomalous	1561 nm	14.4 nm	193 fs	0.342	8.85 MHz	[71]
2018	Hot injection method	Colloidal PbS QD	Fiber ferrule	Drop casting	Ring	Anomalous	1563 nm	4.78 nm	559 fs	0.33	13.9 MHz	[111]
2018	-	PbS/CdS-QD	Fiber ferrule	Film attachment	Ring	Anomalous	1562.5 nm	2.504 nm	54 ps	16.63	3.302 MHz	[209]
2018	Seed-mediated growth	GNRs	D-shaped fiber	Film attachment	Ring	Normal	1041 nm	8.6 nm	162.3 ps	386.4	6.649 MHz	[212]
2018	Seed-mediated growth	GNRs solution	Tapered fiber	Immersion	Ring	Anomalous	1943.5 nm	10.8 nm	404 fs	0.357	25.66 MHz	[213]
2018	Hydrothermal method	Ni-MOF/IPA solution	D-shaped fiber	Drop casting	Ring	1) Normal 2) Anomalous	1) 1062.02 nm 2) 1563.79 nm	1) 2.23 nm 2) 3.8 nm	1) 240 ps 2) 749 fs	1) 142.4 2) 0.35	1) 9.57 MHz 2) 6.47 MHz	[107]
2019	LPE	CNT-PVA film	Fiber ferrule	Film attachment	Ring	Anomalous	1594.97 nm	10.19 nm	742 fs	0.89	2.415 GHz (213 rd order)	[263]
2019	LPE	SWCNT	Fiber ferrule	Film attachment	Ring	Anomalous	2080 nm	6.65 nm	212 fs	0.315	54.43 MHz	[268]
2019	Modified Hummer's method	Graphene solution	Fiber ferrule	Optical deposition	Ring	Anomalous	1) 1558 nm 2) 1558 nm	1) 3.1 nm 2) 3.4 nm	1) 950 fs 2) 840 fs	1) 0.354 2) 0.343	1) 15.75 MHz 2) 409.6 MHz (26 th harmonics)	[102]
2019	-	Glycerin	Fiber ferrule	Coating	Ring	Anomalous	1568.92 nm	1.15 nm	3.57 os	1.51	23.08 MHz	[150]
2019	Liquid interfacial synthesis	Graphdiyne	Fiber ferrule	Film transfer	Ring	Anomalous	1557.17 nm	4.07 nm	688 fs	0.346	14.6 MHz	[269]
2019	CVD	MoS ₂ /PVA	Fiber ferrule	Film transfer	Ring	Normal	1564.586 nm	10.596 nm	10.84 ns	-	940.8 kHz	[270]
2019	LPE	MoS ₂	Fiber ferrule	Film transfer	Ring	Anomalous	1570 nm	7.49 nm	386 fs	0.315	28 MHz	[19]
2019	LPE	MoS ₂	Sol-gel	Sol-gel transfer	Ring	Normal	1029.78 nm	14.98 nm	13.8 ps	58.46	22.44 MHz	[271]
2019	MSD	MoTe ₂	Tapered fiber	Optical deposition	Ring	Anomalous	1561 nm	24.9 nm	111.9 fs	-	96.15 MHz	[21]
2019	LPE	ReSe ₂ /PVA	D-shaped fiber	Drop casting	Ring	Anomalous	1561.2 nm	3.4 nm	862 fs	0.361	14.97 MHz	[272]
2019	ME	Bulk PtSe ₂	D-shaped fiber	Scotch tape transferring	Ring	Anomalous	1567.07 nm	3.105 nm	861 fs	0.326	8.24 MHz	[174]
2019	-	In ₂ Se ₃ /PVA	Fiber ferrule	Film	Ring	Anomalous	1) 1558 nm	1) 1.5 nm	1) 1.88 ps	1) 0.347	1) 1.85 MHz	[183]

				attachment			2) 1530 nm	2) 1.6 nm	2) 1.76 ps	2) 0.36	2) 1.85 MHz	
2019	LPE	SnSe ₂ /PVA	Fiber ferrule	Film attachment	Ring	Normal	1064 nm	1.9 nm	278.8 ns	-	333 kHz	[226]
2019	Mechanical grinding and sonication	SnSe ₂ /polyvinylpyrrolidone (PVP)	D-shaped fiber	Drop casting	Ring	Anomalous	1560 nm	5.27 nm	610 fs	-	15.5 MHz	[180]
2019	LPE	Antimonene	Fiber ferrule	Dip coating and drying	Ring	Anomalous	1564 nm	0.278 nm	953 ns	32.49	356 MHz (165 th harmonics)	[81]
2019	LPE	PbS nanoparticles	Fiber ferrule	Film attachment	Ring	Anomalous	1957.37 nm	3.43 nm	1.91 ps	0.335	21.93 MHz	[273]
2019	Bacterially harvesting	Bio-tellurium/PMMA	Fiber ferrule	Film transfer	Ring	Anomalous	1550 nm	-	1.81 ps	-	18.8 MHz	[274]
2020	CVD	Graphene/WS ₂	Fiber ferrule	Film transfer	Ring	Anomalous	1601.9 nm	4.3 nm	660 fs	0.33	21.78 MHz	[185]
2020	LPE	WS ₂	Fiber ferrule	Sol-gel transfer	Ring	1) Normal 2) Anomalous	1) 1029.1 nm 2) 1560.1 nm	1) 3.2 nm 2) 9.1 nm	1) 58 ps 2) 325 fs	1) – 2) 0.365	1) 19.03 MHz 2) 30.91 MHz	[275]
2020	LPE	PdS ₂ /PVA	D-shaped fiber	Film transfer	Ring	Anomalous	1565.8 nm	4.48 nm	803 fs	0.44	12.1 MHz	[84]
2020	Magnetic fluid	Fe ₃ O ₄	Fiber ferrule	Drop casting	Ring	Anomalous	1572.39 nm	1.39 nm	2.93 ps	0.494	2.806 MHz	[187]
2020	Chemical Vapour transport	TiS ₃	Fiber ferrule	Chemical vapour transport	Ring	Anomalous	1555.34 nm	30.49 nm	147.72 fs	0.5582	76.168 MHz	[81]
2020	Hydrothermal	Ag ₂ S	Tapered fiber	Optical deposition	Ring	Anomalous	1561.1 nm	1.54 nm	780 fs	-	1) 4.65 MHz 2) 1.1 GHz (229 th harmonics)	[110]
2020	LPE	Bismuthene	Tapered fiber	Drop casting	Ring	Anomalous	1555.7 nm	1.12 nm	1.3 ps	-	4 MHz	[276]
2020	LPE	Tellurene/PVA	Fiber ferrule	Film attachment	Ring	Anomalous	1565.58 nm	0.12 nm	21.45 ps	0.315	5.0378 MHz	[83]
2020	LPE	Tellurene	Tapered fiber	Supernatant deposition	Ring	Anomalous	1558.8 nm	2.91 nm	1.03 ps	0.37	3.327 MHz	[82]

7.0 Applications

The MLFL has been employed for arrays of applications. The direct application of MLFL is the generation of supercontinuum (SC) laser through a nonlinear medium. For instance, a thulium-doped MLFL was integrated to generate a mid-infrared SC laser source from 900 to 9000 nm with highly nonlinear optical fiber [277]. Apart from SC laser, thulium-doped mode-locked laser serves as the pump source for the optical parametric oscillator in the mid-infrared range from 3.0 to 5.4 μm [278]. The optical parametric oscillator is applied in a frequency comb spectroscopy system for the detection of atmospheric air compounds such as CH_4 , CO , CO_2 and H_2O . A dual-band wavelength MLFL is applied in time-resolved and multi-wavelength cavity ring-down spectroscopies, as well as the design of transmitters which operate at two separate operating wavelengths [279]. Based on the dual-band wavelength MLFL in [132], the 1480 nm wavelength is useful for water detection in various liquids, whereas 1845 nm is suitable for laser treatment and surgery for the human retina. In addition, mode-locked laser was employed to write waveguide on glasses [8]. The laser beam is focused with a microscope objective to induce defects based on multiphoton interaction to numerous kinds of glasses such as silica, borate, soda lime silicate and ZBLAN. The writing of damage lines or waveguides perpendicular to the incident laser beam provides flexibility to write multiple planar patterns by changing the focus depth of the laser beam. An advantage of this technique is that the glasses do not cracked throughout the writing process regardless of laser powers. In addition, mode-locked laser was applied in the synchronization of lasers and microwave sources [7]. The ultra-low noise signal from the mode-locked laser was employed as the timing signals, which were distributed along 300 m timing-stabilized fiber links to synchronize the receive signals. The proposed technique provides a precision of 6.4 fs residual timing error and 0.36 fs timing jitter over 72 hours of unaided operation. A coherent radar demonstrator was presented with the mode-locked laser to generate radar signals and receive the echoes [9]. This remote sensing system shows high accuracy and effectiveness, which is free from up and down-conversion of the radio frequency signal to achieve high signal resolution. The system shows an improvement to the current electronics technology with carrier frequency above 2 GHz, as well as the capability in detecting non-cooperating airplanes. Subsequently, these applications promote the large marketable values of mode-locked laser in both research institutes and industry sectors.

8.0 Conclusion

In conclusion, a comprehensive review has been successfully presented on material-based SA in the recent development of MLFL. SA is the mode-locker which can be synthesized with numerous methods. ME, LPE and CVD are among the most popular material synthesis techniques. The ME and LPE are cost-effective solutions, whereas CVD provides high product quality. In addition, modified Hummer's method, CCM, electrochemical exfoliation, hydrothermal, hot injection, and other methods show the potential as the alternatives for ME, LPE or CVD in synthesizing the SA materials.

Next, the characteristics and feasibility of the materials as the SA are concluded. The SA materials have been developed from SWCNT, graphene, TMD to lately BP. In contrast to SWCNT, graphene shows the advantage of zero bandgap for broadband wavelength operation. Both SWCNT and graphene possess the advantages of high nonlinearity and ultrafast recovery time. However, the operating wavelength of SWCNT is limited to tube diameter and chirality control whilst graphene has a weak absorption coefficient of less than 2.3 % per layer. Moreover, the TMD is attractive for the thickness dependent bandgap and electronic band structure. Nevertheless, a challenge in TMD is the robustness and stability issue when exposed to high power illumination. In comparison to TMD, BP has tunable direct bandgap for all thicknesses. Additionally, BP possesses a higher absorption coefficient per layer than graphene. However, BP is vulnerable to photo-oxidation and water absorption. To alternatively substitute these materials, TMO, QDs, GNRs, MOF and other materials are progressively proposed. TMO has been proven with its high nonlinear optical absorption, large third-order optical nonlinearity, and ultrafast response time. QDs have zero-dimensional, scalable bandgap, and stronger third order nonlinearity than bulk material. Most QDs, such as phosphorene, antimonene, bismuthene, and tellurene show these remarkable properties as the saturable absorber. However, the large bandgap for certain QDs circumvent its application for broadband operation. For GNR, the engineering of its aspect ratio contributes to the broadband operation. Nonetheless, the photo-thermal effect with high peak power will optically damage the GNRs and limits the pulse duration to a maximum of up to tens of picoseconds. In short, the TMO, QDs, GNRs, MOF, and other materials have been demonstrated with remarkable properties as the saturable absorber. Nevertheless, the research for these materials in longer wavelength regions such as 1.55 μm and 2 μm remains at quite an early investigation stage. The authors believe further studies and research of these materials in numerous wavelength region such as visible, NIR, MIR, and THz will satisfy large research gaps throughout this research pathway. The materials are mainly deposited to fiber ferrule, D-shaped fiber, and tapered fiber to produce the SA. The fiber ferrule SA shows the simplest configuration at the cost of a low optical damage threshold. D-shaped and tapered fiber SAs possess the evanescent field interaction with the material, along with longer nonlinear interaction length and higher optical damage threshold than fiber ferrule SA. Nevertheless, tapered fiber is mechanically fragile whereas D-shaped fiber is sensitive to polarization. The SA is incorporated inside the laser cavity to generate MLFL. A laser cavity is designed in an anomalous dispersion regime with Kelly's sidebands indicating stable soliton pulses, normal dispersion regime with large chirped dissipative soliton pulses for high pulse energy application especially in 1.06 μm , and DM regime to generate pulse duration typically shorter than 200 fs with Gaussian profile. Based on the recent development of MLFL in Table 5, the ring cavity and anomalous dispersion are primarily employed due to the design simplicity in the laser cavity. The ultrashort pulses ranging from ps to fs are potential in several applications such as the generation of SC laser, waveguide writing on glasses, and coherent radar system. These applications show the marketable potential of MLFL. In the authors' perspective view, the technology for

the preparation of the SA and the generation of passively mode-locked fiber laser is in the mature stage. Some recent research focuses on discovering new SA materials or performing the mode-locked laser in different wavelength region, particularly in 1 μm , 1.55 μm and 2 μm . This could be a minor improvement to this research area as there is insignificant improvement to the mode-locked laser performance and the SA material characteristics. Therefore, a more valuable work in this research area could be paved into several directions, such as the investigation of mode-locked laser in achieving higher peak power, higher harmonics, and shorter pulse duration even with attosecond. The study of the dynamics for soliton, harmonic mode-locking, stretch pulse and others are very interesting even with some old SA materials such as CNT or graphene. Moreover, the research will be more valuable by aligning the experimental measurement to the theoretical modelling and simulation. The SA has a bright future trend as there is still existing research gap to be fulfilled such as the extensive studies for integration and interaction of the material to the laser, material properties and characteristics as the SA, and optimization of the SA quality in terms of modulation depth, saturation intensity, and non-saturable loss. In a nutshell, this review provides better insight for the readers to select the most appropriate material synthesis technique, material or material/polymer composite, SA structure, deposition techniques, as well as structural and dispersion design of MLFL cavity based on the recommendations in each of the discussed sections.

References

- [1] J. Kim and Y. Song, "Ultralow-noise mode-locked fiber lasers and frequency combs : principles, status, and applications," *Adv. Opt. Photonics*, vol. 8, no. 3, pp. 465–540, 2016.
- [2] X. Li, X. Yu, Z. Sun, Z. Yan, B. Sun, Y. Cheng, and X. Yu, "High-power graphene mode-locked Tm/Ho co-doped fiber laser with evanescent field interaction," *Sci. Rep.*, vol. 5, p. 16624, 2015.
- [3] M. Zhang, Q. Wu, F. Zhang, L. Chen, X. Jin, and Y. Hu, "2D Black Phosphorus Saturable Absorbers for Ultrafast Photonics," *Adv. Opt. Mater.*, vol. 1800224, pp. 1–18, 2018.
- [4] M. Azimipour and R. Pashaie, "Nonlinear optical signal processing on multiwavelength sensitive materials," *Opt. Lett.*, vol. 38, no. 21, pp. 4324–4326, 2013.
- [5] D. Huang, E. A. Swanson, C. P. Lin, J. S. Schuman, W. G. Stinson, W. Chang, M. R. Hee, T. Flotire, K. Gregory, C. A. Puliafito, and J. G. Fujimoto, "Optical Coherence Tomography," *Science (80-.)*, vol. 254, no. 5035, pp. 1178–1181, 1991.
- [6] M. E. Fermann, T. R. Schibli, I. Hartl, D. C. Yost, M. J. Martin, A. Marcinkevics, and J. Ye, "Optical frequency comb with submillihertz linewidth and more than 10 W average power," *Nat. Photonics*, vol. 2, pp. 355–359, 2008.
- [7] J. Kim, J. A. Cox, J. Chen, and F. X. Kärtner, "Drift-free femtosecond timing

- synchronization of remote optical and microwave sources,” *Nat. Photonics*, vol. 2, pp. 733–736, 2008.
- [8] K. M. Davis, K. Miura, N. Sugimoto, and K. Hirao, “Writing waveguides in glass with a femtosecond laser,” *Opt. Lett.*, vol. 21, no. 21, pp. 1729–1731, 1996.
 - [9] P. Ghelfi, F. Laghezza, F. Scotti, G. Serafino, A. Capria, S. Pinna, D. Onori, C. Porzi, M. Scaffardi, A. Malacarne, V. Vercesi, E. Lazzeri, F. Berizzi, and A. Bogoni, “A fully photonics-based coherent radar system,” *Nature*, vol. 507, pp. 341–345, 2014.
 - [10] A. Stolow, A. E. Bragg, and D. M. Neumark, “Femtosecond Time-Resolved Photoelectron Spectroscopy,” *Chem. Rev.*, vol. 104, pp. 1719–1758, 2004.
 - [11] J. Koo, J. Park, J. Lee, Y. M. Jhon, and J. H. Lee, “Femtosecond harmonic mode-locking of a fiber laser at 3.27 GHz using a bulk-like , MoSe₂-based saturable absorber,” *Opt. Express*, vol. 24, no. 10, pp. 10575–10589, 2016.
 - [12] X. Xu, J. Zhai, L. Li, Y. Chen, Y. Yu, M. Zhang, and S. Ruan, “Passively mode-locking erbium-doped fiber lasers with 0.3 nm Single-Walled Carbon Nanotubes,” *Sci. Rep.*, vol. 4, p. 6761, 2014.
 - [13] G. Sobon, “Mode-locking of fiber lasers using novel two-dimensional nanomaterials : graphene and topological insulators [Invited],” *Photon. Res.*, vol. 3, no. 2, pp. A56–A63, 2015.
 - [14] M. Pawliszewska, T. Martynkien, A. Przewloka, and J. Sotor, “Dispersion-managed Ho-doped fiber laser mode-locked with a graphene saturable absorber,” *Opt. Lett.*, vol. 43, no. 1, pp. 38–41, 2018.
 - [15] Y. Li, L. Gao, W. Huang, C. Gao, M. Liu, and T. Zhu, “All-fiber mode-locked laser via short single- wall carbon nanotubes interacting with evanescent wave in photonic crystal fiber,” *Opt. Express*, vol. 24, no. 20, pp. 23450–23458, 2016.
 - [16] Y. Chen, S. Chen, J. Liu, Y. Gao, and W. Zhang, “Sub-300 femtosecond soliton tunable fiber laser with all-anomalous dispersion passively mode locked by black phosphorus,” *Opt. Express*, vol. 24, no. 12, pp. 13316–13324, 2016.
 - [17] G. Sobon, J. Sotor, I. Pasternak, A. Krajewska, W. Strupinski, and K. M. Abramski, “Multilayer graphene-based saturable absorbers with scalable modulation depth for mode-locked Er- and Tm-doped fiber lasers,” *Opt. Mater. Express*, vol. 5, no. 12, pp. 2884–2894, 2015.
 - [18] Q. W. Sheng, M. Feng, W. Xin, H. Guo, T. Y. Han, Y. G. Li, Y. G. Liu, F. Gao, F. Song, Z. B. Liu, and J. G. Tian, “Tunable graphene saturable absorber with cross absorption modulation for mode-locking in fiber laser,” *Appl. Phys. Lett.*, vol. 105, p. 041901, 2014.
 - [19] T. Chen, C. Cheng, Y. Lin, C. Tsai, S. Member, and Y. Chi, “Optimizing the Self-Amplitude Modulation of Different 2-D Saturable Absorbers for Ultrafast Mode-Locked Fiber Lasers,” *IEEE J. Sel. Top. Quantum Electron.*, vol. 25, no.

4, p. 0900310, 2019.

- [20] S. Li, C. Wang, Y. Yin, E. Lewis, and P. Wang, "Novel layered 2D materials for ultrafast photonics," *Nanophotonics*, vol. 9, no. 7, pp. 1743–1786, 2020.
- [21] M. Liu, W. Liu, and Z. Wei, "MoTe₂ Saturable Absorber With High Modulation Depth for Erbium-Doped Fiber Laser," *J. Light. Technol.*, vol. 37, no. 13, pp. 3100–3105, 2019.
- [22] S. Y. Set, H. Yaguchi, Y. Tanaka, and M. Jablonski, "Laser Mode Locking Using a Saturable Absorber Incorporating Carbon Nanotubes," *J. Light. Technol.*, vol. 22, no. 1, pp. 51–56, 2004.
- [23] Q. Bao, H. Zhang, Y. Wang, Z. Ni, Y. Yan, Z. X. Shen, K. P. Loh, and D. Y. Tang, "Atomic-layer graphene as a saturable absorber for ultrafast pulsed lasers," *Adv. Funct. Mater.*, vol. 19, no. 19, pp. 3077–3083, 2009.
- [24] H. Zhang, S. B. Lu, J. Zheng, J. Du, S. C. Wen, D. Y. Tang, and K. P. Loh, "Molybdenum disulfide (MoS₂) as a broadband saturable absorber for ultra-fast photonics," *Opt. Express*, vol. 22, no. 6, pp. 7249–7260, 2014.
- [25] Y. Chen, G. Jiang, S. Chen, Z. Guo, X. Yu, C. Zhao, H. Zhang, Q. Bao, S. Wen, D. Tang, and D. Fan, "Mechanically exfoliated black phosphorus as a new saturable absorber for both Q-switching and mode-locking laser operation," *Opt. Express*, vol. 23, no. 10, pp. 5989–5992, 2015.
- [26] X. Wang, Y. Cui, T. Li, M. Lei, J. Li, and Z. Wei, "Recent Advances in the Functional 2D Photonic and Optoelectronic Devices," *Adv. Opt. Mater.*, vol. 1801274, pp. 1–17, 2018.
- [27] W. Liu, M. Liu, X. Liu, X. Wang, H. Deng, and M. Lei, "Recent Advances of 2D Materials in Nonlinear Photonics and Fiber Lasers," *Adv. Opt. Mater.*, vol. 1901631, pp. 1–30, 2020.
- [28] S. Liu, Y. Wang, R. Lv, J. Wang, H. Wang, Y. Wang, and L. Duan, "2D molybdenum carbide (Mo₂C)/fluorine mica (FM) saturable absorber for passively mode-locked erbium-doped all-fiber laser," *Nanophotonics*, vol. 9, no. 8, pp. 2523–2530, 2020.
- [29] C. Ma, W. Huang, Y. Wang, J. Adams, Z. Wang, J. Liu, Y. Song, Y. Ge, Z. Guo, L. Hu, and H. Zhang, "MXene saturable absorber enabled hybrid mode-locking technology: A new routine of advancing femtosecond fiber lasers performance," *Nanophotonics*, vol. 9, no. 8, pp. 2451–2458, 2020.
- [30] Z. Guo, H. Zhang, S. Lu, Z. Wang, S. Tang, J. Shao, Z. SUn, H. Xie, H. Wang, X. F. Yu, and P. K. Chu, "From Black Phosphorus to Phosphorene: Basic Solvent Exfoliation, Evolution of Raman Scattering, and Applications to Ultrafast Photonics," *Adv. Funct. Mater.*, vol. 25, no. 45, pp. 6996–7002, 2015.
- [31] H. P. Boehm, R. Setton, and E. Stumpp, "International union of pure and applied chemistry inorganic chemistry division commission on high temperature and solid state chemistry nomenclature and terminology of graphite intercalation compounds," *Pure Appl. Chem.*, vol. 66, no. 9, pp. 1893–

1901, 1994.

- [32] A. A. Balandin, S. Ghosh, W. Bao, I. Calizo, D. Teweldebrhan, F. Miao, and C. N. Lau, "Superior thermal conductivity of single-layer graphene," *Nano Lett.*, vol. 8, no. 3, pp. 902–907, 2008.
- [33] M. S. A. Bhuyan, M. N. Uddin, M. M. Islam, F. A. Bipasha, and S. S. Hossain, "Synthesis of graphene," *Int. Nano Lett.*, vol. 6, no. 2, pp. 65–83, 2016.
- [34] H. Hiura, T. W. Ebbesen, J. Fujita, K. Tanigaki, and T. Takada, "Role of sp^3 defect structures in graphite and carbon nanotubes," *Nature*, vol. 367, no. 6459, pp. 148–151, 1994.
- [35] X. Lu, M. Yu, H. Huang, and R. S. Ruoff, "Tailoring graphite with the goal of achieving single sheets," *Nanotechnology*, vol. 10, no. 3, pp. 269–272, 1999.
- [36] D. Steinberg, J. D. Zapata, and A. T. De Souza, "Mechanically Exfoliated Graphite Onto D-Shaped Optical Fiber for Femtosecond Mode-Locked Erbium-Doped Fiber Laser," *J. Light. Technol.*, vol. 36, no. 10, pp. 1868–1874, 2018.
- [37] Z. Qin, G. Xie, J. Ma, P. Yuan, and L. Qian, "2.8 μm all-fiber Q-switched and mode-locked lasers with black phosphorus," *Photon. Res.*, vol. 6, no. 11, pp. 1074–1078, 2018.
- [38] L. Ci, L. Song, D. Jariwala, A. L. Elias, W. Gao, M. Terrones, P. M. Ajayan, "Graphene shape control by multistage cutting and transfer," *Adv. Mater.*, vol. 21, no. 44, pp. 4487–4491, 2009.
- [39] X. Liang, A. S. P. Chang, Y. Zhang, B. D. Harteneck, H. Choo, and D. L. Olynick, "Electrostatic Force Assisted Exfoliation of Prepatterned Few Layer Graphenes into Device Sites.," *Nano Lett.*, vol. 9, no. 1, pp. 467–472, 2009.
- [40] X. Liang, Z. Fu, and S. Y. Chou, "Graphene transistors fabricated via transfer-printing in device active-areas on large wafer," *Nano Lett.*, vol. 7, no. 12, pp. 3840–3844, 2007.
- [41] Y. Huang, E. Sutter, J. T. Sadowski, M. Cotlet, O. L. A. Monti, D. A. Racke, M. R. Neupane, D. Wickramaratne, R. K. Lake, B. A. Parkinson, and P. Sutter, "Tin Disulfide ; An Emerging Layered Metal Dichalcogenide Semiconductor : Materials Properties and Device Characteristics," *ACS Nano*, vol. 8, no. 10, pp. 10743–10755, 2014.
- [42] C. Ruppert, O. B. Aslan, and T. F. Heinz, "Optical Properties and Band Gap of Single- and Few-Layer MoTe_2 Crystals," *Nano Lett.*, vol. 14, no. 11, pp. 6231–6236, 2014.
- [43] H. R. Gutie, N. Perea-lo, A. Laura, A. Berkdemir, B. Wang, and M. Terrones, "Extraordinary Room-Temperature Photoluminescence in Triangular WS_2 Monolayers," *Nano Lett.*, vol. 13, pp. 3447–3454, 2013.
- [44] D. Mao, X. She, B. Du, D. Yang, W. Zhang, K. Song, X. Cui, B. Jiang, T. Peng, and J. Zhao, "Erbium-doped fiber laser passively mode locked with few-layer $\text{WSe}_2/\text{MoSe}_2$ nanosheets," *Sci. Rep.*, vol. 6, p. 23583, 2016.

- [45] E. J. Aiub, D. Steinberg, E. A. T. De Souza, and L. A. M. Saito, “200-fs mode-locked Erbium-doped fiber laser by using mechanically exfoliated MoS₂ saturable absorber onto D-shaped optical fiber,” *Opt. Express*, vol. 25, no. 9, pp. 10546–10552, 2017.
- [46] H. Liu, A. T. Neal, Z. Zhu, Z. Luo, X. Xu, D. Tomanek, and P. D. Ye, “Phosphorene : An Unexplored 2D Semiconductor with a High Hole Mobility,” *ACS Nano*, vol. 8, no. 4, pp. 4033–4041, 2014.
- [47] J. Sotor, G. Sobon, M. Kowalczyk, W. Mzcherzynski, P. Paletko, and K. M. Abramski, “Ultrafast thulium-doped fiber laser mode locked with black phosphorus,” *Opt. Lett.*, vol. 40, no. 16, pp. 3885–3888, 2015.
- [48] J. Yin, F. Zhu, J. Lai, H. Chen, M. Zhang, J. Zhang, J. Wang, T. He, B. Zhang, J. Yuan, P. Yan, and S. Ruan, “Hafnium Sulfide Nanosheets for Ultrafast Photonic Device,” *Adv. Opt. Mater.*, vol. 1801303, pp. 1–8, 2018.
- [49] J. Du, M. Zhang, Z. Guo, J. Chen, X. Zhu, G. Hu, P. Peng, Z. Zheng, and H. Zhang, “Phosphorene quantum dot saturable absorbers for ultrafast fiber lasers,” *Sci. Rep.*, vol. 7, p. 42357, 2017.
- [50] K. Wu, X. Zhang, J. Wang, X. Li, and J. Chen, “WS₂ as a saturable absorber for ultrafast photonic applications of mode-locked and Q- switched lasers,” *Opt. Express*, vol. 23, no. 9, pp. 11453–11461, 2015.
- [51] X. Xu, M. He, C. QUAN, R. Wang, C. Liu, Q. Zhao, Y. Zhou, J. Bai, and X. Xu, “Saturable Absorption Properties of ReS₂ Films and Mode-Locking Application Based on Double-Covered ReS₂ Micro Fiber,” *J. Light. Technol.*, vol. 36, no. 22, pp. 5130–5136, 2018.
- [52] Z. Qin, G. Xie, C. Zhao, S. Wen, P. Yuan, and L. Qian, “Mid-infrared mode-locked pulse generation with multilayer black phosphorus as saturable absorber,” *Opt. Lett.*, vol. 41, no. 1, pp. 56–59, 2016.
- [53] R. Khazaeinezhad, S. H. Kassani, H. Jeong, D. Yeom, and K. Oh, “Femtosecond Soliton Pulse Generation Using Evanescent Field Interaction Through Tungsten Disulfide (WS₂) Film,” *J. Light. Technol.*, vol. 33, no. 17, pp. 3550–3557, 2015.
- [54] R. Khazaeinezhad, S. H. Kassani, H. Jeong, T. Nazari, D.-I. Yeom, and K. Oh, “Mode-Locked All-Fiber Lasers at Both Anomalous and Normal Dispersion Regimes Based on Spin-Coated MoS₂ Nano-Sheets on a Side-Polished Fiber,” *IEEE Photonics J.*, vol. 7, no. 1, p. 1500109, 2015.
- [55] F. Torrisi, D. Popa, S. Milana, Z. Jiang, T. Hasan, E. Lidorikis, and A. C. Ferrari, “Stable, Surfactant-Free Graphene-Styrene Methylmethacrylate Composite for Ultrafast Lasers,” *Adv. Opt. Mater.*, vol. 4, pp. 1088–1097, 2016.
- [56] Y. Xu, Z. Wang, Z. Guo, H. Huang, Q. Xiao, and H. Zhang, “Solvothetmal Synthesis and Ultrafast Photonics of Black Phosphorus Quantum Dots,” *Adv. Opt. Mater.*, vol. 4, pp. 1223–1229, 2016.
- [57] L. Lu, Z. Liang, L. Wu, Y. Chen, Y. Song, S. C. Dhanabalan, J. S. Ponraj, B.

- Dong, and Y. Xiang, “Few-layer Bismuthene: Sonochemical Exfoliation , Nonlinear Optics and Applications for Ultrafast Photonics with Enhanced Stability,” *Laser Photon. Rev.*, vol. 12, p. 1700221, 2018.
- [58] K. Niu, R. Sun, Q. Chen, B. Man, and H. Zhang, “Passively mode-locked Er-doped fiber laser based on SnS₂ nanosheets as a saturable absorber,” *Photon. Res.*, vol. 6, no. 2, pp. 72–76, 2018.
- [59] M. Chernysheva, M. Al Araithi, G. A. Rance, N. J. Weston, B. Shi, S. Saied, J. L. Sullivan, N. Marsh, and A. Rozhin, “Revealing the nature of morphological changes in carbon nanotube-polymer saturable absorber under high-power laser irradiation,” *Sci. Rep.*, vol. 8, p. 7491, 2018.
- [60] D. Li, H. Jussila, Y. Wang, G. Hu, T. Albrow-owe, R. C. T. Howe, Z. Ren, J. Bai, T. Hasan, and Z. Sun, “Wavelength and pulse duration tunable ultrafast fiber laser mode- locked with carbon nanotubes,” *Sci. Rep.*, vol. 8, p. 2738, 2018.
- [61] Y. Song, Z. Liang, X. Jiang, Y. Chen, Z. Li, L. Lu, Y. Ge, K. Wang, J. Zheng, S. Lu, J. Ji, and H. Zhang, “Few-layer antimonene decorated microfiber: ultra-short pulse generation and all-optical thresholding with enhanced long term stability,” *2D Mater.*, vol. 4, no. 4, p. 045010, 2017.
- [62] H. Ahmad, M. Tajdidzadeh, M. Rezayi, and I. S. Amiri, “Passive mode-locking at S-band by single-mode thulium-doped fluoride fiber using a thin film PtAg/N-G saturable absorber,” *J. Nanophotonics*, vol. 11, no. 2, p. 026008, 2017.
- [63] D. Steinberg, H. G. Rosa, and E. A. T. De Souza, “Influence of Carbon Nanotubes Saturable Absorbers Diameter on Mode-Locking Erbium-Doped Fiber Laser Performance,” *J. Light. Technol.*, vol. 35, no. 21, pp. 4804–4808, 2017.
- [64] S. Lu, Y. Ge, Z. Sun, Z. Huang, R. Cao, C. Zhao, S. Wen, D. Fan, J. Li, and H. Zhang, “Ultrafast nonlinear absorption and nonlinear refraction in few-layer oxidized black phosphorus,” *Photon. Res.*, vol. 4, no. 6, pp. 286–292, 2016.
- [65] X. Z. Hu, S. C. Hen, M. Z. Hang, L. C. Hen, and J. Z. Hao, “TiS₂-based saturable absorber for ultrafast fiber lasers,” *Photon. Res.*, vol. 6, no. 10, pp. C44–C48, 2018.
- [66] S. Liu, Z. Li, Y. Ge, H. Wang, R. Yue, X. Jiang, J. Li, Q. Wen, and H. Zhang, “Graphene / phosphorene nano-heterojunction: facile synthesis, nonlinear optics, and ultrafast photonics applications with enhanced performance,” *Photon. Res.*, vol. 5, no. 6, pp. 662–668, 2017.
- [67] Z. Luo, Y. Li, M. Zhong, Y. Huang, X. Wan, J. Peng, and J. Weng, “Nonlinear optical absorption of few-layer molybdenum diselenide (MoSe₂) for passively mode-locked soliton fiber laser [Invited],” *Photon. Res.*, vol. 3, no. 3, pp. A79–A86, 2015.
- [68] D. Mao, Y. Wang, C. Ma, L. Han, B. Jiang, X. Gan, S. Hua, and W. Zhang, “WS₂ mode-locked ultrafast fiber laser,” *Sci. Rep.*, vol. 5, p. 7965, 2015.

- [69] K. Wu, X. Zhang, J. Wang, and J. Chen, “463-MHz fundamental mode-locked fiber laser based on few-layer MoS₂ saturable absorber,” *Opt. Lett.*, vol. 40, no. 7, pp. 1374–1377, 2015.
- [70] D. Mao, X. Cui, X. Gan, M. Li, W. Zhang, H. Lu, and J. Zhao, “Passively Q-Switched and Mode-Locked Fiber Laser Based on an ReS₂ Saturable Absorber,” *IEEE J. Sel. Top. Quantum Electron.*, vol. 24, no. 3, p. 1100406, 2018.
- [71] B. Guo, S.-H. Wang, Z.-X. Wu, Z.-X. Wang, D.-H. Wang, H. Huang, F. Zhang, Y.-Q. Ge, and H. Zhang, “Sub-200 fs soliton mode-locked fiber laser based on bismuthene saturable absorber,” *Opt. Express*, vol. 26, no. 18, pp. 22750–22760, 2018.
- [72] X. Jin, G. Hu, M. Zhang, Y. Hu, T. Albrow-Owen, R. C. T. Howe, T.-C. Wu, Q. Wu, Z. Zheng, and T. Hasan, “102 fs pulse generation from a long-term stable, inkjet-printed black phosphorus-mode-locked fiber laser,” *Opt. Express*, vol. 26, no. 10, pp. 12506–12513, 2018.
- [73] R. Zhao, G. Li, B. Zhang, and J. He, “Multi-wavelength bright-dark pulse pair fiber laser based on rhenium disulfide,” *Opt. Express*, vol. 26, no. 5, pp. 5819–5826, 2018.
- [74] M. Pawliszewska, Y. Ge, Z. Li, H. Zhang, and J. Sotor, “Fundamental and harmonic mode-locking at 2.1 μm with black phosphorus saturable absorber,” *Opt. Express*, vol. 25, no. 15, pp. 16916–16921, 2017.
- [75] L. Yun, “Black phosphorus saturable absorber for dual-wavelength polarization-locked vector soliton generation,” *Opt. Express*, vol. 25, no. 26, pp. 32380–32385, 2017.
- [76] Y. Song, S. Chen, Q. Zhang, H. Zhang, and D. Tang, “Vector soliton fiber laser passively mode locked by few layer black phosphorus-based optical saturable absorber,” *Opt. Express*, vol. 24, no. 23, pp. 25933–25942, 2016.
- [77] Z. Luo, M. Liu, Z. Guo, X. Jiang, A. Luo, C. Zhao, X. Yu, W. Xu, and H. Zhang, “Microfiber-based few-layer black phosphorus saturable absorber for ultra-fast fiber laser,” *Opt. Express*, vol. 23, no. 15, pp. 20030–20039, 2015.
- [78] J. Li, Y. Zhao, Q. Chen, K. Niu, and R. Sun, “Passively Mode-Locked Ytterbium-Doped Fiber Laser Based on SnS₂ as Saturable Absorber,” *IEEE Photonics J.*, vol. 9, no. 6, p. 1506707, 2017.
- [79] N. Xu, W. Yang, and H. Zhang, “Nonlinear saturable absorption properties of indium selenide and its application for demonstrating a Yb-doped mode-locked fiber laser,” *Opt. Mater. Express*, vol. 8, no. 10, pp. 3092–3103, 2018.
- [80] B. Guo, Q. Lyu, Y. Yao, and P. Wang, “Direct generation of dip-type sidebands from WS₂ mode-locked fiber laser,” *Opt. Mater. Express*, vol. 6, no. 8, pp. 2475–2486, 2016.
- [81] W. Liu, M. Liu, X. Liu, X. Wang, H. Teng, M. Lei, Z. Wei, and Z. Wei, “Saturable absorption properties and femtosecond mode-locking application of titanium trisulfide Saturable absorption properties and femtosecond mode-

- locking application of titanium trisulfide,” *Appl. Phys. Lett.*, vol. 061901, pp. 1–4, 2020.
- [82] G. Liu, J. Yuan, T. Wu, S. Member, F. Zhang, F. Xing, and W. Zhang, “Ultrathin 2D nonlayered tellurene nanosheets as saturable absorber for picosecond pulse generation in all-fiber lasers,” *J. Sel. Top. Quantum Electron.*, vol. 27, no. 2, pp. 1–6, 2020.
 - [83] W. Zhang, G. Wang, F. Xing, Z. Man, F. Zhang, K. Han, H. Zhang, and S. Fu, “Passively Q-switched and mode-locked erbium-doped fiber lasers based on tellurene nanosheets as saturable absorber,” *Opt. Express*, vol. 28, no. 10, pp. 35–38, 2020.
 - [84] P. K. Cheng, C. Y. Tang, X. Y. Wang, L.-H. Zeng, and Y. H. Tsang, “Passively Q-switched and femtosecond mode-locked erbium-doped fiber laser based on a 2D palladium disulfide (PdS₂) saturable absorber,” *Photon. Res.*, vol. 8, no. 4, 2020.
 - [85] J. Yin, J. Li, H. Chen, J. Wang, P. Yan, M. Liu, W. Liu, W. Lu, Z. Xu, W. Zhang, J. Wang, Z. Sun, and S. Ruan, “Large-area highly crystalline WSe₂ atomic layers for ultrafast pulsed lasers,” *Opt. Express*, vol. 25, no. 24, pp. 30020–30031, 2017.
 - [86] J. Wang, H. Chen, Z. Jiang, J. Yin, J. Wang, M. Zhang, T. He, J. Li, P. Yan, and S. Ruan, “Mode-locked thulium-doped fiber laser with chemical vapor deposited molybdenum ditelluride,” *Opt. Lett.*, vol. 43, no. 9, pp. 1998–2001, 2018.
 - [87] J. Wang, W. Lu, J. Li, H. Chen, Z. Jiang, J. Wang, W. Zhang, and M. Zhang, “Ultrafast Thulium-Doped Fiber Laser Mode Locked by Monolayer WSe₂,” *IEEE J. Sel. Top. Quantum Electron.*, vol. 24, no. 3, p. 1100706, 2018.
 - [88] J. Sotor, M. Pawliszewska, G. Sobon, P. Kaczmarek, A. Przewolka, I. Pasternak, J. Cajzl, P. Peterka, P. Honzátko, I. Kasik, W. Strupinski, and K. M. Abramski, “All-fiber Ho-doped mode-locked oscillator based on a graphene saturable absorber,” *Opt. Lett.*, vol. 41, no. 11, pp. 2592–2595, 2016.
 - [89] X. M. Liu, H. R. Yang, Y. D. Cui, G. W. Chen, Y. Yang, X. Q. Wu, X. K. Yao, and D. D. Han, “Graphene-clad microfibre saturable absorber for ultrafast fibre lasers,” *Sci. Rep.*, vol. 6, p. 26024, 2016.
 - [90] J. Gene, N. H. Park, H. Jeong, S. Choi, F. Rotermund, D.-I. Yeom, and B. Y. Kim, “Optically controlled in-line graphene saturable absorber for the manipulation of pulsed fiber laser operation,” *Opt. Express*, vol. 24, no. 19, pp. 21301–21307, 2016.
 - [91] G. Sobon, J. Sotor, I. Pasternak, A. Krajewska, and K. M. Abramski, “All-polarization maintaining, graphene-based femtosecond Tm-doped all-fiber laser,” *Opt. Express*, vol. 23, no. 7, pp. 9339–9346, 2015.
 - [92] K. Zhang, M. Feng, Y. Ren, F. Liu, X. Chen, J. Yang, X.-Q. Yan, F. Song, and J. Tian, “Q-switched and mode-locked Er-doped fiber laser using PtSe₂ as a saturable absorber,” *Photon. Res.*, vol. 6, no. 9, pp. 893–899, 2018.

- [93] Y. Cui, F. Lu, and X. Liu, “Nonlinear Saturable and Polarization-induced Absorption of Rhenium Disulfide,” *Sci. Rep.*, vol. 7, p. 40080, 2017.
- [94] Y. Cui, F. Lu, and X. Liu, “MoS₂-clad microfibre laser delivering conventional, dispersion-managed and dissipative solitons,” *Sci. Rep.*, vol. 6, p. 30524, 2016.
- [95] W. Li, L. Yi, R. Zheng, Z. Ni, and W. Hu, “Fabrication and application of a graphene polarizer with strong saturable absorption,” *Photon. Res.*, vol. 4, no. 2, pp. 41–44, 2016.
- [96] N. H. Park, H. Jeong, S. Y. Choi, M. H. Kim, and F. Rotermund, “Monolayer graphene saturable absorbers with strongly enhanced evanescent-field interaction for ultrafast fiber laser mode-locking,” *Opt. Express*, vol. 23, no. 15, pp. 19806–19812, 2015.
- [97] M. Chernysheva, A. Bednyakova, M. Al Araithi, R. C. T. Howe, G. Hu, T. Hasan, A. Gambetta, G. Galzerano, and M. Rümeli, “Double-Wall Carbon Nanotube Hybrid Mode-Locker in Tm-doped Fibre Laser: A Novel Mechanism for Robust Bound-State Solitons Generation,” *Sci. Rep.*, vol. 7, p. 44314, 2017.
- [98] S. Kobtsev, A. Ivanenko, Y. G. Gladush, B. Nyushkov, A. Kokhanovskiy, A. S. Anisimov, and A. G. Nasibulin, “Ultrafast all-fibre laser mode-locked by polymer-free carbon nanotube film,” *Opt. Express*, vol. 24, no. 25, pp. 28768–28773, 2016.
- [99] H. Chen, C. Tsai, C. Chang, K. Lin, C. Chang, and W. Hsieh, “Investigation of Graphene Dispersion From Kelly Sideband in Stable Mode-Locked Erbium-Doped Fiber Laser by Few-Layer Graphene Saturable Absorbers,” *J. Light. Technol.*, vol. 33, no. 21, pp. 4406–4412, 2015.
- [100] F. Bonaccorso, A. Lombardo, T. Hasan, Z. Sun, L. Colombo, and A. C. Ferrari, “Production and processing of graphene and 2D crystals Graphene is at the center of an ever growing research effort due to its unique to these crystals , accelerating their journey towards applications,” *Mater. Today*, vol. 15, no. 12, pp. 564–589, 2012.
- [101] H. Chen, J. Yin, J. Yang, X. Zhang, M. Liu, Z. Jiang, J. Wang, Z. Sun, T. Guo, W. Liu, and P. Yan, “Transition-metal dichalcogenides heterostructure saturable absorbers for ultrafast photonics,” *Opt. Lett.*, vol. 42, no. 21, pp. 4279–4282, 2017.
- [102] B. Fu, J. Li, Z. Cao, and P. Daniel, “Bound states of solitons in a harmonic graphene-mode-locked fiber laser,” *Photon. Res.*, vol. 7, no. 2, pp. 116–120, 2019.
- [103] D. Steinberg, R. M. Gerosa, F. N. Pellicer, J. D. Zapata, S. H. Domingues, E. A. T. De Souza, and L. A. M. Saito, “Graphene oxide and reduced graphene oxide as saturable absorbers onto D-shaped fibers for sub 200-fs EDFL mode-locking,” *Opt. Mater. Express*, vol. 8, no. 1, pp. 144–156, 2018.
- [104] C. Yang, C. Wu, Y. Lin, L. Tsai, Y. Chi, J. Chang, C. Wu, H. Tsai, D. Tsai, and G. Lin, “Fabricating graphite nano-sheet powder by slow electrochemical

- exfoliation of large-scale graphite foil as a mode-locker for fiber lasers,” *Opt. Mater. Express*, vol. 3, no. 11, pp. 1893–1905, 2013.
- [105] K. Wei, S. Fan, Q. Chen, and X. Lai, “Passively mode-locked Yb fiber laser with PbSe colloidal quantum dots as saturable absorber,” *Opt. Express*, vol. 25, no. 21, pp. 3771–3774, 2017.
 - [106] Y. Ge, Z. Zhu, Y. Xu, Y. Chen, S. Chen, Z. Liang, and D. Fan, “Broadband Nonlinear Photoresponse of 2D TiS₂ for Ultrashort Pulse Generation and All-Optical Thresholding Devices,” *Adv. Opt. Mater.*, vol. 1701166, pp. 1–10, 2018.
 - [107] X. Jiang, L. Zhang, S. Liu, Y. Zhang, Z. He, and W. Li, “Ultrathin Metal–Organic Framework : An Emerging Broadband Nonlinear Optical Material for Ultrafast Photonics,” *Adv. Opt. Mater.*, vol. 1800561, pp. 1–11, 2018.
 - [108] Z. Wang, Y. Xu, S. C. Dhanabalan, J. Sophia, C. Zhao, C. Xu, Y. Xiang, J. Li, and H. Zhang, “Black Phosphorus Quantum Dots as an Efficient Saturable Absorber for Bound Soliton Operation in an Erbium Doped Fiber Laser,” *IEEE Photonics J.*, vol. 8, no. 5, p. 1503310, 2016.
 - [109] Y. Zhou, M. Zhao, S. Wang, H. Chen-Xia, Y. Wang, S. Yan, Y. Li, J. Xu, Y. Tang, G. Lin-Feng, Q. Wang, and H.-L. Zhang, “Developing carbon-nitride nanosheets for mode-locking ytterbium fiber lasers,” *Opt. Lett.*, vol. 41, no. 6, pp. 6–9, 2016.
 - [110] J. Feng, X. Li, Z. Shi, C. Zheng, X. Li, D. Leng, Y. Wang, J. Liu, and L. Zhu, “2D Ductile Transition Metal Chalcogenides (TMCs): Novel High-Performance Ag₂S Nanosheets for Ultrafast Photonics,” *Adv. Opt. Mater.*, vol. 1901762, pp. 1–9, 2019.
 - [111] L. Yun, Y. Qiu, C. Yang, J. Xing, K. Yu, X. Xu, and W. Wei, “PbS quantum dots as a saturable absorber for ultrafast laser,” *Photon. Res.*, vol. 6, no. 11, pp. 1028–1032, 2018.
 - [112] G. Sobon, A. Duzynska, M. Świniarski, J. Judek, and J. Sotor, “CNT-based saturable absorbers with scalable modulation depth for Thulium-doped fiber lasers operating at 1.9 μm ,” *Sci. Rep.*, vol. 7, p. 45491, 2017.
 - [113] J. Boguslawski, J. Sotor, G. Sobon, R. Kozinski, K. Librant, M. Aksienionek, L. Lipinska, and K. M. Abramski, “Graphene oxide paper as a saturable absorber for Er- and Tm-doped fiber lasers,” *Photon. Res.*, vol. 3, no. 4, pp. 119–124, 2015.
 - [114] P. Yan, H. Chen, A. Liu, K. Li, S. Ruan, J. Ding, X. Qiu, and T. Guo, “Self-Starting Mode-Locking by Fiber-Integrated WS₂ Saturable Absorber Mirror,” *IEEE J. Sel. Top. Quantum Electron.*, vol. 23, no. 1, p. 1100106, 2017.
 - [115] J. Wang, Z. Jiang, H. Chen, J. Li, J. Yin, J. Wang, T. He, P. Yan, and S. Ruan, “High energy soliton pulse generation by a magnetron-sputtering-deposition-grown MoTe₂ saturable absorber,” *Photon. Res.*, vol. 6, no. 6, pp. 535–541, 2018.

- [116] J. Wang, Z. Jiang, H. Chen, J. Li, J. Yin, J. Wang, T. He, P. Yan, and S. Ruan, "Magnetron-sputtering deposited WTe_2 for an ultrafast thulium-doped fiber laser," *Opt. Lett.*, vol. 42, no. 23, pp. 5010–5013, 2017.
- [117] X. Liu, Q. Gao, Y. Zheng, D. Mao, and J. Zhao, "Recent progress of pulsed fiber lasers based on transition-metal dichalcogenides and black phosphorus saturable absorbers," *Nanophotonics*, vol. 9, no. 8, pp. 2215–2231, 2020.
- [118] Z. Luo, D. Wu, B. Xu, H. Xu, Z. Cai, J. Peng, J. Weng, S. Xu, C. Zhu, F. Wang, and Z. Sun, "Two-dimensional material-based saturable absorbers: Towards compact visible-wavelength all-fiber pulsed lasers," *Nanoscale*, vol. 8, no. 2, pp. 1066–1072, 2016.
- [119] M. Calvaresi, M. Quintana, P. Rudolf, and F. Zerbetto, "Rolling up a Graphene Sheet," *ChemPhysChem*, vol. 14, pp. 3447–3453, 2013.
- [120] A. G. Rozhin, V. Scardaci, F. Wang, F. Hennrich, I. H. White, and W. I. Milne, "Generation of ultra-fast laser pulses using nanotube mode-locks," *Phys. Stat. Soli.*, vol. 3555, no. 13, pp. 3551–3555, 2006.
- [121] Y. Meng, Y. Li, Y. Xu, and F. Wang, "Carbon Nanotube Mode-Locked Thulium Fiber Laser With 200 nm Tuning Range," *Sci. Rep.*, vol. 7, p. 45109, 2017.
- [122] J. Wang, X. Liang, G. Hu, Z. Zheng, and S. Lin, "152 fs nanotube-mode-locked thulium-doped all-fiber laser," *Sci. Rep.*, vol. 6, p. 28885, 2016.
- [123] M. A. Solodyankin, E. D. Obraztsova, A. S. Lobach, A. I. Chernov, A. V. Tausenev, V. I. Konov, and E. M. Dianov, "Mode-locked 1.93 μm thulium fiber laser with a carbon nanotube absorber," *Opt. Lett.*, vol. 33, no. 12, pp. 1336–1338, 2008.
- [124] A. Martinez and Z. Sun, "Nanotube and graphene saturable absorbers for fibre lasers," *Nat. Photonics*, vol. 7, pp. 842–845, 2013.
- [125] B. T. Hasan, Z. Sun, F. Wang, F. Bonaccorso, P. H. Tan, A. G. Rozhin, and A. C. Ferrari, "Nanotube–polymer composites for ultrafast photonics," *Adv. Mater.*, vol. 21, pp. 3874–3899, 2009.
- [126] X. Li, K. Wu, Z. Sun, B. Meng, Y. Wang, Y. Wang, X. Yu, X. Yu, Y. Zhang, P. P. Shum, and Q. J. Wang, "Single-wall carbon nanotubes and graphene oxide-based saturable absorbers for low phase noise mode-locked fiber lasers," *Sci. Rep.*, vol. 6, p. 25266, 2016.
- [127] K. Peng, Y. Lin, C. Wu, S. Lin, C. Yang, S. Lin, D. Tsai, and G. Lin, "Dissolution-and-reduction CVD synthesis of few-layer graphene on ultra-thin nickel film lifted off for mode-locking fiber lasers," *Sci. Rep.*, vol. 5, p. 13689, 2015.
- [128] I. Hernandez-romano, D. Mandridis, J. J. Sanchez-mondragon, D. A. May-arrioja, and P. J. Delfyett, "Hybrid Mode Locked Fiber Laser Using a PDMS/SWCNT Composite Operating at 4 GHz," *J. Light. Technol.*, vol. 29, no. 21, pp. 3237–3242, 2011.

- [129] Y. Cui and X. Liu, "Graphene and nanotube mode-locked fiber laser emitting dissipative and conventional solitons," *Opt. Express*, vol. 21, no. 16, pp. 18969–18974, 2013.
- [130] K. Cheng, Y. Lin, and S. Absorber, "Harmonic Order-Dependent Pulseswidth Shortening of a Passively Mode-Locked Fiber Laser With a Carbon Nanotube Harmonic Order-Dependent Pulseswidth Shortening of a Passively Mode-Locked Fiber Laser With a Carbon Nanotube," *IEEE Photonics J.*, vol. 4, no. 5, pp. 1542–1552, 2012.
- [131] F. Bonaccorso, Z. Sun, T. Hasan, and A. C. Ferrari, "Graphene Photonics and Optoelectronics," *Nat. Photonics*, vol. 4, pp. 611–622, 2010.
- [132] C. Jia, B. J. Shastri, N. Abdukerim, M. Rochette, P. R. Prucnal, M. Saad, and L. R. Chen, "Passively synchronized Q-switched and mode-locked dual-band Tm 3^{+} : ZBLAN fiber lasers using a common graphene saturable absorber," *Sci. Rep.*, vol. 6, p. 36071, 2016.
- [133] D. Popa, Z. Sun, F. Torrisi, T. Hasan, F. Wang, D. Popa, Z. Sun, F. Torrisi, T. Hasan, F. Wang, and A. C. Ferrari, "Sub 200 fs pulse generation from a graphene mode-locked fiber laser," *Appl. Phys. Lett.*, vol. 97, no. 20, p. 203106, 2010.
- [134] L. Miao, Y. Jiang, S. Lu, B. Shi, C. Zhao, H. Zhang, and S. Wen, "Broadband ultrafast nonlinear optical response of few-layers graphene: toward the mid-infrared regime," *Photon. Res.*, vol. 3, no. 5, pp. 214–219, 2015.
- [135] Z. Sun, T. Hasan, F. Torrisi, D. Popa, G. Privitera, F. Wang, F. Bonaccorso, D. M. Basko, and A. C. Ferrari, "Graphene mode-locked ultrafast laser," *ACS Nano*, vol. 4, no. 2, pp. 803–810, 2010.
- [136] A. Gupta, G. Chen, P. Joshi, S. Tadigadapa, and P. C. Eklund, "Raman scattering from high-frequency phonons in supported n-graphene layer films," *Nano Lett.*, vol. 6, no. 12, pp. 2667–2673, 2006.
- [137] F. Banhart, J. Kotakoski, and A. V. Krashennnikov, "Structural Defects in Graphene," *ACS Nano*, vol. 5, no. 1, pp. 26–41, 2011.
- [138] Y.-H. Lin, C.-Y. Yang, S.-F. Lin, and G.-R. Lin, "Triturating versatile carbon materials as saturable absorptive nano powders for ultrafast pulsating of erbium-doped fiber lasers," *Opt. Mater. Express*, vol. 5, no. 2, pp. 236–253, 2015.
- [139] H. G. Rosa, D. Steinberg, J. D. Zapata, A. M. Saito, and M. C. Ana, "Raman Mapping Characterization of All-Fiber CVD Monolayer Graphene Saturable Absorbers for Erbium-Doped Fiber Laser Mode Locking," *J. Light. Technol.*, vol. 33, no. 19, pp. 4118–4123, 2015.
- [140] J. Li, H. Luo, B. Zhai, R. Lu, Z. Guo, H. Zhang, and Y. Liu, "Black phosphorus: a two-dimension saturable absorption material for locked fiber lasers," *Sci. Rep.*, vol. 6, p. 30361, 2016.
- [141] J. Chen, B. Zheng, G. Shao, S. Ge, F. Xu, and Y. Lu, "An all-optical modulator

- based on a stereo graphene – microfiber structure,” *Light Sci. Appl.*, vol. 4, p. e360, 2015.
- [142] W. Wang, W. Yue, Z. Liu, T. Shi, J. Du, and Y. Leng, “Ultrafast Nonlinear Optical Response in Plasmonic 2D Molybdenum Oxide Nanosheets for Mode-Locked Pulse Generation,” *Adv. Opt. Mater.*, vol. 1700948, pp. 1–8, 2018.
 - [143] P. Yan, A. Liu, Y. Chen, J. Wang, S. Ruan, H. Chen, and J. Ding, “Passively mode-locked fiber laser by a cell-type WS₂ nanosheets saturable absorber,” *Sci. Rep.*, vol. 5, p. 12587, 2015.
 - [144] K. P. Loh, Q. Bao, G. Eda, and M. Chhowalla, “Graphene oxide as a chemically tunable platform for optical applications,” *Nat. Chem.*, vol. 2, pp. 1015–1024, 2010.
 - [145] X. Zhao, Z. Liu, W. Yan, Y. Wu, X. Zhang, Y. Chen, J. Tian, X. Zhao, Z. Liu, W. Yan, Y. Wu, and X. Zhang, “Ultrafast carrier dynamics and saturable absorption of solution-processable few-layered graphene oxide Ultrafast carrier dynamics and saturable absorption of solution-processable few-layered graphene oxide,” *Appl. Phys. Lett.*, vol. 98, p. 121905, 2011.
 - [146] J. Zhu, Y. Li, Y. Chen, W. J. Blau, and J. Wang, “Graphene oxide covalently functionalized with zinc phthalocyanine for broadband optical limiting,” *Carbon N. Y.*, vol. 49, pp. 1900–1905, 2011.
 - [147] X. He, Z. Liu, D. Wang, M. Yang, C. R. Liao, and X. Zhao, “Passively Mode-Locked Fiber Laser Based on Reduced Graphene Oxide on Microfiber for Ultra-Wide-Band Doublet Pulse Generation,” *J. Light. Technol.*, vol. 30, no. 7, pp. 984–989, 2012.
 - [148] R. Philip, P. Chantharasupawong, H. Qian, R. Jin, and J. Thomas, “Evolution of Nonlinear Optical Properties: From Gold Atomic Clusters to Plasmonic Nanocrystals,” *Nano Lett.*, vol. 12, no. 9, pp. 4661–4667, 2012.
 - [149] V. Vanyukov, V. Bondar, and A. Chuvilin, “Saturable absorption in detonation nanodiamond dispersions,” *J. Nanophotonics*, vol. 11, no. 3, p. 032506, 2017.
 - [150] W. Zhang, L. Zhan, T. Xian, and L. Gao, “Generation of Bright/Dark Pulses in an erbium-doped fiber laser mode-locked with glycerin,” *J. Light. Technol.*, vol. 37, no. 15, pp. 3756–3760, 2019.
 - [151] Z. Wang, L. Zhan, J. Wu, Z. Zhou, L. Zhang, K. Qian, L. He, and X. Fang, “Self-starting ultrafast fiber lasers mode-locked with alcohol,” *Opt. Lett.*, vol. 40, no. 16, pp. 1–4, 2015.
 - [152] C. Lu, Y. Yang, J. Wang, R. Fu, X. Zhao, L. Zhao, Y. Ming, Y. Hu, H. Lin, X. Tao, Y. Li, and W. Chen, “High-performance graphdiyne-based electrochemical actuators,” *Nat. Commun.*, vol. 9, no. 752, pp. 1–11, 2018.
 - [153] H. Yu, H. Yu, Y. Xue, B. Huang, L. Hui, C. Zhang, Y. Fang, Y. Liu, and Y. Zhao, “Ultrathin Nanosheet of Graphdiyne-Supported Palladium Atom Catalyst for Efficient Hydrogen Production Ultrathin Nanosheet of Graphdiyne-Supported Palladium Atom Catalyst for Efficient Hydrogen Production,”

iScience, vol. 11, pp. 31–41, 2018.

- [154] J. Zhou, J. Li, Z. Liu, and J. Zhang, “Exploring Approaches for the Synthesis of Few-Layered Graphdiyne,” *Adv. Mater.*, vol. 1803758, pp. 1–16, 2019.
- [155] L. Wu, Y. Dong, J. Zhao, D. Ma, W. Huang, Y. Zhang, Y. Wang, X. Jiang, Y. Xiang, J. Li, and Y. Feng, “Kerr Nonlinearity in 2D Graphdiyne for Passive Photonic Diodes,” *Adv. Mater.*, vol. 1807981, pp. 1–10, 2019.
- [156] S. A. Han, R. Bhatia, and S. Kim, “Synthesis, properties and potential applications of two-dimensional transition metal dichalcogenides,” *Nano Converg.*, vol. 2, no. 17, pp. 1–14, 2015.
- [157] Y. Jiang, L. Miao, G. Jiang, Y. Chen, X. Qi, and X. Jiang, “Broadband and enhanced nonlinear optical response of MoS₂/graphene nanocomposites for ultrafast photonics applications,” *Sci. Rep.*, vol. 5, p. 16372, 2015.
- [158] M. Zhang, G. Hu, G. Hu, R. C. T. Howe, L. Chen, Z. Zheng, and T. Hasan, “Yb- and Er-doped fiber laser Q-switched with an optically uniform, broadband WS₂ saturable absorber,” *Sci. Rep.*, vol. 5, p. 17842, 2015.
- [159] Q. H. Wang, K. Kalantar-zadeh, A. Kis, J. N. Coleman, and M. S. Strano, “Electronics and optoelectronics of two-dimensional transition metal dichalcogenides,” *Nat. Nanotechnol.*, vol. 7, pp. 699–712, 2012.
- [160] S. Bikorimana, P. Lama, A. Walser, R. Dorsinville, S. Anghel, A. Mitioglu, A. Micu, and L. Kulyuk, “Nonlinear optical responses in two-dimensional transition metal dichalcogenide multilayer: WS₂, WSe₂, MoS₂ and Mo_{0.5}W_{0.5}S₂,” *Opt. Express*, vol. 24, no. 18, pp. 20685–20695, 2016.
- [161] H. Shi, R. Yan, S. Bertolazzi, J. Brivio, B. Gao, A. Kis, and D. Jena, “Exciton Dynamics in Suspended 2D Crystals,” *ACS Nano*, vol. 7, pp. 1072–1080, 2013.
- [162] J. Du, Q. Wang, G. Jiang, C. Xu, C. Zhao, Y. Xiang, Y. Chen, S. Wen, and H. Zhang, “Ytterbium-doped fiber laser passively mode locked by few-layer Molybdenum Disulfide (MoS₂) saturable absorber functioned with evanescent field interaction,” *Sci. Rep.*, vol. 4, p. 6346, 2014.
- [163] K. Wang, J. Wang, J. Fan, M. Lotya, A. O. Neill, D. Fox, Y. Feng, X. Zhang, B. Jiang, Q. Zhao, H. Zhang, J. N. Coleman, L. Zhang, and W. J. Blau, “Ultrafast Saturable Absorption of Two-Dimensional MoS₂ Nanosheets,” *ACS Nano*, vol. 7, pp. 9260–9267, 2013.
- [164] G. Zhao, J. Hou, Y. Wu, J. He, and X. Hao, “Preparation of 2D MoS₂/Graphene Heterostructure through a Monolayer Intercalation Method and its Application as an Optical Modulator in Pulsed Laser Generation,” *Adv. Opt. Mater.*, vol. 3, no. 7, pp. 937–942, 2015.
- [165] C. Qin, Y. Gao, Z. Qiao, L. Xiao, and S. Jia, “Atomic-Layered MoS₂ as a Tunable Optical Platform,” *Adv. Funct. Mater.*, vol. 4, no. 10, pp. 1429–1456, 2016.
- [166] R. I. Woodward, R. C. T. Howe, G. Hu, F. Torrisi, M. Zhang, T. Hasan, and E. J. R. Kelleher, “Few-layer MoS₂ saturable absorbers for short-pulse laser

- technology : current status and future perspectives [Invited],” *Photon. Res.*, vol. 3, no. 2, pp. A30–A42, 2015.
- [167] H. S. S. Ramakrishna Matte, A. Gomathi, A. K. Manna, D. J. Late, R. Datta, S. K. Patti, and C. N. R. Rao, “MoS₂ and WS₂ analogues of graphene,” *Angew. Chemie Int. Ed.*, vol. 49, no. 24, pp. 4059–4062, 2010.
 - [168] S. Wang, H. Yu, H. Zhang, A. Wang, M. Zhao, Y. Chen, L. Mei, and J. Wang, “Broadband Few-Layer MoS₂ Saturable Absorbers,” *Adv. mater.*, vol. 26, pp. 3538–3544, 2014.
 - [169] H. Luo, X. Tian, Y. Gao, R. Wei, J. Li, J. Qiu, and Y. Liu, “Antimonene: a long-term stable two-dimensional saturable absorption material under ambient conditions for the mid-infrared spectral region,” *Photon. Res.*, vol. 6, no. 9, pp. 900–907, 2018.
 - [170] J. Gusakova, X. Wang, L. L. Shiau, A. Krivosheeva, V. Shaposhnikov, V. Borisenko, V. Gusakov, and B. K. Tay, “Electronic Properties of Bulk and Monolayer TMDs: Theoretical Study Within DFT Framework (GVJ-2e Method),” *Phys. Stat. Soli.*, vol. 214, no. 12, p. 1700218, 2017.
 - [171] K. Dolui and S. Sanvito, “Dimensionality-driven phonon softening and incipient charge density wave instability in TiS₂,” *Europhys. Lett.*, vol. 115, no. 4, p. 47001, 2016.
 - [172] Y. Wang, L. Li, W. Yao, S. Song, J. T. Sun, J. Pan, X. Ren, C. Li, E. Okunishi, Y. Wang, E. Wang, Y. Shao, Y. Y. Zhang, H. Yang, and E. F. Schwier, “Monolayer PtSe₂, a New Semiconducting Transition-Metal-Dichalcogenide, Epitaxially Grown by Direct Selenization of Pt,” *Nano Lett.*, vol. 15, no. 6, pp. 4013–4018, 2015.
 - [173] B. Huang, L. Du, Q. Yi, L. Yang, J. Li, L. Miao, C. Zhao, and S. Wen, “Bulk-structured PtSe₂ for femtosecond fiber laser mode-locking,” *Opt. Express*, vol. 27, no. 3, pp. 2604–2611, 2019.
 - [174] X. Yu, P. Yu, D. Wu, B. Singh, Q. Zeng, H. Lin, W. Zhou, J. Lin, K. Suenaga, Z. Liu, and Q. J. Wang, “Atomically thin noble metal dichalcogenide: a broadband mid-infrared semiconductor,” *Nat. Commun.*, vol. 9, no. 1, p. 1545, 2018.
 - [175] Z. Huang, W. Zhang, and W. Zhang, “Computational Search for Two-Dimensional MX₂ Semiconductors with Possible High Electron Mobility at Room Temperature,” *Materials (Basel)*, vol. 9, no. 9, p. 716, 2016.
 - [176] S. Tongay, H. Sahin, C. Ko, A. Luce, W. Fan, K. Liu, J. Zhou, Y. Huang, C. Ho, J. Yan, D. F. Ogletree, S. Aloni, J. Ji, S. Li, J. Li, F. M. Peeters, and J. Wu, “Monolayer behaviour in bulk ReS₂ due to electronic and vibrational decoupling,” *Nat. Commun.*, vol. 5, p. 3252, 2014.
 - [177] E. Liu, Y. Fu, Y. Wang, Y. Feng, H. Liu, X. Wan, W. Zhou, B. Wang, L. Shao, C. Ho, Y. Huang, Z. Cao, L. Wang, A. Li, J. Zeng, F. Song, X. Wang, Y. Shi, H. Yuan, H. Y. Hwang, Y. Cui, F. Miao, and D. Xing, “Integrated digital inverters based on two-dimensional anisotropic ReS₂ field-effect transistors,”

Nat. Commun., vol. 6, p. 6991, 2015.

- [178] X. Meng, Y. Zhou, K. Chen, R. H. Roberts, W. Wu, J. Lin, R. T. Chen, X. Xu, and Y. Wang, “Anisotropic Saturable and Excited-State Absorption in Bulk ReS_2 ,” *Adv. Opt. Mater.*, vol. 1800137, pp. 1–8, 2018.
- [179] P. Xu, T. Fu, J. Xin, Y. Liu, P. Ying, X. Zhao, H. Pan, and T. Zhu, “Anisotropic thermoelectric properties of layered compound SnSe_2 ,” *Sci. Bull.*, vol. 62, no. 24, pp. 1663–1668, 2017.
- [180] Y. I. Jhon, J. Lee, M. Seo, J. H. Lee, and Y. M. Jhon, “Van der Waals Layered Tin Selenide as Highly Nonlinear Ultrafast Saturable Absorber,” *Adv. Opt. Mater.*, vol. 1801745, pp. 1–9, 2019.
- [181] Y. Wang, Y. Li, and Z. Chen, “Not your familiar two dimensional transition metal disulfide : structural and electronic properties of,” *J. Mater. Chem. C*, vol. 3, pp. 9603–9608, 2015.
- [182] M. Ghorbani-asl, A. Kuc, P. Miró, and T. Heine, “A Single-Material Logical Junction Based on 2D Crystal PdS_2 ,” *Adv. Mater.*, vol. 28, pp. 853–856, 2016.
- [183] G. Wang, G. Chen, W. Li, W. Zhang, C. Zeng, and W. Zhao, “Indium selenide as a saturable absorber for a wavelength-switchable vector-soliton fiber laser,” *Opt. Mater. Express*, vol. 9, no. 2, pp. 449–456, 2019.
- [184] B. Ghosh, A. Gupta, and B. Bishnoi, “Effects of defects on the electronic properties of WTe_2 armchair nanoribbons,” *J. Semicond.*, vol. 35, no. 11, p. 113002, 2014.
- [185] W. Du, H. Li, C. Lan, C. Li, J. Li, Z. Wang, and Y. Liu, “Graphene/ WS_2 heterostructure saturable absorbers for ultrashort pulse generation in L-band passively mode-locked fiber lasers,” *Opt. Express*, vol. 28, no. 8, pp. 11514–11523, 2020.
- [186] X. Hong, J. Kim, S. Shi, Y. Zhang, C. Jin, Y. Sun, S. Tongay, J. Wu, Y. Zhang, and F. Wang, “Ultrafast charge transfer in atomically thin MoS_2/WS_2 heterostructures,” *Nat. Nanotechnol.*, vol. 9, no. 9, pp. 682–686, 2014.
- [187] P. Cheng, Y. Du, M. Han, and X. Shu, “Mode-locked and Q-switched mode-locked fiber laser based on a ferroferric-oxide nanoparticles saturable absorber,” *Opt. Express*, vol. 28, no. 9, pp. 13177–13186, 2020.
- [188] H. Jiang, H. Shi, X. Sun, and B. Gao, “Optical Anisotropy of Few-Layer Black Phosphorus Visualized by Scanning Polarization Modulation Microscopy Optical Anisotropy of Few-Layer Black Phosphorus Visualized by Scanning Polarization Modulation Microscopy,” *ACS Photon.*, vol. 5, no. 6, pp. 2509–2515, 2018.
- [189] D. Li, H. Jussila, L. Karvonen, G. Ye, H. Lipsanen, X. Chen, and Z. Sun, “Polarization and Thickness Dependent Absorption Properties of Black Phosphorus: New Saturable Absorber for Ultrafast Pulse Generation,” *Sci. Rep.*, vol. 5, p. 15899, 2015.
- [190] H. O. H. Churchill and P. Jarillo-herrero, “Two-Dimensional crystals:

- Phosphorus joins the family,” *Nat. Nanotechnol.*, vol. 9, no. 5, pp. 330–331, 2014.
- [191] S. B. Lu, L. L. Miao, Z. N. Guo, X. Qi, C. J. Zhao, H. Zhang, S. C. Wen, and D. Y. Fan, “Broadband nonlinear optical response in multi-layer black phosphorus: an emerging infrared and mid-infrared optical material,” *Opt. Express*, vol. 23, no. 9, pp. 3370–3377, 2015.
 - [192] K. Wang, B. M. Szyd, G. Wang, X. Zhang, J. J. Wang, J. J. Magan, L. Zhang, J. N. Coleman, J. Wang, and W. J. Blau, “Ultrafast Nonlinear Excitation Dynamics of Black Phosphorus Nanosheets from Visible to Mid-Infrared,” *ACS Nano*, vol. 10, no. 7, pp. 6923–6932, 2016.
 - [193] A. Castellanos-gomez, L. Vicarelli, and E. Prada, “Isolation and characterization of few-layer black phosphorus,” *2D Mater.*, vol. 1, p. 025001, 2014.
 - [194] J. Zhang, X. Yu, W. Han, B. Lv, X. Li, S. Xiao, Y. Gao, and J. He, “Broadband spatial self-phase modulation of black phosphorous,” *Opt. Lett.*, vol. 41, no. 8, pp. 1704–1707, 2016.
 - [195] L. Li, Y. Yu, G. J. Ye, Q. Ge, X. Ou, H. Wu, D. Feng, X. H. Chen, and Y. Zhang, “Black phosphorus field-effect transistors,” *Nat. Nanotechnol.*, vol. 9, pp. 372–377, 2014.
 - [196] J. O. Island, G. A. Steele, H. S. J. Van Der Zant, and A. Castellanos-gomez, “Environmental instability of few-layer black phosphorus,” *2D Mater.*, vol. 2, p. 011002, 2015.
 - [197] M. T. Edmonds, A. Tadich, A. Carvalho, A. Ziletti, S. P. Koenig, D. F. Coker, A. H. C. Neto, and M. S. Fuhrer, “Creating a Stable Oxide at the Surface of Black Phosphorus,” *ACS Appl. Mater. Interfaces*, vol. 7, no. 27, pp. 14557–14562, 2015.
 - [198] H. Mu, S. Lin, Z. Wang, S. Xiao, P. Li, and Y. Chen, “Black Phosphorus – Polymer Composites for Pulsed Lasers,” *Adv. Opt. Mater.*, vol. 3, pp. 1447–1453, 2015.
 - [199] R. Gui, H. Jin, Z. Wang, and J. Li, “Black phosphorus quantum dots: synthesis, properties, functionalized modification and applications,” *Chem. Soc. Rev.*, vol. 47, pp. 6795–6823, 2018.
 - [200] K. A. Ritter and J. W. Lyding, “The influence of edge structure on the electronic properties of graphene quantum dots and nanoribbons,” *Nat. Mater.*, vol. 8, pp. 235–242, 2009.
 - [201] Z. Sun, H. Xie, S. Tang, X. Yu, Z. Guo, J. Shao, H. Zhang, H. Huang, H. Wang, and P. K. Chu, “Ultrasmall Black Phosphorus Quantum Dots: Synthesis and Use as Photothermal Agents,” *Angew. Chemie Int. Ed.*, vol. 54, no. 39, pp. 11526–11530, 2015.
 - [202] S. K. Gupta, Y. Sonvane, G. Wang, and R. Pandey, “Size and edge roughness effects on thermal conductivity of pristine antimonene allotropes,” *Chem. Phys.*

- Lett.*, vol. 641, pp. 169–172, 2015.
- [203] S. Zhang, Z. Yan, Y. Li, Z. Chen, and H. Zeng, “Atomically Thin Arsenene and Antimonene: Semimetal-Semiconductor and Indirect-Direct Band-Gap Transitions,” *Angew. Chemie*, vol. 127, pp. 1–5, 2015.
 - [204] S. Zhang, M. Xie, F. Li, Z. Yan, Y. Li, E. Kan, W. Liu, Z. Chen, and H. Zeng, “Semiconducting Group 15 Monolayers: A Broad Range of Band Gaps and High Carrier Mobilities,” *Angew. Chemie Int. Ed.*, vol. 55, no. 5, pp. 1666–1669, 2016.
 - [205] L. Cheng, H. Liu, X. Tan, J. Zhang, J. Wei, H. Lv, J. Shi, and X. Tang, “Thermoelectric Properties of a Monolayer Bismuth,” *J. Phys. Chem. C*, vol. 118, no. 2, pp. 904–910, 2014.
 - [206] Q. Wang, M. Safdar, K. Xu, M. Mirza, Z. Wang, J. He, and W. E. T. Al, “Van der Waals Epitaxy and Photoresponse of Hexagonal Tellurium Nanoplates on Flexible Mica Sheets,” *ACS Nano*, vol. 8, no. 7, pp. 7497–7505, 2014.
 - [207] Z. Zhu, X. Cai, S. Yi, J. Chen, Y. Dai, C. Niu, and Z. Guo, “Multivalency-Driven Formation of Te-Based Monolayer Materials: A Combined First-Principles and Experimental study,” *Phys. Rev. Lett.*, vol. 119, p. 106101, 2017.
 - [208] X. Huang, J. Guan, Z. Lin, B. Liu, S. Xing, W. Wang, and J. Guo, “Epitaxial Growth and Band Structure of Te Film on Graphene Epitaxial Growth and Band Structure of Te Film on Graphene,” *Nano Lett.*, vol. 17, no. 8, pp. 4619–4623, 2017.
 - [209] N. Ming, S. Tao, W. Yang, Q. Chen, R. Sun, C. Wang, S. Wang, B. Man, and H. Zhang, “Mode-locked Er-doped fiber laser based on PbS/CdS core/shell quantum dots as saturable absorber,” *Opt. Express*, vol. 26, no. 7, pp. 9017–9026, 2018.
 - [210] I. Moreels, K. Lambert, D. Smeets, D. De Muynck, T. Nollet, C. Martins, F. Vanhaecke, C. Delerue, G. Allan, and Z. Hens, “Size-Dependent Optical Properties of Colloidal PbS Quantum Dots,” *ACS Nano*, vol. 3, no. 10, pp. 3023–3030, 2009.
 - [211] L. Cademartiri, E. Montanari, G. Calestani, A. Migliori, A. Guagliardi, and G. A. Ozin, “Size-Dependent Extinction Coefficients of PbS Quantum Dots,” *J. Am. Chem. Soc.*, vol. 128, pp. 10337–10346, 2006.
 - [212] L. Du, S. Lu, L. Du, Z. Kang, J. Li, B. Huang, G. Jiang, L. Miao, G. Qin, and C. Zhao, “Stable Dissipative Soliton Generation From Yb-Doped Fiber Laser Modulated via Evanescent Field Interaction With Gold Stable Dissipative Soliton Generation From Yb-Doped Fiber Laser Modulated via Evanescent Field Interaction With,” *IEEE Photonics J.*, vol. 10, p. 6101008, 2018.
 - [213] Z. Kang, M. Liu, C. Tang, X. Xu, Z. Jia, G. Qin, and W. Qin, “Microfiber coated with gold nanorods as saturable absorbers for 2 μm femtosecond fiber lasers,” *Opt. Mater. Express*, vol. 8, no. 12, pp. 3841–3850, 2018.
 - [214] Z. Kang, X. Gao, L. Zhang, Y. Feng, G. Qin, and W. Qin, “Passively mode-

- locked fiber lasers at 1039 and 1560 nm based on a common gold nanorod saturable absorber,” *Opt. Mater. Express*, vol. 5, no. 4, pp. 794–801, 2015.
- [215] X. Wang, A. Luo, H. Liu, N. Zhao, M. Liu, Y. Zhu, J. Xue, Z. Luo, and W. Xu, “Nanocomposites with gold nanorod/silica core-shell structure as saturable absorber for femtosecond pulse generation in a fiber laser,” *Opt. Express*, vol. 23, no. 17, pp. 22602–22610, 2015.
 - [216] Z. Kang, Q. Li, X. J. Gao, L. Zhang, Z. X. Jia, G. S. Qin, and W. P. Qin, “Gold nanorod saturable absorber for passive mode-locking at 1 μ m wavelength,” *Laser Phys. Lett.*, vol. 11, p. 035102, 2014.
 - [217] Z. Kang, Y. Xu, L. Zhang, Z. Jia, L. Liu, D. Zhao, Y. Feng, G. Qin, and W. Qin, “Passively mode-locking induced by gold nanorods in erbium-doped fiber lasers,” *Appl. Phys. Lett.*, vol. 103, p. 041105, 2013.
 - [218] Y. Horiguchi, K. Honda, Y. Kato, N. Nakashima, and Y. Niidome, “Photothermal Reshaping of Gold Nanorods Depends on the Passivating Layers of the Nanorod Surfaces,” *Langmuir*, vol. 24, no. 20, pp. 12026–12031, 2008.
 - [219] X. Wang, Z. Luo, H. Liu, M. Liu, A. Luo, and W. Xu, “Microfiber-based gold nanorods as saturable absorber for femtosecond pulse generation in a fiber laser,” *Appl. Phys. Lett.*, vol. 105, p. 161107, 2014.
 - [220] C. Cheng, Y. Lin, T. Chen, H. Chen, Y. Chi, C. Lee, C. Wu, and G. Lin, “Can silicon carbide serve as a saturable absorber for passive mode-locked fiber lasers?,” *Sci. Rep.*, vol. 5, p. 16463, 2015.
 - [221] G. L. Desautels, C. Brewer, M. Walker, S. Juhl, M. Finet, S. Ristich, M. Whitaker, and P. Powers, “Femtosecond laser damage threshold and nonlinear characterization in bulk transparent SiC materials,” *J. Opt. Soc. Am. B*, vol. 25, no. 1, pp. 60–66, 2010.
 - [222] A. Nel, T. Xia, L. Madler, and N. Li, “Toxic Potential of Materials at the Nanolevel,” *Science (80-.)*, vol. 311, pp. 622–627, 2006.
 - [223] R. Khazaeinezhad, S. H. Kassani, and B. Paulson, “Ultrafast nonlinear optical properties of thin-solid DNA film and their application as a saturable absorber in femtosecond mode- locked fiber laser,” *Sci. Rep.*, vol. 7, p. 41480, 2017.
 - [224] H. Lee, W. S. Kwon, J. H. Kim, D. Kang, and S. Kim, “Polarization insensitive graphene saturable absorbers using etched fiber for highly stable ultrafast fiber lasers,” *Opt. Express*, vol. 23, no. 17, pp. 22116–22122, 2015.
 - [225] J. Lee, J. Koo, J. Lee, J. Y. Min, and J. H. Lee, “All-fiberized, femtosecond laser at 1912 nm using a bulk-like MoSe₂ saturable absorber,” *Opt. Mater. Express*, vol. 7, no. 8, pp. 2968–2979, 2017.
 - [226] P. Li, Z. Liu, Z. Cong, and X. Chen, “Dual-Wavelength Passively Mode-Locked Yb-Doped Fiber Laser Based on a SnSe₂-PVA Yb-Doped Fiber Laser,” *IEEE Photonics J.*, vol. 11, no. 4, pp. 1–13, 2019.
 - [227] J. D. Zapata, D. Steinberg, L. A. M. Saito, R. E. P. De Oliveira, and A. M.

- Cárdenas, “Efficient graphene saturable absorbers on D-shaped optical fiber for ultrashort pulse generation,” *Sci. Rep.*, vol. 6, p. 20644, 2016.
- [228] S. Ko, J. Lee, S. Member, J. Koo, S. Member, B. S. Joo, M. Gu, and J. H. Lee, “Chemical Wet Etching of an Optical Fiber Using a Hydrogen Fluoride-Free Solution for a Saturable Absorber Based on the Evanescent Field Interaction,” *J. Light. Technol.*, vol. 34, no. 16, pp. 3776–3784, 2016.
- [229] W. S. Kwon, H. Lee, J. H. Kim, J. Choi, K. Kim, and S. Kim, “Ultrashort stretched-pulse L-band laser using carbon-nanotube saturable absorber,” *Opt. Express*, vol. 23, no. 6, pp. 7779–7785, 2015.
- [230] A. G. Rozhin, Y. Sakakibara, and M. Tokumoto, “Near-infrared nonlinear optical properties of single-wall carbon nanotubes embedded in polymer film,” *Thin Solid Films*, vol. 465, pp. 368–372, 2004.
- [231] F. Wang, Y. Jing, Z. Kang, L. Zhou, Z. Li, M. Liu, and T. Wang, “Mesoporous Carbon Nanospheres as Broadband Saturable Absorbers for Pulsed Laser Generation,” *Adv. Opt. Mater.*, vol. 1800606, pp. 1–8, 2018.
- [232] J. Tarka, G. Sobon, J. Boguslawski, J. Sotor, J. Jagiello, M. Aksienionek, L. Lipinska, M. Zdrojek, J. Judek, and K. M. Abramski, “168 fs pulse generation from graphene-chitosan mode-locked fiber laser,” *Opt. Mater. Express*, vol. 4, no. 10, pp. 1981–1986, 2014.
- [233] B. Liu, L. Gao, W. W. Cheng, X. S. Tang, C. Gao, Cao, Y. Long, Y. J. Li, and T. Zhu, “1.6 μm dissipative soliton fiber laser mode-locked by cesium lead halide perovskite quantum dots,” *Opt. Express*, vol. 26, no. 6, pp. 7155–7161, 2018.
- [234] P. C. Debnath, J. Park, A. M. Scott, J. Lee, and J. H. Lee, “In Situ Synthesis of Graphene with Telecommunication Lasers for Nonlinear Optical Devices,” *Adv. Opt. Mater.*, vol. 3, no. 9, pp. 1264–1272, 2015.
- [235] L. Li, Y. Su, Y. Wang, X. Wang, Y. Wang, X. Li, D. Mao, and J. Si, “Femtosecond Passively Er-Doped Mode-Locked Fiber Laser With WS_2 Solution Saturable Absorber,” *IEEE J. Sel. Top. Quantum Electron.*, vol. 23, no. 1, p. 1100306, 2017.
- [236] A. Luo, M. Liu, X. Wang, Q. Ning, W. Xu, and Z. Luo, “Few-layer MoS_2 -deposited microfiber as highly nonlinear photonic device for pulse shaping in a fiber laser [Invited],” *Photon. Res.*, vol. 3, no. 2, pp. A69–A78, 2015.
- [237] P. Yan, A. Liu, Y. Chen, H. Chen, S. Ruan, S. Chen, I. L. Li, H. Yang, J. Hu, and G. Cao, “Microfiber-based WS_2 -film saturable absorber for ultra-fast photonics,” *Opt. Mater. Express*, vol. 5, no. 3, pp. 479–489, 2015.
- [238] H. Jeong, S. Y. Choi, F. Rotermund, K. Lee, and D. Yeom, “All-Polarization Maintaining Passively Mode-Locked Fiber Laser Using Evanescent Field Interaction With Single-Walled Carbon Nanotube Saturable Absorber,” *J. Light. Technol.*, vol. 34, no. 15, pp. 3510–3514, 2016.
- [239] T. Chen, H. Chen, and D. N. Wang, “Graphene Saturable Absorber Based on

- Slightly Tapered Fiber With Inner Air-Cavity,” *J. Light. Technol.*, vol. 33, no. 11, pp. 2332–2336, 2015.
- [240] Z. Liu, X. He, and D. N. Wang, “Passively mode-locked fiber laser based on a hollow-core photonic crystal fiber filled with few-layered graphene oxide solution,” *Opt. Lett.*, vol. 36, no. 16, pp. 3024–3026, 2011.
 - [241] F. W. Wise, A. Chong, and W. H. Renninger, “High-energy femtosecond fiber lasers based on pulse propagation at normal dispersion,” *Laser Photon. Rev.*, vol. 2, pp. 58–73, 2008.
 - [242] Z. Zhang, L. Wang, and Y. Wang, “Sub-100 fs and Passive Harmonic Mode-Locking of Dispersion-Managed Dissipative Fiber Laser With Carbon Nanotubes,” *J. Light. Technol.*, vol. 31, no. 23, pp. 3719–3725, 2013.
 - [243] Y. Wang, S. Alam, E. D. Obraztsova, A. S. Pozharov, S. Y. Set, and S. Yamashita, “Generation of stretched pulses and dissipative solitons at 2 μm from an all-fiber mode-locked laser using carbon nanotube saturable absorbers,” *Opt. Lett.*, vol. 41, no. 16, pp. 3864–3867, 2016.
 - [244] A. B. Grudinin and S. Gray, “Passive harmonic mode locking in soliton fiber lasers,” *J. Opt. Soc. Am. B*, vol. 14, no. 1, pp. 144–154, 1997.
 - [245] J. Wang, Z. Cai, P. Xu, G. Du, F. Wang, S. Ruan, Z. Sun, and T. Hasan, “Pulse dynamics in carbon nanotube mode-locked fiber lasers near zero cavity dispersion,” *Opt. Express*, vol. 23, no. 8, pp. 19947–19958, 2015.
 - [246] L. Hou, H. Guo, Y. Wang, J. Sun, Q. Lin, Y. Bai, and J. Bai, “Sub-200 femtosecond dispersion-managed soliton ytterbium-doped fiber laser based on carbon nanotubes saturable absorber,” *Opt. Express*, vol. 26, no. 7, pp. 9063–9070, 2018.
 - [247] A. Stark, L. Correia, M. Teichmann, and S. Salewski, “Intracavity absorption spectroscopy with thulium-doped fibre laser,” *Opt. Commun.*, vol. 215, pp. 113–123, 2003.
 - [248] G. Sobon, J. Sotor, I. Pasternak, A. Krajewska, and K. M. Abramski, “260 fs and 1 nJ pulse generation from a compact , mode-locked Tm-doped fiber laser,” *Opt. Express*, vol. 23, no. 24, pp. 31446–31451, 2015.
 - [249] Y. Zhang, J. Wang, X. Guan, B. Xu, H. Xu, and Z. Cai, “MoTe₂-Based Broadband Wavelength Tunable Eye-Safe Pulsed Laser Source at 1.9 μm ,” *IEEE Photonics Technol. Lett.*, vol. 30, no. 21, pp. 1890–1893, 2018.
 - [250] J. Wang, X. Zhu, Y. Ma, Y. Wang, M. Tong, S. Fu, J. Zong, K. Wiersma, A. Chavez-pirson, R. A. Norwood, W. Shi, and N. Peyghambarian, “Compact CNT Mode-Locked Ho³⁺-Doped Fluoride Fiber Laser at 1.2 μm ,” *IEEE J. Sel. Top. Quantum Electron.*, vol. 24, no. 3, p. 1101205, 2018.
 - [251] J. Sotor, J. Boguslawski, T. Martynkien, P. Mergo, A. Krajewska, A. Przewolka, W. Strupinski, and G. Sobon, “Tm-doped fiber laser, mode-locked by a graphene saturable absorber,” *Opt. Lett.*, vol. 42, no. 8, pp. 1592–1595, 2017.

- [252] J. Tarka, J. Boguslawski, G. Sobon, I. Pasternak, A. Przewłoka, and W. Strupinski, "Power Scaling of an All-PM Fiber Er-Doped Mode-Locked Laser Based on Graphene Saturable Absorber," *IEEE J. Sel. Top. Quantum Electron.*, vol. 23, no. 1, p. 1100506, 2017.
- [253] R. Lindberg, J. Bogusławski, I. Pasternak, A. Przewłoka, and F. Laurell, "Mapping Mode-Locking Regimes in a Polarization-Maintaining Er-Doped Fiber Laser," *IEEE J. Sel. Top. Quantum Electron.*, vol. 24, no. 3, p. 1101709, 2018.
- [254] X. Li, Y. Wang, Y. Wang, and X. Hu, "Mode-Locked Yb-Doped Fiber Laser Based on Single-Walled Carbon Nanotube Wall Paper Absorber," *IEEE Photonics J.*, vol. 4, no. 1, pp. 234–241, 2012.
- [255] Z. Zhang, Y. Cai, J. Wang, H. Wan, and L. Zhang, "Switchable Dual-Wavelength Cylindrical Vector Beam Generation From a Passively Mode-Locked Fiber Laser Based on Carbon Nanotubes," *IEEE J. Sel. Top. Quantum Electron.*, vol. 24, no. 3, p. 1100906, 2018.
- [256] Y. Wang, J. Li, B. Zhai, Y. Hu, K. Mo, R. Lu, and Y. Liu, "Tunable and switchable dual-wavelength mode-locked Tm 3+-doped fiber laser based on a fiber taper," *Opt. Express*, vol. 24, no. 14, pp. 15299–15306, 2016.
- [257] X. Han, "Nanotube-Mode-Locked Fiber Laser Delivering Dispersion-Managed or Dissipative Solitons," *J. Light. Technol.*, vol. 32, no. 8, pp. 1472–1476, 2014.
- [258] Y. Li, K. Yin, X. Zhang, and X. Zheng, "All-Fiber Bidirectional Mode-Locked Ultrafast Fiber Laser at 2 μm ," *IEEE Photonics J.*, vol. 11, no. 6, pp. 1–9, 2019.
- [259] G. Hu, Y. Pan, X. Zhao, S. Yin, M. Zhang, and Z. Zheng, "Asynchronous and synchronous dual-wavelength pulse generation in a passively mode-locked fiber laser with a mode-locker," *Opt. Lett.*, vol. 42, no. 23, pp. 4942–4945, 2017.
- [260] Y. Wang, J. Li, L. Hong, G. Li, F. Liu, X. Zhou, and Y. Liu, "Coexistence of dissipative soliton and stretched pulse in dual-wavelength mode-locked Tm-doped fiber laser with strong third-order dispersion," *Opt. Express*, vol. 26, no. 14, pp. 4206–4216, 2018.
- [261] C. Wei, Y. Lyu, Q. Li, Z. Kang, H. Zhang, and G. Qin, "Wideband Tunable, Carbon Nanotube Mode-Locked Fiber Laser Emitting at Wavelengths Around 3 μm ," *IEEE Photonics Technol. Lett.*, vol. 31, no. 11, pp. 869–872, 2019.
- [262] Y. Wang, J. Li, E. Zhang, K. Mo, Y. Wang, X. Zhou, and Y. Liu, "Coexistence of noise-like pulse and high repetition rate harmonic mode-locking in a laser," *Opt. Express*, vol. 25, no. 15, pp. 17192–17200, 2017.
- [263] Q. Huang, Z. Huang, M. Al Araithi, A. Rozhin, and C. Mou, "2.4 GHz L-Band Passively Harmonic Mode Locked Er-Doped Fiber Laser Based on Carbon Nanotubes Film," *IEEE Photonics Technol. Lett.*, vol. 32, no. 2, pp. 121–124, 2020.
- [264] X. Liu and M. Pang, "Revealing the Buildup Dynamics of Harmonic Mode-

- Locking States in Ultrafast Lasers,” *Laser Photonics Rev.*, vol. 13, no. 9, pp. 1–9, 2019.
- [265] Y. Wang, D. Mao, X. Gan, L. Han, C. Ma, T. Xi, Y. Zhang, W. Shang, S. Hua, and J. Zhao, “Harmonic mode locking of bound-state solitons fiber laser based on MoS₂ saturable absorber,” *Opt. Express*, vol. 23, no. 1, pp. 205–210, 2015.
 - [266] X. Xu, S. Ruan, J. Zhai, L. Li, J. Pei, and Z. Tang, “Facile active control of a pulsed erbium-doped fiber laser using modulation depth tunable carbon nanotubes,” *Photon. Res.*, vol. 6, no. 11, pp. 996–1002, 2018.
 - [267] K. Y. Lau, M. H. Abu Bakar, F. D. Muhammad, A. A. Latif, M. F. Omar, Z. Yusoff, and M. A. Mahdi, “Dual-wavelength, mode-locked erbium-doped fiber laser employing a graphene/polymethyl-methacrylate saturable absorber,” *Opt. Express*, vol. 26, no. 10, pp. 12790–12800, 2018.
 - [268] M. Pawliszewska, A. Duzynska, M. Zdrojek, and J. Sotor, “Metallic carbon nanotube-based saturable absorbers for holmium-doped fiber lasers,” *Opt. Express*, vol. 27, no. 8, pp. 11361–11369, 2019.
 - [269] J. Guo, R. Shi, R. Wang, Y. Wang, F. Zhang, C. Wang, H. Chen, C. Ma, Z. Wang, Y. Ge, Y. Song, and Z. Luo, “Graphdiyne-Polymer Nanocomposite as a Broadband and Robust Saturable Absorber for Ultrafast Photonics,” *Laser Photon. Rev.*, vol. 1900367, pp. 1–10, 2020.
 - [270] P. Ma, W. Lin, H. Zhang, S. Xu, and Z. Yang, “High-Power Large-Energy Rectangular Mode-Locked Er-Doped Fiber Laser Based on High-Damage-Threshold MoS₂ Saturable Absorber,” *IEEE Photonics J.*, vol. 11, no. 5, pp. 1–12, 2019.
 - [271] R. Lv, Z. Chen, S. Liu, J. Wang, Y. Li, Y. Wang, and Y. Wang, “Optical properties and applications of molybdenum disulfide/SiO₂ saturable absorber fabricated by sol-gel technique,” *Opt. Express*, vol. 27, no. 5, pp. 6348–6356, 2019.
 - [272] J. Lee, K. Lee, S. Kwon, B. Shin, and J. H. Lee, “Investigation of nonlinear optical properties of rhenium diselenide and its application as a femtosecond mode-locker,” *Photon. Res.*, vol. 7, no. 9, pp. 984–993, 2019.
 - [273] J. Li, C. Zhu, F. Li, Jianfeng Yan, X. Li, A. Qyyum, Z. Hu, C. Zhu, and Y. Liu, “Lead Sulfide Saturable Absorber Based Passively Mode-Locked Tm-Doped Fiber Laser,” *IEEE Photonics J.*, vol. 12, no. 2, pp. 1–10, 2020.
 - [274] K. Wang, X. Zhang, I. M. Kislyakov, N. Dong, S. Zhang, G. Wang, J. Fan, X. Zou, J. Du, Y. Leng, Q. Zhao, K. Wu, J. Chen, S. M. Baesman, K. Liao, S. Maharjan, H. Zhang, L. Zhang, S. A. Curran, R. S. Oremland, W. J. Blau, and J. Wang, “Bacterially synthesized tellurium nanostructures for broadband ultrafast nonlinear optical applications,” *Nat. Commun.*, vol. 10, no. 1, pp. 1–10, 2019.
 - [275] S. Liu, R. Lv, Y. Wang, J. Wang, Y. Wang, and H. Wang, “Passively Mode-Locked Fiber Laser with WS₂/SiO₂ Saturable Absorber Fabricated by Sol-Gel Technique,” *ACS Appl. Mater. Interfaces*, vol. 12, no. 26, pp. 29625–29630,

2020.

- [276] P. Guo, X. Li, T. Feng, Y. Zhang, W. Xu, and J. Accepted, “Few-layer bismuthene for coexistence of harmonic and dual-wavelength in a mode-locked fiber laser,” *ACS Appl. Mater. Interfaces*, vol. 12, no. 28, pp. 31757–31763, 2020.
- [277] I. Kubat, C. R. Petersen, U. V. Møller, A. Seddon, T. Benson, L. Brilland, D. Mechin, P. M. Moselund, and O. Bang, “Thulium pumped mid-infrared 0.9–9 μm supercontinuum generation in concatenated fluoride and chalcogenide glass fibers,” *Opt. Express*, vol. 22, no. 4, pp. 3959–3967, 2014.
- [278] A. Khodabakhsh, V. Ramaiah-Badarla, L. Rutkowski, A. C. Johansson, K. F. Lee, J. Jiang, C. Mohr, M. E. Fermann, and A. Foltynowicz, “Fourier transform and Vernier spectroscopy using an optical frequency comb at 3–5.4 μm ,” *Opt. Lett.*, vol. 41, no. 11, pp. 2541–2544, 2016.
- [279] H. Waechter, D. Munzke, A. Jang, and H. Loock, “Simultaneous and Continuous Multiple Wavelength Absorption Multiplexing Fiber-Loop Cavity Ring-Down Spectroscopy,” *Anal. Chem.*, vol. 83, pp. 2719–2725, 2011.